

Yale University

EliScholar – A Digital Platform for Scholarly Publishing at Yale

Yale Graduate School of Arts and Sciences Dissertations

Spring 2021

Intuitive and Accurate Material Appearance Design and Editing

Weiqi Shi

Yale University Graduate School of Arts and Sciences, weiqi.shi@yale.edu

Follow this and additional works at: https://elischolar.library.yale.edu/gsas_dissertations

Recommended Citation

Shi, Weiqi, "Intuitive and Accurate Material Appearance Design and Editing" (2021). *Yale Graduate School of Arts and Sciences Dissertations*. 201.

https://elischolar.library.yale.edu/gsas_dissertations/201

This Dissertation is brought to you for free and open access by EliScholar – A Digital Platform for Scholarly Publishing at Yale. It has been accepted for inclusion in Yale Graduate School of Arts and Sciences Dissertations by an authorized administrator of EliScholar – A Digital Platform for Scholarly Publishing at Yale. For more information, please contact elischolar@yale.edu.

Abstract

Intuitive and Accurate Material Appearance Design and Editing

WeiQi Shi

2021

Creating and editing high-quality materials for photorealistic rendering can be a difficult task due to the diversity and complexity of material appearance. Material design is the process by which artists specify the reflectance properties of a surface, such as its diffuse color and specular roughness [1]. Even with the support of commercial software packages, material design can be a time-consuming trial-and-error task due to the counter-intuitive nature of the complex reflectance models. Moreover, many material design tasks require the physical realization of virtually designed materials as the final step, which makes the process even more challenging due to rendering artifacts and the limitations of fabrication.

In this dissertation, we propose a series of studies and novel techniques to improve the intuitiveness and accuracy of material design and editing. Our goal is to understand how humans visually perceive materials, simplify user interaction in the design process and, and improve the accuracy of the physical fabrication of designs.

Our first work focuses on understanding the perceptual dimensions for measured material data. We build a perceptual space based on a low-dimensional reflectance manifold that is computed from crowd-sourced data using a multi-dimensional scaling model. Our analysis shows the proposed perceptual space is consistent with the physical interpretation of the measured data. We also put forward a new material editing interface that takes advantage of the proposed perceptual space. We visualize each dimension of the manifold to help users understand how it changes the material appearance.

Our second work investigates the relationship between translucency and glossiness in material perception. We conduct two human subject studies to test if subsurface scattering impacts gloss perception and examine how the shape of an object influences this perception. Based on our results, we discuss why it is necessary to include transparent and translucent media for future research in gloss perception and material design.

Our third work addresses user interaction in the material design system. We present a novel Augmented Reality (AR) material design prototype, which allows users to visualize their designs against a real environment and lighting. We believe introducing AR technology can make the design process more intuitive and improve the authenticity of the results for both novice and experienced users. To test this assumption, we conduct a user study to compare our prototype with the traditional material design system with gray-scale background and synthetic lighting. The results demonstrate that with the help of AR techniques, users perform better in terms of objectively measured accuracy and time and they are subjectively more satisfied with their results.

Finally, our last work turns to the challenge presented by the physical realization of designed materials. We propose a learning-based solution to map the virtually designed appearance to a meso-scale geometry that can be easily fabricated. Essentially, this is a fitting problem, but compared with previous solutions, our method can provide the fabrication recipe with higher reconstruction accuracy for a large fitting gamut. We demonstrate the efficacy of our solution by comparing the reconstructions with existing solutions and comparing fabrication results with the original design. We also provide an application of bi-scale material editing using the proposed method.

Intuitive and Accurate Material Appearance Design and Editing

A Dissertation
Presented to the Faculty of the Graduate School
of
Yale University
in Candidacy for the Degree of
Doctor of Philosophy

by
Weiqi Shi

Dissertation Director: Holly Rushmeier

June 2021

© 2021 by Weiqi Shi

All rights reserved.

Contents

Acknowledgements	xi
1 Introduction	1
2 Background	8
2.1 Light Transport	8
2.1.1 Rendering Equation	9
2.1.2 Surface Reflection	10
2.1.3 Subsurface Scattering	11
2.2 BRDF Models and Representations	12
3 A Low-Dimension Perceptual Space for Intuitive Material Appearance Editing	15
3.1 Introduction	15
3.2 Related Works	17
3.2.1 Human Perception to Material Appearance	17
3.2.2 Material Editing	19
3.3 Goal	20
3.4 Crowdsourcing Data Collection	21
3.5 Learning Perceptual Embedding	23
3.5.1 Non-metric Multidimensional Scaling	23
3.5.2 Model Selection	26
3.6 Building A Perceptual Space	27
3.6.1 Perpetual Interpolation Using GPLVM	27

3.6.2	Visualization and Analysis	29
3.7	Perceptual Editing Interface	31
3.7.1	Interface Overview	32
3.8	Discussion and Conclusion	33
4	The Role of Subsurface Scattering in Glossiness Perception	35
4.1	Introduction	35
4.2	Related Work	38
4.2.1	Gloss perception	39
4.2.2	Translucency perception	39
4.2.3	Impact of translucency on gloss	40
4.3	Experiment 1: Pilot Study	41
4.3.1	Methodology	41
4.3.2	Results	46
4.3.3	Discussion	49
4.4	Experiment 2: Impact of Shape	50
4.4.1	Methodology	50
4.4.2	Results	52
4.4.3	Discussion	55
4.5	Discussion	58
4.6	Conclusion	61
5	Material Design in Augmented Reality with In-Situ Visual Feedback	62
5.1	Introduction	62
5.2	Related Work	64
5.2.1	User Study in Appearance Design	64
5.2.2	Material Editing	64
5.2.3	Material Display	65
5.2.4	High Resolution Rendering in Augmented Reality	66
5.2.5	Global Illumination in Mixed Reality	67
5.3	Study Overview	67

5.3.1	Goal	67
5.3.2	Users	68
5.3.3	Task	68
5.3.4	Materials	68
5.3.5	Models and Geometries	69
5.3.6	Interaction	69
5.3.7	Lighting	69
5.3.8	User Interface	70
5.4	Experiment	71
5.4.1	Trials	71
5.4.2	Procedure	72
5.4.3	Questionnaire	72
5.4.4	Rating	72
5.4.5	BRDF Parameters Evaluation	73
5.5	System Implementation	74
5.5.1	System Structure	74
5.5.2	Rendering	75
5.5.3	Light Estimation	76
5.5.4	Tracking	76
5.5.5	Hardware Description	77
5.6	Results	77
5.6.1	Time to Completion	78
5.6.2	Satisfaction for Material Quality	78
5.6.3	Subjective System Ranking and Rating	80
5.6.4	Raters' Evaluation	80
5.6.5	BRDF Parameter Comparison	81
5.7	Workflow Observation	81
5.7.1	Lighting Adjustment	81
5.7.2	Geometry Consistency	82
5.7.3	Object Interaction	82

5.7.4	Real Scenes vs. Synthetic Scenes	83
5.7.5	One-Parameter-at-a-Time	83
5.7.6	Spectrum vs. Sliders	83
5.8	Discussion	84
5.9	Conclusion	85
6	Learning-Based Inverse Bi-Scale Material Fitting from Tabular BRDFs	87
6.1	Introduction	87
6.2	Related Work	90
6.2.1	Bi-Scale Design	91
6.2.2	Microfacet Material Modeling	92
6.2.3	Inverse Rendering and BRDF Fitting	92
6.2.4	Learning Materials in Image Space	93
6.3	Method	93
6.3.1	Simulation	94
6.3.2	Tabular BRDF Representation	96
6.3.3	Network Architecture	99
6.3.4	Color Restoration	100
6.4	Implementation	101
6.5	Results	103
6.5.1	Tabular BRDF Analysis	104
6.5.2	Training results	107
6.5.3	Comparison	107
6.5.4	Validation on measured materials	110
6.6	Applications	112
6.6.1	Bi-scale design	112
6.6.2	Fabrication	113
6.7	Discussion	114
6.8	Conclusion	115
7	Limitations, Future Work, and Conclusion	117

List of Figures

1.1	Material design interface in Blender	2
1.2	Overview of our contributions in this dissertation.	4
2.1	Light reflection on the surface.	9
2.2	Three types of surface reflection.	10
2.3	Example of subsurface scattering	11
3.1	Example of stimuli of our psychophysical experiment.	21
3.2	Training and testing errors (percentage of violation) for different λ in Cross validation.	27
3.3	Visualization of each perceptual dimension that is interpolated using GPLVM.	29
3.4	BRDF-slices of the first 5 principal components of the 39 metal BRDF stimuli and a slice reference.	30
3.5	Comparison between our method and mapping perceptual embedding to the first 5 principle components and then perform reconstruction.	31
3.6	Example of our proposed user interface.	32
4.1	Examples of materials and shapes used in the study of the impact of subsurface scattering on gloss.	36
4.2	Sphere examples with the same surface roughness but different subsurface scattering properties.	42
4.3	Sphere examples with the same subsurface scattering properties but different surface roughness.	42
4.4	Significance tables for each roughness level for Experiment 1.	47

4.5	Z-scores for fixed roughness experiments.	47
4.6	The significance table for all 30 stimuli.	48
4.7	Z-scores for the comparisons of all 30 stimuli.	48
4.8	Five different shapes have been studied throughout the experiment. Left to right: sphere, spiky sphere, Stanford Lucy, low-resolution Lucy and cylinder.	51
4.9	Significance tables for each roughness level of Lucy.	53
4.10	Z-scores results for Lucy. The difference among Z-scores grows with the increase of roughness.	53
4.11	The variance (left) of the mean Z-scores and the number of significantly different pairs (right).	54
4.12	Z-score as a function of the extinction coefficient (top row) and albedo (bottom). Sphere (red circles) and Lucy (blue diamonds).	54
4.13	Z-score results for Sphere. Larger circle diameters represent a higher mean Z-score.	54
4.14	The results for Lucy. High albedo and low extinction coefficient usually yield glossier stimuli.	55
4.15	Comparison between objects with identical shapes and surface roughness but differ- ent albedo of subsurface scattering.	57
4.16	Curvature influences glossiness cues - thus, the perceived relative glossiness of the objects.	58
5.1	Augmented Reality material design user interface and Virtual Synthetic material design user interface.	70
5.2	Reference materials, test objects for AR tracking and time limits for all trials. . . .	71
5.3	Example of designed materials of two subjects using different systems.	74
5.4	Augmented Reality system setup.	75
5.5	Average time to completion for all trials over novice and experienced users (in seconds).	77
5.6	Average material quality rating over novice and experienced users.	78
5.7	Average system rating over novice and experienced users and distribution of prefer- ence rating.	79

5.8	Average number of votes for each system and percentage of selected reasons of votes for AR systems.	79
5.9	Mean square errors between user defined material BRDF parameters and estimated BRDF parameters over two systems.	80
6.1	Bi-scale material fitting framework with given the large-scale appearance, reconstruction, and new designs	88
6.2	Example of bi-scale material in real life.	89
6.3	Comparison of bi-scale simulations.	96
6.4	Examples of different tabular BRDF formats.	98
6.5	The pipeline of our bi-scale learning model and network architecture.	99
6.6	Compared to other color optimization approaches.	102
6.7	Examples of different meso-scale geometry primitives used for simulation.	103
6.8	Comparison of reconstructed anisotropic appearance for different tabular formats with 10 times difference between predictions and the ground truth.	105
6.9	Two example materials and the feature maps of tabular formats from the fifth convolutional layer.	106
6.10	The best (left side) and worst-case (right side) predictions on a set of 200 images. .	108
6.11	Qualitative comparison ($4 \times$ difference) between our method and previous work. .	109
6.12	Qualitative comparison ($4 \times$ difference) between our method and previous work for multi-color materials.	110
6.13	Results of user study using Amazon Mechanical Turk.	111
6.14	Validation on measured materials from RGL material database.	111
6.15	The BRDF slice along the mirror directions and lobe comparison.	112
6.16	Bi-scale design example.	113
6.17	Bi-scale design for multi-color anisotropic materials.	113
6.18	Fabrication example with target appearance modeled as a macro-BRDF for a given sample, the reconstruction using our method and small-scale details, and an image of the real world woven sample.	114
6.19	Failure reconstruction of material example with iridescent effect.	116

List of Tables

4.1	The depth of the objects in X, Y and Z dimensions.	56
4.2	Gaussian curvature (GC) and mean curvature (MC) are found locally for each point of the 3D object.	56
5.1	Estimated BRDF parameter values for all target objects in experiment.	80
6.1	Evaluation of Different Tabular BRDFs (8500 samples)	104
6.2	Ablation Study (8500 samples)	104
6.3	Comparison of 200 randomly sampled materials	108

Acknowledgements

First, I would like to thank my advisor Holly Rushmeier for her patient guidance, insightful advice, and immediate feedback. This dissertation would not have been possible without her encouragement and support. During my PhD years, she has taught me to think like a scientist and do things with a high standard. It has been a great privilege to work with Holly.

I also thank my dissertation committee members: Julie Dorsey, Steven Zucker and Diego Gutierrez. Thank you for all the constructive comments and contribution and all the time spent. I feel extremely fortunate to have the chance to work with such an excellent group of people.

I would like to express my gratitude to all my collaborators: Manfred Lau, Goze Akoglu, Eleni Kotoula, Ying Yang, Metin Sezgin, Davit Gigilashvili, Steven L. Song, and Michael Reed. I feel extremely fortunate to have the chance to work with such an excellent group of people.

I would like to thank my lab mates at Yale Graphics Group: Zeyu Wang, Sherry Qiu, Yiwei Hu, Chengan He and Ezira Davis for the countless conversations and the stimulating environment they created. Special thanks to Zeyu Wang for the contribution to many of my projects and numerous hours we spent discussing exciting ideas.

Finally, I thank my parents Guanqi Shi and Ling Wang for their continuous and unconditional support over all these years. They give me the courage and strength to explore and pursue things I am interested in.

Chapter 1

Introduction

One of the main properties of an object that contributes to its appearance is material. Many designers desire to effortlessly alter object materials. The process to create or edit the appearance of a given object can be referred to as material design. It has been widely used in the industry to create digital content (video games/animated films) or fabricate products with a particular look (clothes, furniture, paint, and so on). To help visualize the design, many digital software packages (Maya [2], blender [3] etc.) provide toolboxes for a designer to achieve their goal on virtual platforms. However, even with the help of software, the material design process is still not intuitive due to complex reflectance properties and the changeable appearance of the real-world materials under different conditions such as lighting, camera view, and the shape of the objects. In general, material design is a time-consuming trial and error task. In this dissertation, we focus on how to intuitively and accurately design and model material appearance using digital software.

To make the material design process more intuitive, two factors need to be considered: material models and user interaction. Material models define the reflectance properties and the look of the material. Users can change the visual appearance by tweaking the parameters of the models. To reproduce the appearance of complex materials, physically-based shading models have been developed and implemented in many design applications. These models can produce physically plausible reflectance behavior and rich appearance details. However, it is challenging to edit those models intuitively because of the large number of parameters involved. Users need to understand the meaning of each parameter and how they influence appearance before they can start a design task. The inconsistency of the implementation of material models between different applications

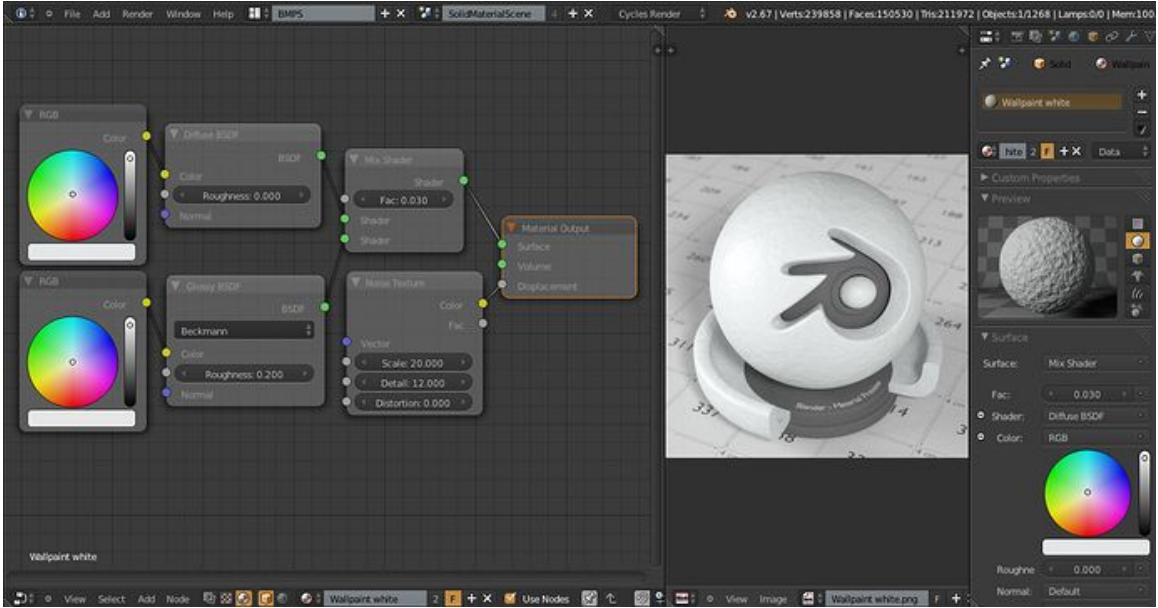


Figure 1.1: Material design interface in Blender

can also cause problems, even if they are using the same group of parameters to define the model. Furthermore, physically plausible shading models are not always consistent with human perception, and changing some parameters may lead to subtle appearance changes that humans cannot perceive.

Another challenge of material appearance design comes from user interaction. Virtual 3D applications are the platform for most of the material design tasks. The results are presented under virtual lighting (normally a single point light), and against a virtual background such as a cube map, gray room, or a checkerboard (Fig. 1.1). These settings may work for digital content creation but are far from ideal for those materials that need to be fabricated and used in the real world. Since material appearance may vary significantly under different lighting conditions, it is worth investigating how the design environment and interaction tools can make a difference on the material design process.

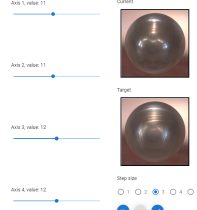
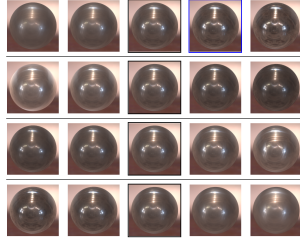
Given the virtually designed material, how to accurately realize its appearance in the real world is also a challenge for the manufacturing industry. To fabricate a material with a certain appearance, the physical parameters that describe the geometric structures at the meso-scopic scale are needed. However, most of the current material design systems are developed to facilitate digital content creation, ignoring the demands and constraints of fabrication and physical realization. The output of those systems are normally the parameters of analytical models that can only be used for rendering. Therefore, finding the methods and materials to fabricate the appearance that accurately matches the

virtual design is still an open question.

In this dissertation, we first focus on studying and analyzing intuitive material models that taken human perception into consideration. The goal is to understand how humans visually perceive materials and build a low-dimensional perceptual space that can explain the real-world materials. There have been some prior attempts to fit material appearance with perceptual dimensions. But most of them only focus on providing explicit and analytic solutions to explain one single visual feature, such as glossiness [4, 5, 6]. We expand from previous work and consider multiple visual features at the same time to build a complete perceptual space. We believe this is the key to create intuitive material models, which can make the design process more straightforward. Due to the diversity of material appearance, we narrow our focus on two types of special materials: metal-like materials with high glossiness and translucent materials. However, the methodologies of the study can be applied to more general material categories. In Chapter 3 we extract the perceptual features of the measured materials from a psychophysical study and use the features to build a perceptual space. In Chapter 4 we study what features influence human perception of translucent materials.

Next, we address the user interaction issue in the design process. Our goal is to present users with a more realistic and immersive environment for material design. We take advantage of the Augmented Reality (AR) techniques and propose an AR material design system, which could allow users to visualize their designs against the real-world environment. The designed materials are lit by natural lighting and projected to physical replicas that can be easily interacted with. In Chapter 5, we present an AR material design prototype and conduct a user study to compare our prototype with a traditional material design system with a synthetic environment. The user study helps us evaluate our system and help us understand how the AR techniques improve the intuitiveness of the design process.

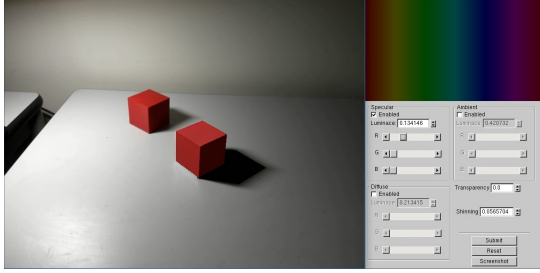
Lastly, we tackle the challenge of physical realization of the designed materials. The idea is to find a bi-scale mapping between the large-scale appearance and meso-scale geometries. The challenges come from both sides of the mapping: how to represent the large-scale materials due to its changeable appearance under different lighting conditions, and how to iterate meso-scale geometries that have diverse patterns and nonlinear representations. It is worth noting that there has been some prior work focusing on similar material fitting problems. However these either use analytical models for fitting, whose results cannot be used for fabrication [7, 8, 9, 10, 11, 12, 13], or use an iterative



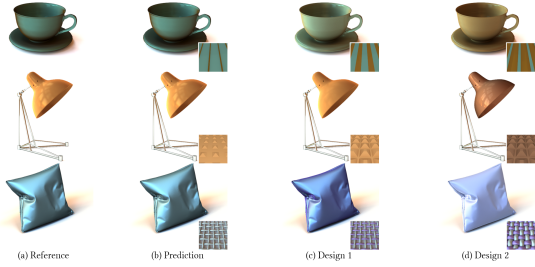
Chapter 3



Chapter 4



Chapter 5



Chapter 6

Figure 1.2: Overview of our contributions in this dissertation.

search-based solution that suffers from low accuracy [14]. In Chapter 6, we propose a solution to solve these problems. To represent the large-scale materials, we use a tabulated structure to represent its reflectance behavior in low dimensions. We analyze the different ways to construct a tabulated structure to take advantage of the spatial features from the reflection. For the meso-scale geometries, we use a learning-based solution to build the nonlinear bi-scale mapping with synthetic training data. Our method takes as input the tabulated structure of large-scale appearance and outputs the physical parameters of the meso-scale geometries and micro-scale reflectance data. To evaluate the proposed method, we compare the reconstruction accuracy with existing solutions and demonstrate the fabrication results. We also provide an application of bi-scale material editing using the proposed method.

To summarize, we conduct user studies and develop a series of novel techniques to improve the intuitiveness and accuracy of material design and related fabrication. These techniques were presented at multiple conferences and journals [15, 16, 17]. The study introduced in Chapter 4 was a collaborative project between the author and Davit Gigilashvili. Our specific contributions include:

Building an intuitive perceptual space based on measured material manifolds. Understand-

ing human visual perception to materials is challenging. Real-world material appearance functions are usually described by non-linear and high-dimensional physical properties, and their connections to human visual system are not always explicitly defined. In this chapter, we present a method to build an intuitive low-dimensional perceptual space for real-world measured material data based on its underlying non-linear reflectance manifold. Unlike many previous works that address individual perceptual attributes (such as gloss), we focus on building a complete perceptual space with multiple attributes and understanding how they influence the material perception. We first use the crowd-sourced data on the perceived similarity of measured materials to build a multi-dimensional scaling model. Then we use the output as a low-dimensional manifold to construct a perceptual space that can be interpolated and extrapolated with Gaussian process latent variable models. Given the perceptual space, we propose a material design interface using the manifold, which allows users to edit appearance using its perceptual dimensions with visual variations.

Evaluating the difference and relationship between glossiness and translucency for material perception. This study investigates the potential impact of subsurface light transport on gloss perception to broaden our understanding of visual appearance in computer graphics applications. Gloss is an important attribute for characterizing material appearance. We hypothesize that subsurface scattering of light impacts the glossiness perception. However, gloss has been traditionally studied as a surface-related quality and the findings in the state-of-the-art are usually based on fully opaque materials, although the visual cues of glossiness can be impacted by light transmission as well. To address this gap and to test our hypothesis, we conducted psychophysical experiments and found that subjects perceive a difference in gloss between stimuli that differ in subsurface light transport but have identical surface qualities and object shape. This gives us a clear indication that subsurface light transport contributes to a glossy appearance. Furthermore, we conducted additional experiments and found that the contribution of subsurface scattering to gloss varies across different shapes and levels of surface roughness. We argue that future research on gloss should include transparent and translucent media and extend the perceptual models currently limited to surface scattering to more general ones inclusive of subsurface light transport.

Developing an AR material design prototype and studying its contributions in terms of user interaction for material design. Material design is the process by which artists or designers set the appearance properties of virtual surface to achieve a desired look. This process is often

conducted in a virtual synthetic environment however, advances in computer vision tracking and interactive rendering now makes it possible to design materials in augmented reality (AR), rather than purely virtual synthetic, environments. However, how designing in an AR environment affects user behavior is unknown. To evaluate how work in a real environment influences the material design process, we propose a novel material design interface that allows designers to interact with a tangible object as they specify appearance properties. The setup allows designers to view the real-time rendering of appearance properties through a virtual reality setup as they manipulate the object. Our setup uses a camera to capture the physical surroundings of the designer to create subtle but realistic reflection effects on the virtual view superimposed on the tangible object. The effects are based on the physical lighting conditions of the actual design space. We describe a user study that compares the efficacy of our method to that of a traditional 3D virtual synthetic material design system. Both subjective feedback and quantitative analysis from our study suggest that the in-situ experience provided by our setup allows the creation of higher quality material properties and supports the sense of interaction and immersion.

Proposing a learning-based solution for bi-scale material fitting and fabrication. Relating small-scale structures to large-scale appearance is a key element in material appearance design. Bi-scale material design requires finding small-scale structures – meso-scale geometry and micro-scale BRDFs – that produce a desired large-scale appearance expressed as a macro-scale BRDF. The adjustment of small-scale geometry and reflectance to achieve a desired appearance can become a tedious trial-and-error process. We present a learning-based solution to fit a target macro-scale BRDF with a combination of a meso-scale geometry and micro-scale BRDF. We confront challenges in representation at both scales. At the large scale we need macro-scale BRDFs that are both compact and expressive. At the small scale we need diverse combinations of geometric patterns and potentially spatially varying micro-BRDFs. For large-scale macro-BRDFs, we propose a novel 2D subset of a tabular BRDF representation that well preserves important appearance features for learning. For small-scale details, we represent geometries and BRDFs in different categories with different physical parameters to define multiple independent continuous search spaces. To build the mapping between large-scale macro-BRDFs and small-scale details, we propose an end-to-end model that takes the subset BRDF as input and performs classification and parameter estimation on small-scale details to find an accurate reconstruction. Compared with other fitting methods, our learning-based solution

provides higher reconstruction accuracy and covers a wider gamut of appearance.

The dissertation is organized as follows. We first introduce the basic background of light transport and material models in Chapter 2. From Chapters 3 to 6, we present technical details and user studies for an intuitive and accurate material design system, including analyzing perceptual space of different materials, building an AR system, and proposing algorithms for fitting bi-scale materials respectively. Finally, we present our conclusion and discuss future research directions in Chapter 7.

Chapter 2

Background

In this chapter, we review the basic concepts used throughout this dissertation. We start with a brief review of physically-based light transport (Section 2.1). Then, we introduce different BRDF models and their representations (Section 2.2).

2.1 Light Transport

The simulation of light transport with physical laws provides accurate and photorealistic results. Two types of optics models explain light transport, modern quantum optics and classical optics. Quantum optics explains the dual wave-particle nature of light and is the most accurate model. Within classical optics are the wave and geometric optics models. Geometric optics addresses objects whose scale is much larger than the wavelength of light so that physical effects such as diffraction and interference modeled by wave optics are negligible. In this dissertation, we focus on problems where the assumptions for geometric optics hold. Geometric optics models assume that light travels instantly through any medium, and it travels in straight lines in a vacuum. With these assumptions, we can model light transport and its interaction with objects easily without considering the wavelength (spectral) and time dimensions.

In the rest of this section, we introduce the rendering equation (Section 2.1.1), surface reflection (Section 2.1.2) and subsurface scattering (Section 2.1.3).

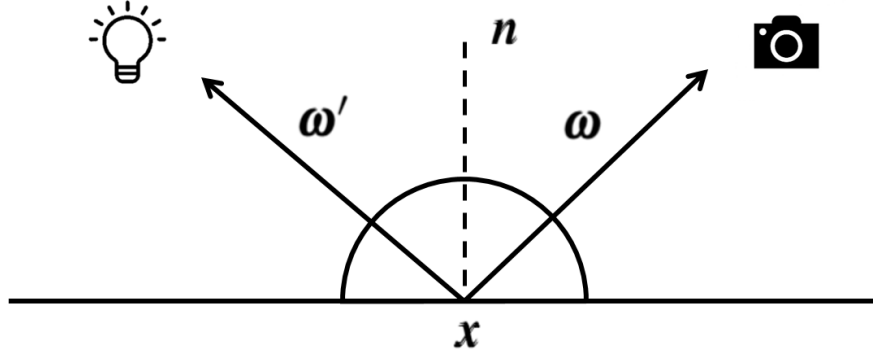


Figure 2.1: Light reflection on the surface.

2.1.1 Rendering Equation

The rendering equation [18] was introduced for computer graphics applications to simulate the process of light transport. This equation mathematically describes the process of light propagation and reflection. It is based on the assumption that the medium the light travels through has a homogeneous refractive index and does not participate in the light scattering.

The rendering equation can be written as:

$$L_o(\mathbf{x}, \boldsymbol{\omega}) = L_e(\mathbf{x}, \boldsymbol{\omega}) + L_r(\mathbf{x}, \boldsymbol{\omega}) \quad (2.1)$$

$$L_o(\mathbf{x}, \boldsymbol{\omega}) = L_e(\mathbf{x}, \boldsymbol{\omega}) + \int_{\Omega} f_r(\mathbf{x}, \boldsymbol{\omega}', \boldsymbol{\omega}) L_i(\mathbf{x}, \boldsymbol{\omega}') |\mathbf{n} \cdot \boldsymbol{\omega}'| d\boldsymbol{\omega}'$$

where L_o is the outgoing radiance from point \mathbf{x} towards direction $\boldsymbol{\omega}$, L_e is the radiance emitted from point \mathbf{x} to direction $\boldsymbol{\omega}$ and L_i is the radiance of incident light incoming from $-\boldsymbol{\omega}'$ direction to point \mathbf{x} . The radiance we mentioned here is the differential radiant power per unit projected area per unit solid angle. It expresses the amount of light that arrives at or leave from the surface point \mathbf{x} in the direction $\boldsymbol{\omega}$. Therefore the integral can also be written as a five-dimensional variable $L_r(\mathbf{x}, \boldsymbol{\omega})$ in the equation. The incoming radiance is integrated on the hemisphere Ω , which is centered at point \mathbf{x} and rotated with respect to the normal \mathbf{n} . f_r represents bidirectional reflectance distribution function (BRDF) of the surface at position \mathbf{x} , with surface normal \mathbf{n} , which will be introduced in the next subsection. The dot product $\mathbf{n} \cdot \boldsymbol{\omega}'$ is the cosine of the angle between vector $\boldsymbol{\omega}'$ and the surface normal. $d\boldsymbol{\omega}'$ is the differential solid angle of incoming light.

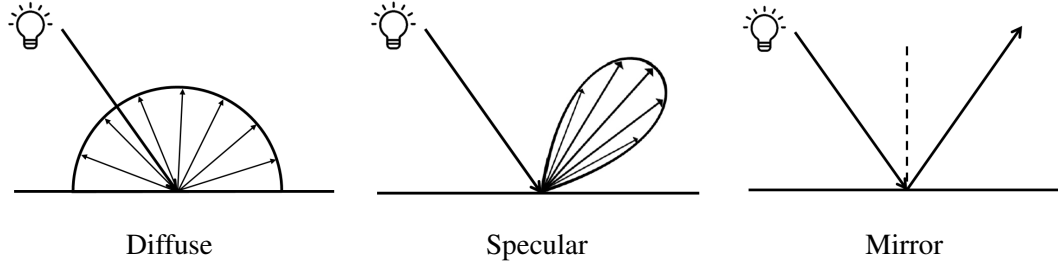


Figure 2.2: Three types of surface reflection.

2.1.2 Surface Reflection

The bidirectional reflectance distribution function (BRDF) describes the light reflected by a particular material. The BRDF represents the ratio between the differential reflected radiance L_r in the outgoing direction ω and the product of the incident radiance L_i of the incoming direction $-\omega'$ and the cosine of the incident angle between \mathbf{n} and ω' . It can be written as:

$$f_r(\mathbf{x}, \omega', \omega) = \frac{dL_r(\mathbf{x}, \omega)}{L_i(\mathbf{x}, \omega') |\mathbf{n} \cdot \omega'| d\omega'} \quad (2.2)$$

BRDFs have these three properties:

- positivity $f_r(\mathbf{x}, \omega', \omega) \geq 0$
- Helmholtz reciprocity: $f_r(\mathbf{x}, \omega', \omega) = f_r(\mathbf{x}, \omega, \omega')$
- Energy conservation $\int_{\Omega} f_r(\mathbf{x}, \omega', \omega) |\mathbf{n} \cdot \omega'| d\omega' \leq 1$

In computer graphics BRDF definitions with these three properties are generally referred to as “physically plausible.”

Generally, there are three types of surface reflections due to the different material properties: diffuse, specular, and mirror reflection. Diffuse reflection spreads the incident energy equally (Lambertian reflection) or near equally into all outgoing directions on the hemisphere. Mirror reflection reflects the light only in the direction of perfect reflection. Specular reflection scatters light into the outgoing directions within a certain range, called the specular lobe, around the mirror direction.

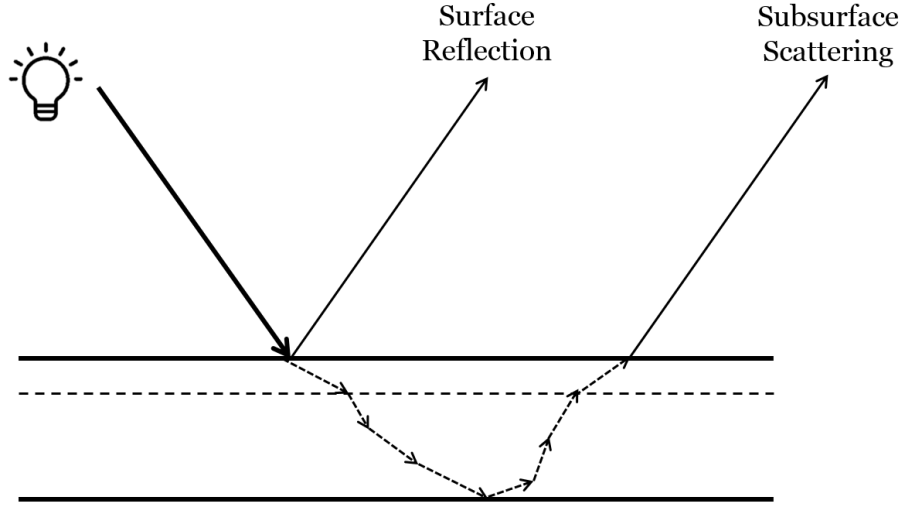


Figure 2.3: Example of subsurface scattering

Instead of being directly reflected at a single point on the material surface, the light may go through the participating medium within an object, scatter, and exit at a different point. This effect is called subsurface scattering or volume scattering. Simulating the process of light propagation and interactions inside the medium can enrich the visual effects that cannot be simply modeled with surface reflection.

When light travels inside a participating medium, it interacts with the material through absorption and scattering. These normally occur due to interactions between photons and the particles randomly distributed in the medium. We define σ_a and σ_s as the absorption and scattering coefficients to represent the probability densities of a photon being absorbed or scattered after traveling a unit distance respectively. Alternatively, we can define the extinction coefficient $\sigma_t = \sigma_a + \sigma_s$ and the single-scattering albedo $\alpha = \sigma_s / \sigma_t$. To explain the distribution of light scattered in a medium, we can use phase function $f_p(\omega', \omega)$ to describe the probability of a photon that travels from the direction ω' and is redirected to the direction ω .

2.1.3 Subsurface Scattering

Given these notations, we can use the radiative transfer equation (RTE) [19]:

$$(\boldsymbol{\omega} \cdot \nabla)L(\mathbf{x}, \boldsymbol{\omega}) = -\sigma_t L(\mathbf{x}, \boldsymbol{\omega}) + \sigma_s L_s(\mathbf{x}, \boldsymbol{\omega}) + Q(\mathbf{x}, \boldsymbol{\omega}) \quad (2.3)$$

$-\sigma_t L(\mathbf{x}, \boldsymbol{\omega})$ represents the radiance loss due to the collision between photons and the particles of the medium, which makes photons no longer contribute to $L(\mathbf{x}, \boldsymbol{\omega})$. The collision includes photons being absorbed or scattered into another direction (out-scattering).

The second term $\sigma_s L_s(\mathbf{x}, \boldsymbol{\omega})$ describes photons that travel from other directions and then are scattered into direction $\boldsymbol{\omega}$ (in-scattering). We can compute this term by scaling the total in-scattering radiance $L_s(\mathbf{x}, \boldsymbol{\omega})$ with σ_s , and the total radiance is the integral of the directional radiance and the phase function over the unit sphere Ω .

$$L_s(\mathbf{x}, \boldsymbol{\omega}) = \int_{\Omega} f_p(\mathbf{x}, \boldsymbol{\omega}', \boldsymbol{\omega}) L(\mathbf{x}, \boldsymbol{\omega}') d\boldsymbol{\omega}' \quad (2.4)$$

The last term $Q(\mathbf{x}, \boldsymbol{\omega})$ specifies the amount of illumination emitted by the medium itself.

We can evaluate $L(\mathbf{x}, \boldsymbol{\omega})$ at a given point \mathbf{x} by integrating the both sides of the equation 2.3.

$$L(\mathbf{x}, \boldsymbol{\omega}) = \int_{\mathbf{y}}^{\mathbf{x}} \tau(\mathbf{x}', \mathbf{x}) (Q(\mathbf{x}', \boldsymbol{\omega}) + \sigma_s(\mathbf{x}') \int_{\Omega} f_p(\mathbf{x}, \boldsymbol{\omega}', \boldsymbol{\omega}) L(\mathbf{x}, \boldsymbol{\omega}') d\boldsymbol{\omega}') d\mathbf{x}' + \tau(\mathbf{y}, \mathbf{x}) L(\mathbf{y}, \boldsymbol{\omega}) \quad (2.5)$$

where \mathbf{y} defines the endpoint of a line segment starting from \mathbf{x} with length s , $\mathbf{y} = \mathbf{x} - s\boldsymbol{\omega}$, and $\tau(\mathbf{y}, \mathbf{x})$ describes the transmittance between the two points.

$$\tau(\mathbf{y}, \mathbf{x}) = \exp\left(-\int_{\mathbf{y}}^{\mathbf{x}} \sigma_t(\mathbf{x}') d\mathbf{x}'\right) \quad (2.6)$$

2.2 BRDF Models and Representations

To achieve photorealism, many BRDF models have been introduced in computer graphics to simulate different kinds of materials and surfaces. There are three types of BRDF models: empirical, physical-based, and measured BRDF models.

Empirical BRDF models are created based on the empirical observation of light reflection on material surfaces. Ward [20] proposed an empirical anisotropic BRDF model that has been widely used due to its capability of modeling various materials and its intuitiveness. To efficiently evaluate the Ward model, Walter [21] propose the derivation of the probability density function for its associated Monte Carlo sampling. The Phong model [22] is another widely used empirical reflection model in real-time graphics applications due to its simplicity and inexpensive evaluation. In Chapter 5, we conduct a material editing user study using the Phong model to compare the AR and traditional material design system. We choose this model because it is intuitive for novice users. The Phong BRDF model can be described as follow:

$$f_r(\mathbf{x}, \boldsymbol{\omega}', \boldsymbol{\omega}) = \frac{k_d}{\pi} + k_s \cos^n \alpha \quad (2.7)$$

k_d and k_s are the diffuse and specular albedo representing the fraction of light with diffuse and specular reflection. n is the specular exponent representing the shininess of the surface. Higher values of n lead to sharper specular reflections and stronger highlights. α is the angle between the mirror reflection of incoming direction $\boldsymbol{\omega}'$ about the normal at point \mathbf{x} and the outgoing direction $\boldsymbol{\omega}$. Note that, the empirical Phong model is based only on observation and is not very accurate and not physically-based, which could produce unrealistic, artificial results.

Physically-based BRDFs are created to simulate the physically correct reflectance behavior and achieve photorealistic rendering. The most relevant models are microfacet models such as the Oren-Nayar [23], Blinn [24]. and Cook-Torrance [25] models. The microfacet BRDF models are based on the assumption that lights interact with tiny microfacets on the surface and the reflection on each facet is either a mirror (Blinn and Cook-Torrance) or Lambertian reflector (Oren-Nayar). The material appearance largely depends on the distribution of the facet normals, which describe the orientation of each facet. If the facet's normals are specular and are concentrated around a certain direction, the overall appearance will be glossy. If their normals spread to every direction, the overall surface looks diffuse. We use the normal distribution function (NDF) to model the distribution of the facet normals. NDF indicates the percentage of microfacets reflecting light from the incident direction $\boldsymbol{\omega}'$ to the outgoing direction $\boldsymbol{\omega}$. It can also be interpreted as the percentage of microfacets whose normals point to the half vector direction $\boldsymbol{\omega}_h$ between the camera and light directions. We can

represent the microfacet BRDF as follows:

$$f_r(\omega', \omega) = \frac{F(\omega, \omega_h)G(\omega, \omega', \omega_h)D(\omega_h)}{4(\mathbf{n} \cdot \omega')(\mathbf{n} \cdot \omega)} \quad (2.8)$$

The D represents the NDF in the equation. The F denotes the Fresnel term that defines how reflections are low when viewed straight on and are increased at glancing angles. G is the shadowing-masking term that takes occluded microfacets into account. Shadowing means a microfacet is not visible from the incident direction and therefore is not illuminated and not contributing to the reflection. Masking means a microfacet is not visible to the outgoing direction and therefore does not contribute to the reflection.

The last category of BRDF models is measured BRDF. Measured BRDFs can accurately capture the material appearance that appears in the real-world but require storing large quantities of data. The number of captured BRDFs is limited because the acquisition techniques and equipment are expensive. Matusik et al. [26] propose a data-driven reflectance model and a data format supporting isotropic measured BRDFs. They also provide a dataset including 100 measured BRDFs (MERL dataset) presented in Rusinkiewicz coordinates [27]. The Rusinkiewicz coordinates take advantage of the properties of half-angle directions, and it allows the sampling density to vary near the specular highlight. In Chapter 6, we use the MERL dataset to generate training data for our learning-based solution. Another measured BRDF model related to our work is the RGL dataset [28]. They propose an adaptive BRDF sampling method to capture the real-world material appearance based on the precomputed NDF. Their dataset covers a large range of appearances and includes anisotropic BRDFs. In Chapter 3, we use both the RGL and the MERL dataset to create stimuli for our psychophysical study.

Chapter 3

A Low-Dimension Perceptual Space for Intuitive Material Appearance Editing

3.1 Introduction

In this chapter we consider problems arising in a common approach for authoring appearance. The appearance of an existing real-world material is captured as a starting point, and then edited to create a new material. Real-world materials display complex and diverse appearances. To capture their rich details for photorealistic rendering, material acquisition techniques have been developed to measure their reflectance. However, the raw measurements are not easily interpreted by a user [29]. The high dimension and non-linearity of the measured reflectance data make it difficult to understand the material recognition process and edit the appearance intuitively. There have been many previous works studying the perceptual dimensions of measured material data. However, they either focus on an individual perceptual attribute such as gloss [4, 5] and translucency [30, 31] or project perceptual dimensions onto a subset of principal components of the measured data [26, 29]. Typically many components are required to faithfully represent input reflectance [32]. Therefore, building a complete low-dimension perceptual space that explains the appearance of measured material data is still an open question.

Even though millions of entries may be acquired to capture material appearance, many research projects have demonstrated that the underlying embedding of the real-world measured material

data is of substantially lower dimension. This result provides the foundation for building a low-dimension perceptual space and relating human perception to the reflectance embedding. Inspired by the most recent work for parameterization of measured material manifolds [32], we can build a mapping between the compact latent variables and the measured bidirectional reflectance distribution function (BRDF) data using the Gaussian Process Latent Variable Model (GPLVM). Compared to previous approaches applying linear dimension reduction techniques to the BRDF data, using GPLVM requires fewer latent space dimensions to faithfully reproduce measured materials. For example, linear dimension reduction requires 45 dimensions to accurately reconstruct a chromatic material sample from MERL dataset [26], while parameterizing the BRDF manifold with GPLVM only needs five dimensions.

In this chapter, we take advantage of the GPLVM model and propose a solution to build a low-dimension perceptual space for measured material data using perceived appearance similarity as a metric. We start by collecting crowdsourced data by conducting a psychophysical experiment. Particularly, we ask participants to select two out of three given examples that have similar appearance for each trial on Mechanical Turk. The measured materials are selected from multiple datasets to cover a large variety of appearance including both isotropic and anisotropic samples. Due to the large number of stimuli, we adopt an adaptive sampling scheme similar to that introduced in [33, 34] to keep the number of triplets manageable. Given the human-labeled data, we use the non-metric Multi-Dimensional Scaling (NMDS) algorithm to evaluate the pairwise comparisons for each triplet. The NMDS model provides us a low-dimension embedding that represents the relative positions of each measured BRDF in the manifold. We carefully evaluate the embedding and map it to the measured material samples using GPLVM. It is worth noting that we can perform interpolation on the inherently non-linear perceptual manifold and it will end up with linear combinations of the measured data due to the properties of GPLVM [32]. Compared with the costly non-linear predicting models, this property makes it possible to efficiently edit the appearance using the proposed perceptual space.

To evaluate our solution, we build a slider based material appearance editing interface using our proposed perceptual space. To avoid the ambiguity of the perceptual terminology, we do not name each dimension of the perceptual space. Instead, we provide the visualization of appearance variation along each dimension to help the user interpret the meanings of each dimension by themselves. We compare our interface with a traditional material editing interface with a physical-based reflectance

model through a user study. We perform the evaluation by comparing the time and accuracy of matching a target appearance on the two systems.

In summary, our contribution includes:

- A complete low-dimensional perceptual space built on the crowdsourced data that explains the visual appearance of measured material data.
- An analysis to interpret the perceptual embedding and how they are related to the physical reflectance data.
- An adaption of GPLVM to interpolate measured BRDFs using the perceptual embedding.
- An intuitive material editing interface using the proposed perceptual dimensions.

3.2 Related Works

3.2.1 Human Perception to Material Appearance

According to Dorsey et al. [35], material appearance can be defined as “the visual impression we have for a material”. There have been many previous works focusing on understanding the general process of human perception towards material appearances, and high-level reviews can be found in [36, 37, 38, 39]. Most of the work that has been done in the material perception area can be roughly categorized into three directions based on their different focuses: understanding individual factors on perception (gloss, translucency, shape, and so on), defining metrics to compare BRDFs perceptually, and building perceptual spaces using low-dimensional embedding.

Understanding Individual Factors on Perception. Studying material perception from a particular property helps to understand a certain type of material. Throughout the years, many research projects have been done to study the perception of gloss, such as [40, 4, 5]. Typically, they use the crowdsourced data to fit analytical expressions and create a perceptual parameterization of analytical BRDF models. Translucency is another perceptual attribute that is widely studied. Gkioulekas et al. [41, 30] provide thorough studies to understand different the impact of phase functions and edges on the perception of translucent materials. Gigilashvili et al. [42, 43] study the influence of geometry thickness on the human perception of translucency. Many other internal and external factors have

also been studied to understand their impact on perceiving material appearances, such as texture [44], viscosity [45], shape [46, 47], illumination [48, 49, 50] and motion [51].

Perceptual BRDF Metrics. Measuring the perceived difference between BRDFs is important for material recognition and classification. Many previous works have proposed different metrics to compare BRDFs based on human perception. Fores et al. [8] and Ngan et al. [7] put forward different perceptual metrics to evaluate measured BRDFs directly. Ngan et al. [52], Pereira et al. [53] and Sun et al. [54] focus their work on evaluating and comparing BRDFs in image space. They use images with rendered materials as a medium to build the metrics and compute the difference between material samples. Another promising direction to define the metrics based on the BRDF embedding, such as using MDS [5] or PCA [29]. Recently, Lagunas et al. [34] propose a learning-based solution for the overall material appearance to derive a similarity measure that correlates with the notion of material similarity as perceived by humans.

BRDF Embedding and Perceptual Space. Finding a low-dimensional representation for the high-dimensional BRDF data is the first step for building a perceptual space for material appearances. Many works have performed BRDF analysis and provided compact representations, such as spherical harmonics [55] and spherical wavelets [56]. However, to understand human perception of materials, we need to know the relative position of each material sample in the perceptual space. Therefore, the analysis should focus on the entire space of BRDFs. Typical works include linear dimension reduction approaches such as PCA [57] and nonlinear methods such as MDS. Many works build perceptual space using linear dimension reduction approaches such as [4, 26]. However, according to [26] linear approaches are unable to identify sufficiently small subspace to facilitate practical exploration, while nonlinear methods can only generate compact embeddings without explicitly providing mappings between the measured space and the manifold [32]. The study closest to our work is [29]. They create a perceptual control space by asking users to rate material appearances with 14 adjectives and the map the crowdsource data to the principal components of the measured BRDFs using Radial Basis Function. Different from their work that analyzes perceptual traits based on a high level and possibly ambiguous English words, we collect data based on the perceived similarity of the appearances. In [29] their perceptual dimensions are not independent due to the RBF mapping between PCA and the 14 perceptual parameters. Adjusting one parameter will change the underlying principle components, which leads to the change of values of other parameters. By comparison,

our perceptual dimensions are consistent and independent thanks to the GPLVM, which has proven effectiveness for BRDF completion by interpolating across BRDFs in an ad-hoc latent/perceptual space [32].

3.2.2 Material Editing

Many works have been devoted to the design and development of material editing applications due to the emergence of different shading models and user interaction mechanisms. We will consider material editing models from three perspectives: physical-based models, perceptual-based models, and the editing interface.

Editing Materials based on Physical Models. Currently, many off-the-shelf software products use physical-based shading models as the foundation for material editing, such as Maya [2] and Blender[3]. Users can change the material appearance by tweaking the parameters of analytical BRDF models. BRDF-shop [58] is a prototype that allows users to design an artist-friendly editing framework based on an extension of the Ward model. Talton et al. [59] explore the parameter space of the anisotropic Ashikhmin mode and use it to create an editing system. Shi et al. [15] (discussed in later in Chapter 6) propose a learning-based solution to edit bi-scale materials for fabrication purposes. There are many other works that focus on efficient editing of analytical BRDF models with fast feedback for lighting changes [60, 61, 62]. While using physical models to edit the appearance can provide accurate simulation results, the parametric space is not intuitive and consistent with human perception. The change of specific parameters may lead to subtle appearance changes that humans cannot detect.

Editing Materials based on Perceptual Models. With more and more research studying how the human visual system perceives material appearance, editing materials in perceptual space becomes possible. Pellacini et al. [5], Westlund et al. [6] and Wills et al. [4] propose different applications to edit the gloss attribute of the material. Boyadzhiev et al. [63] develop an image-based material editing system using intuitive attributes. As mentioned previously, Serrano et al. [29] propose an intuitive control space based on the perceptual space they have developed. Mylo et al. [64] introduce an interface to edit spatially-varying material by connecting a link between certain perceived visual properties and specific bands in its spectrum of spatial frequencies of a wavelet decomposition.

Editing Interface and User Interaction Besides shading models, the user interface and platform

also play an important role in the editing process. Most of the material editing systems mentioned so far are slider based interfaces, where users can change the parameters of material model by dragging sliders. However, the disadvantage of the slider based models is that users can only access to the results in the current state represented by the sliders. Users can be easily confused by different dimensions and forget the big picture of the entire space. Many other interfaces and prototypes are also developed to improve the intuitiveness of the material editing. One of the examples is image navigation, which provides users with a group of materials with certain variations. Instead of modifying parameters, users can browse through the materials and pick the one that is closest to their goals. Other lines of work [65][52] and software [66] further explored this idea and developed interfaces based on it. Another example is the Augmented Reality material editing interface proposed by Shi et al. [16] (discussed in Chapter 5), where the real environment rather than synthetic images is provided as background to visualize the appearances. Kerr et al. [1] introduce a user study to compare slider based systems and image navigation. Different from previous work, we propose a novel interface that combines the slider-based system with a variation of the image navigation system to help users understand the parameter space of the perceptual dimensions.

3.3 Goal

Before we provide the technical details, we want to first define the goal and scope of our work. According to Fleming et al. [37], the underlying visual processing of material appearance can be broadly grouped into two computations: categorization and estimation. Categorization is to assign a specific class label to a given material, while estimation is to identify the characteristics of the material. Our work focuses on the latter part. Our goal is to model a perceptual space to "locate" each material sample based on its surface reflectance properties and understand its relative position within its own class. Then we can visualize the space, interpret each dimension based on the visual clues, and edit the appearance by navigating through the perceptual dimensions. Due to the large number of material categories and their distinctive appearance, we narrow our study to the measured metal related materials collected from different datasets. However, we believe the methodology proposed in this chapter can be easily adapted to different material categories in the future.

The structure of the description is as follows. We first introduce the process of the user study to

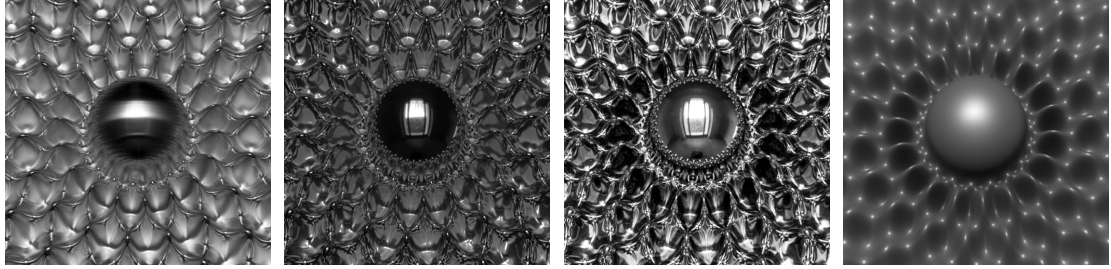


Figure 3.1: Example of stimuli of our psychophysical experiment.

collect crowdsourced data using Mechanical Turk in Section 3.4. In Section 3.5, we talk about how to learn perceptual embedding using the NMDS model with crowdsourced data. We introduce GPLVM to interpolate perceptual embedding and build perceptual space in Section 3.5. In Section 3.7, we introduce a novel material editing interface using the proposed perceptual space. We conclude with a discussion in Section 3.8.

3.4 Crowdsourcing Data Collection

In this section, we describe the design of a crowdsourcing experiment to collect user data on material appearance perception. We adopt the 2AFC scheme to ask users to select two images out of a triplet that has the most similar appearances.

Stimuli. We select 39 measured material data that is categorized as the metal from multiple datasets [26, 28]. The selected data covers a large range of appearance within the metal category. We choose the scene Havran-2 [46] to render the selected material samples since it densely samples the incoming and outgoing light directions and maximizes the information relevant for material appearance judgments. We use the Ennis environment map [67] for illumination and render the stimuli with Mitsuba [68]. Since our focus is the material perception caused by surface reflectance instead of color, we generate the achromatic stimuli by averaging the RGB channels to avoid bias for the user study. We note that the color channels can be easily integrated in the future by tweaking the a and b channels of the CIELAB color space, as proposed in [4, 29].

Participants. We used Amazon Mechanical Turk to recruit participants. A total of 360 paid participants took part in our experiment. Users were not aware of the purpose of the experiment.

Procedure. We decided to use a modified 2AFC scheme instead of the ranking method used in

[29] for our experiment, because of its simplicity and consistency in terms of providing numerical distances between stimuli [4]. Also, the perceptual space may be multi-dimensional and cannot be represented with a linear scale [34]. During the experiment, triplet images of the stimuli were presented to the subjects and they were asked to select any two images that share a similar appearance. Notice the method we used was slightly different from the traditional 2AFC where subjects only need to select from the two alternative candidates to match the reference. Based on the feedback from a pilot study using traditional 2AFC, we observed that subjects tend to choose randomly when they believe the two candidates are more similar. Therefore, we add that as the third option to cover all possible cases and avoid noise in the data.

Inspired by [33, 34], we adopted a similar adaptive sampling scheme to reduce the total number of triplets in our experiment. Ideally, 39 different stimuli yield around 30k comparisons, which would require a total of 150k responses if each comparison is evaluated by more than 5 subjects. However, this scale of the experiment is not feasible. Therefore, we turned to an adaptive sampling scheme to reduce the total amount of comparison to 6k. The sampling scheme selects a batch of triplets to maximize the information gain based on the previous iterations. In our case, we conducted 15 iterations and sampled 400 triplets for each iteration. The mean information gain reduced to 10^{-6} after the 15 iterations, confirming the convergence of the sampling scheme.

We conducted the experiment on Amazon Mechanical Turk. Before the subjects started the actual experiment, they were provided with a training session that included an additional 10 triplet test with obvious answers. Subjects who failed the training session (provided more than 2 wrong answers) were not allowed to start the experiment. Each qualified subject was asked to finish 110 triplets (100 tests and 10 validation) in total without a time limit. The 10 validation triplets were randomly selected from the 100 test triplets and the images were presented in a different order. Subjects were not aware of the validation triplets. If the results from the validation triplets could not reach 80% consistency, all test triplets from the same subject would be rejected. We introduced a delay mechanism for each triplet: the users could only make actions three seconds after the triplet was displayed. This mechanism makes sure that subjects take time to examine the images instead of making fast random clicks. In the end, there were 301 out of 360 subjects who provided valid results, yielding 30,100 responses.

3.5 Learning Perceptual Embedding

3.5.1 Non-metric Multidimensional Scaling

Given the results from the user study, our next step is to convert the triplet comparison into a low-dimensional embedding for each material sample that correctly represents the participants' answers. To be more specific, the Euclidean distance between the embedding of each BRDF should represent the perceptual distance obtained from the triplet comparisons. Therefore we seek a solution using multidimensional scaling techniques to solve the problem. It is worth noting that Lagunas et al. [34] propose a learning-based solution to extract 128 dimension feature vectors from triplet comparisons to predict the perceptual similarity between material appearance. However, their solution does not fit into our framework since we cannot interpret and edit the high-dimensional features intuitively.

Inspired by the work proposed in [4, 69], we decided to use the Non-metric MDS (NMDS) to evaluate the triplet comparison. We will briefly introduce our algorithm and implementation. The detailed proof can be found in the original NMDS paper.

We start from the triplet (i, j, k) representing the indices of material samples answered by subjects in our user study. We denote \mathbf{x}_i as the embedding for a material sample i , the matrix \mathbf{X} as embedding coordinates for all the material samples, and $D_{i,j}$ as the distance between the embedding of i and j . Given a triplet comparison from the subject, we can have

$$\begin{aligned} S_1 &= \{(i, j, k) | D_{i,j} < D_{i,k}\} \\ S_2 &= \{(i, j, k) | D_{i,j} < D_{j,k}\} \end{aligned} \tag{3.1}$$

Since each triplet is evaluated by at least 5 subjects in our experiment, we allow inconsistencies and repetitions between the set S . We can use the square of the distance to replace the original one since the distance is non-negative. We define the Euclidean distance using the Gram matrix $\mathbf{K} = \mathbf{X}^T \mathbf{X}$ as follows:

$$\begin{aligned} D_{i,j}^2 &= \|\mathbf{x}_i - \mathbf{x}_j\|_2^2 = \mathbf{x}_i^T \mathbf{x}_i - 2\mathbf{x}_i^T \mathbf{x}_j + \mathbf{x}_j^T \mathbf{x}_j \\ &= \mathbf{K}_{ii} - 2\mathbf{K}_{ij} + \mathbf{K}_{jj} \end{aligned} \tag{3.2}$$

K_{ij} represents the element in row i and column j from the Gram matrix K . Therefore, we can represent the inequality from a set S as

$$\begin{aligned}
D_{i,j}^2 &< D_{j,k}^2 \\
\mathbf{K}_{ii} - 2\mathbf{K}_{ij} + \mathbf{K}_{jj} &< \mathbf{K}_{jj} - 2\mathbf{K}_{jk} + \mathbf{K}_{kk} \\
\mathbf{K}_{ii} - 2\mathbf{K}_{ij} + \mathbf{K}_{jj} + 1 &\leq \mathbf{K}_{jj} - 2\mathbf{K}_{jk} + \mathbf{K}_{kk}
\end{aligned} \tag{3.3}$$

We obtain the third inequality by converting the second inequality from a strict one to a non-strict one. We can choose any other constant number to finish the conversion and it will only lead to a uniform scaling of the embedding. Therefore we use this constant to remove the scaling ambiguity.

Due to the rotation invariant property of the Gram matrix, we do not need to worry about the rotation ambiguity. However we still need to add constraints to eliminate the translation ambiguity. The simplest way is to limit the center of the embedding to the origin, where we have

$$\begin{aligned}
\sum_a (\sum_b \mathbf{x}_{ab})^2 &= 0 \\
\sum_{bc} \sum_a \mathbf{x}_{ab} \mathbf{x}_{ac} &= 0 \\
\sum_{bc} \mathbf{K}_{bc} &= 0
\end{aligned} \tag{3.4}$$

Therefore we can transform the constraint of the embedding to the Gram matrix.

Our goal is to find low-dimensional embedding from the triplet. The dimensionality of the embedding is the same as the rank of the matrix \mathbf{X} , and also equals to the rank of the Gram matrix \mathbf{K} . Also, the Gram matrix \mathbf{K} is semi-positive definite. Therefore, the problem becomes an optimization problem as follow:

$$\begin{aligned}
& \arg \min_{\mathbf{K}} \text{rank}(\mathbf{K}) \\
& \forall (i, j, k) \in S \quad \mathbf{K}_{kk} - \mathbf{K}_{ii} + 2\mathbf{K}_{ij} - 2\mathbf{K}_{jk} \geq 1 \\
& \mathbf{K}_{kk} - \mathbf{K}_{ii} + 2\mathbf{K}_{ij} - 2\mathbf{K}_{ik} \geq 1 \\
& \sum_{bc} \mathbf{K}_{bc} = 0 \\
& \mathbf{K} \geq 0
\end{aligned} \tag{3.5}$$

To handle the inconsistent results from the same triplet, we follow the method proposed in [69] to introduce slack variables ξ_{ijk} in every inequality constraint, which allows for violations of the inequality and augments the objective function to minimize the total violation. Also, we introduce λ to control the trade-off between the violation and the rank of the matrix. To deal with the non-convexity of the objective function, we relax the rank function to its convex envelope, the trace. A detailed discussion about this relaxation can be found in [4]. Therefore, the objective of our problem becomes:

$$\begin{aligned}
& \arg \min_{\mathbf{K}, \xi} \sum_{(i,j,k) \in S} \xi_{ijk} + \lambda \text{tr}(\mathbf{K}) \\
& \forall (i, j, k) \in S \quad \mathbf{K}_{kk} - \mathbf{K}_{ii} + 2\mathbf{K}_{ij} - 2\mathbf{K}_{jk} \geq 1 - \xi_{ijk} \\
& \mathbf{K}_{kk} - \mathbf{K}_{ii} + 2\mathbf{K}_{ij} - 2\mathbf{K}_{ik} \geq 1 - \xi_{ijk} \\
& \sum_{bc} \mathbf{K}_{bc} = 0 \\
& \mathbf{K} \geq 0 \\
& \xi_{ijk} \geq 0
\end{aligned} \tag{3.6}$$

Once the optimization is finished, we can compute the embedding from the Gram matrix \mathbf{K} by applying the eigen-decomposition:

$$\begin{aligned}
\mathbf{K} &= \mathbf{U}\mathbf{\Sigma}\mathbf{U}^T \\
\mathbf{X} &= \mathbf{U}\mathbf{\Sigma}^{\frac{1}{2}}
\end{aligned}
\tag{3.7}$$

As for implementation, We use Matlab with the SeDuMi solver [70] to solve the optimization problem. The SeDuMi is a convex optimization solver that is designed to solve semi-definite problems. The average convergence time for our optimization problem is around 200 seconds on a standard PC with an AMD Ryzen 7 1700X 8-core CPU and 16 GB RAM.

3.5.2 Model Selection

In this section, we want to evaluate the choice of λ and the dimension of the embedding. λ represents a tradeoff between the rank of the Gram matrix \mathbf{K} and the number of violations in the triplets due to the conflict responses from different subjects.

We conduct cross-validation to perform the model selection and evaluate the influence of λ on the inference accuracy. We split the subjects' responses into the training set and validation set by the ratio of 4:1. We apply the cross-validation 10 times for each value of the λ from 0 to 100. For evaluation purposes, we define the error of each model as the percentage of mismatches between the inference results and the majority user response of the corresponding triplet comparison. Fig. 3.2 demonstrates the average training and validation errors over 10 cross-validation experiment for different λ values. We expect to see the training error monotonically increases with the λ because larger λ means the optimization focuses on reducing the rank of the matrix \mathbf{K} and allows more violations to happen. When the $\lambda = 100$, the optimized rank of matrix \mathbf{K} is 2. However, when the $\lambda = 0$, the optimization entirely focuses on reducing the number of violations, leading to smaller training errors. But the average rank of the matrix \mathbf{K} is 32, which means possible overfitting. Also, this is not consistent with our goal of building a low-dimensional embedding. The validation error first decreases and then increases. The error reaches the minimum point at $\lambda = 26$, representing the model that has the best generalization performance to deal with the violations. At this point, the first four dimensions of the embedding have 99.2% of the variance compared with all dimensions, indicating that we can build a 4D perceptual space.

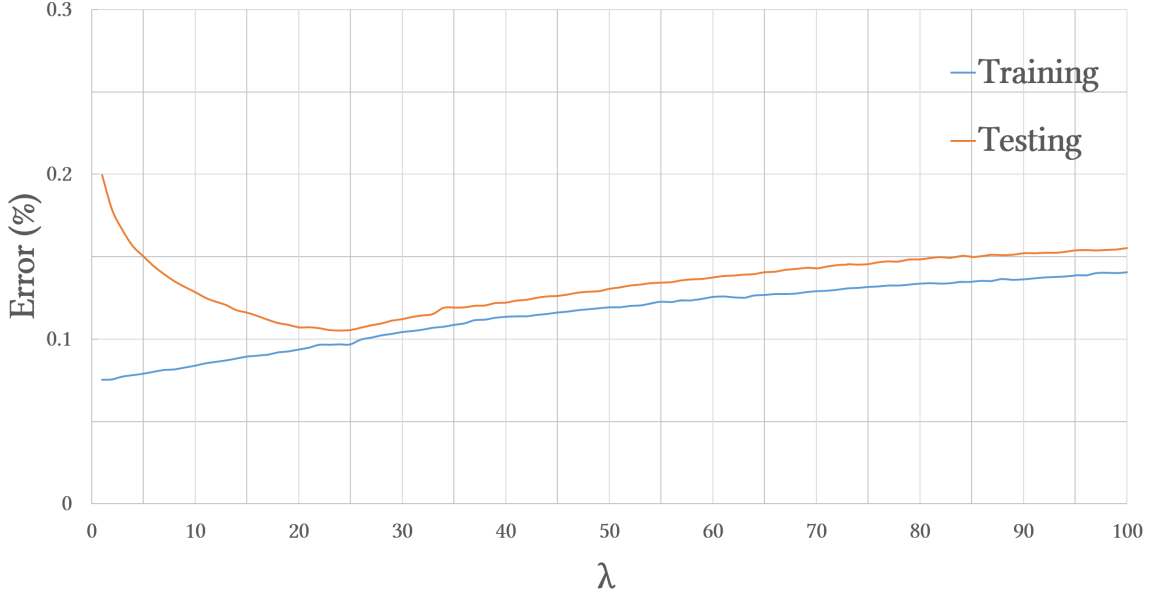


Figure 3.2: Training and testing errors (percentage of violation) for different λ in Cross validation.

3.6 Building A Perceptual Space

The perceptual embedding we have learned from the user responses provides the coordinates of measured material samples on a 4D perceptual manifold. However, they are discrete and separated. We want to define a continuous perpetual space that can map any coordinates on the manifold to the reflectance data. In this section, we talk about how to achieve this by interpolating the material samples with GPLVM and analyze each interpolated dimension of the perceptual space.

3.6.1 Perpetual Interpolation Using GPLVM

We use GPLVM as a regression model that takes as input the perceptual coordinates and outputs the 4M measured BRDF data in the same format as the MERL dataset. The advantages of using GPLVM can be summarized as follows:

- It provides a non-linear mapping between low-dimensional latent space and high-dimensional data.
- It provides a uniform linear interpolation for the data, regardless of the choice of latent variables and their dimension.

- The interpolated data is continuous as long as the covariance/kernel function used in the Gaussian Process is continuous.

We use the GPLVM model introduced in [32] to perform the perpetual interpolation. For the mathematical proofs and derivation of GPLVM please refer to [71]. In our case, we denote $\mathbf{Z} \in \mathbb{R}^{N \times 4M}$ to be the matrix of the measured BRDF data used as stimuli in our experiment and $N = 39$. We use matrix $\mathbf{X} \in \mathbb{R}^{N \times 4}$ to represent the optimized 4D perceptual embedding computed from the NMDS. Given a random coordinate in the perceptual space \mathbf{x}_* , the goal is to predict the corresponding BRDF \mathbf{z}_*

$$\begin{aligned}\mathbf{z}_*^T &= \mathbf{b}_{\mathbf{x}_*}^T \mathbf{Z} \\ \mathbf{b}_{\mathbf{x}_*}^T &= \mathbf{v}_*^T \mathbf{V}^{-1} \\ \mathbf{v}_* &= [c(\mathbf{x}_0, \mathbf{x}_*), c(\mathbf{x}_1, \mathbf{x}_*), \dots, c(\mathbf{x}_{N-1}, \mathbf{x}_*)]^T\end{aligned}\tag{3.8}$$

Although $\mathbf{b}_{\mathbf{x}_*}$ is non-linear with respect to the perceptual embedding, the extrapolated data is still linear for the measured BRDF data \mathbf{Z} . \mathbf{V} is the covariance matrix whose elements are $V_{ij} = c(\mathbf{x}_i, \mathbf{x}_j) \quad \forall V_{ij} \in \mathbf{V}$. c is the kernel function that can be specified by the user and is key to modeling the non-linearity of the underlying function. Following [32], we define c as a shifted squared exponential function because of its smoothness and local support, which leads to smooth transitions for the predicted BRDFs.

$$c(\mathbf{x}, \mathbf{x}') = \mu \delta(\mathbf{x}, \mathbf{x}') + e^{\frac{-\|\mathbf{x} - \mathbf{x}'\|^2}{2l^2}}\tag{3.9}$$

where l and μ are hyperparameters that correspond to the characteristic length scale and noise-filtering parameter respectively. According to [71], a high value for l leads to a smoother function, and a small value for μ can significantly improve numerical stability for inverting \mathbf{K} . Based on the analysis proposed in [32], we set $l = 1$ and $\mu = 10^{-4}$.



Figure 3.3: Visualization of each perceptual dimension that is interpolated using GPLVM.

3.6.2 Visualization and Analysis

For visualization, we continuously interpolate BRDFs along each perceptual dimension using GPLVM and render their appearance. To be more specific, the perceptual coordinates of the 39 stimuli provides a bounding box to define the maximum and minimum value for each dimension. We interpolate one dimension at a time and fix the coordinates of the other three dimensions at the center for better visualization. We demonstrate the results in Fig. 3.3

The images on each row depict how the BRDFs vary with the increase of a specific perceptual coordinate. For Axis 1, the major variation is the specularity. The highlight becomes sharper and the whole appearance turns to be even more glossy. For Axis 2, we can observe the changes in the greasing angles. The edge of the sphere changes from bright to dark as the increase of Axis 2. Axis 3 captures the specular shape and anisotropy. Notice the vertical part of the highlight starts from the clear and regular dot and ends up as stretchy lines. The variation for Axis 4 depicts the increase of the diffuse part while maintains the shape and intensity of the specular part.

Notice that the components of the perceptual coordinates are in the decreasing order of the variance computed from the Gram matrix \mathbf{K} , which represents the importance of each dimension in terms of explaining the perceptual space. In our case, Axis 1 is the most important dimension that explains how humans perceive the appearances of the stimuli, and Axis 4 is the least important one. This result provides some interesting insights that align with our intuition on how humans perceive different characteristics of the metal materials. The changes of shininess and glossiness in Axis 1

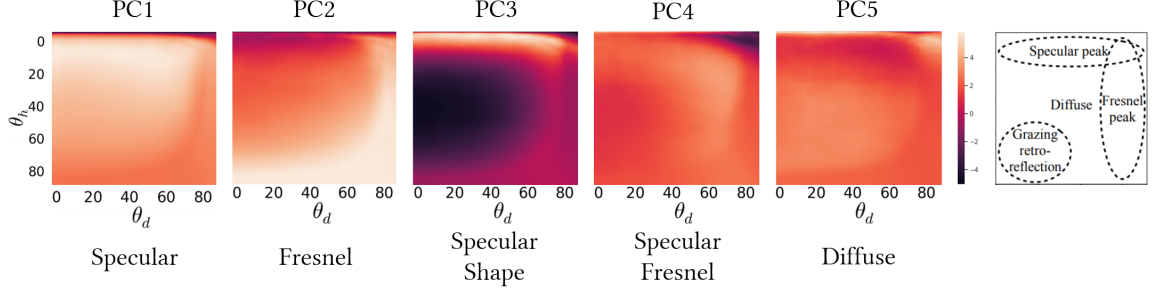


Figure 3.4: BRDF-slices of the first 5 principal components of the 39 metal BRDF stimuli and a slice reference.

demonstrates that humans are most sensitive to the intensity of highlights when recognizing metal materials. The second important thing is the reflectance caused by the Fresnel effect, which can be explained by human sensitivity towards the edge of an object. In comparison, the appearance variation displayed in Axis 3 is less significant compared with the first two, indicating that the shape of the highlight and anisotropy are subtle clues for human perception. The results in Axis 4 show that when the highlight remains the same, the appearance change of the rest part does not make a significant difference in perception, which further demonstrates the importance of the highlight. However, we also want to mention that the last observation could possibly happen for recognizing metal materials only since all the materials used for stimuli are glossy to some extent, which overshadows the influence of the diffuse component.

We also want to demonstrate the proposed perceptual embedding is consistent with the low-dimensional embedding of the BRDF data. We compute the PCA of our 39 stimuli using the method presented in [57] and visualize the scaled first 5 principal components in 2D slice [72]. Fig. 3.4 shows the results. As we can see that the interpreted meaning of each principal components and their importance coincide with our perceptual embedding. This result further convinces the consistency of the underlying embedding between our perceptual model and physical reflectance data. However, it is worth mentioning that we cannot directly map the perceptual embedding to the first 5 principal components of the BRDFs using GPLVM and then apply reconstruction, since the first 5 PC cannot fully reconstruct the original appearance, especially for materials with high specularity and anisotropy. Fig. 3.5 shows an example. Also, we do not notice a significant visual difference between our method and mapping to high dimensional PC (such as 35D).

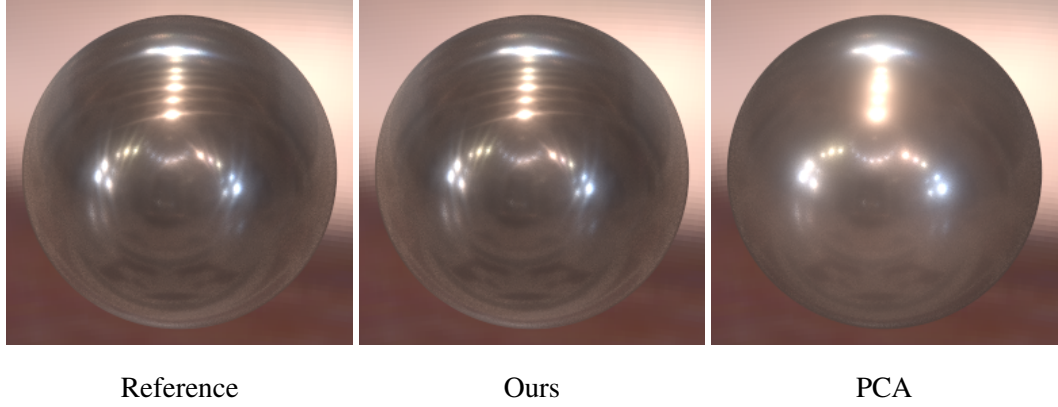


Figure 3.5: Comparison between our method and mapping perceptual embedding to the first 5 principle components and then perform reconstruction.

3.7 Perceptual Editing Interface

With the proposed perceptual space, our next step is to build an intuitive material editing prototype that can take advantage of the low-dimensional embedding. In contrast to previous material editing interfaces, we do not want to represent each dimension with a single word that users may interpret in different ways. Even the words that are used to describe physical attributes of materials (such as specular, roughness, etc) may be abstract for novice users, and may be ambiguous due to their different meanings and interpretations for different analytical BRDF models. For perceptual dimensions, it is even more difficult to find ubiquitous and intuitive words to interpret them. Traditional methods rely on fitting the perceptual dimensions with physical attributes, but this could lead to ambiguity and inconsistency.

Inspired by the image navigation interface proposed by [52], we want to use the appearance variation to define each perceptual dimension. To be more specific, for each dimension, we present to users a series of images with variations corresponding to the uniform steps in our perceptual space. By observing the image variation, users are expected to understand and interpret each perceptual dimension by themselves. However, according to the results from the user study [1], we know that compared with the sliders, users have relatively poor performances using the interface with only image navigation in material editing. Therefore, we propose a trade-off solution that combines the image-navigation with sliders to create an intuitive editing interface.

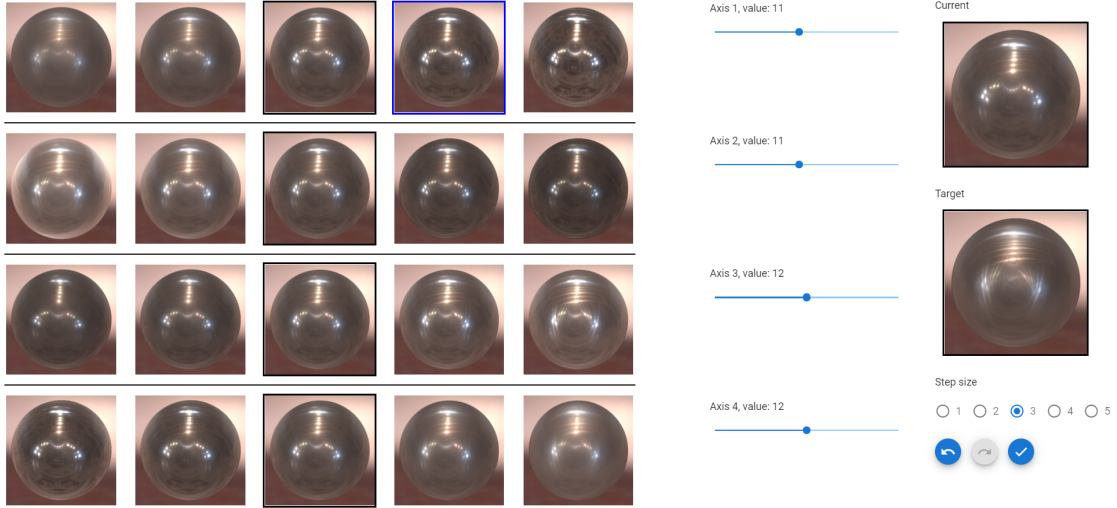


Figure 3.6: Example of our proposed user interface.

3.7.1 Interface Overview

Fig. 3.6 gives an example of our user interface, which includes three sections: image navigation (left), sliders (middle) and utilities (right).

The image navigation section provides a 4×5 image grid, and each row represents the variation of the increasing value for the corresponding axis. For example, there are 5 different variations to demonstrate how the material appearance can vary along the first axis, and their coordinates of the first axis are increasing from left to right. The other three coordinates for all the 5 images on the first row are fixed for the other 3 axes. There is no direct correlation between the images on the same column but different rows, except the middle column, which represents the users' currently selected material. Once an image is selected, it will be presented in the center of each row, and the rest of the images in the grid will be updated iteratively. We provide different step sizes to control the granularity of differences between two adjacent materials on the same row. The 4 axes in our interface represent the 4-dimensional perceptual space. Given this interface, users can navigate through the entire perceptual space incrementally and iteratively. Essentially, it is a simplified 1D version of the original 2D image navigation reported in [52]. However, we believe this simplification is necessary since with the help of the sliders users do not need to deal with axes selection, which is the most confusing part that makes the original image navigation less effective according to [1].

We also provide users with a slider to help them quickly locate the desired material and fine-tune

its appearance. The slider and image navigation are codependent: changes on either one will lead to the update on the other one. The design concept is to provide users more options and information to interact with the material in a straightforward manner. For example, users can drag sliders to quickly visualize the changes along each axis and directly select the desired images from the grid.

For the utility section, users can visualize their current selected material on the right. For evaluation purposes, we also present a target material appearance for appearance matching tasks. We also provide redo and undo features to help users restore a previous or forward state of the design.

3.8 Discussion and Conclusion

In this chapter, we have proposed and analyzed a low-dimensional perceptual space for measured metal materials. Our study covers diverse material appearances collected from different datasets. We have conducted a large-scale psychophysical user study and gathered over 30K valid answers from 360 participants. We evaluated the responses using an NMDS model to extract perceptual embedding for each material sample. We map the perceptual embedding to the reflectance data using GPLVM to interpolate the BRDFs, which provides a continuous perpetual space for appearance editing. We have further designed and implemented a novel intuitive material editing interface that takes advantage of the proposed perceptual model.

There are a few limitations in our study and there is future work needed. The first limitation is the material category. As we have discussed in previous sections, we only focus on understanding human perception of metal materials in this work due to their special visual appearance. We could have incorporated more materials with different categories into our study but that would introduce noise for the embedding. In fact, a key advantage of our flexible methodology is that it can be applied to different types of materials (such as plastic and cloth, etc.) and we can build individual perceptual spaces with unique attributes for each material category, which we believe will provide more insights on material recognition and perception. Another limitation is the small size of the measured BRDF datasets. Even though we have covered a large range of metal materials, there are still many more materials that display unique appearance in real life. With the emergence of new material acquisition and capture techniques, we hope to introduce more metal BRDF and SVBRDF into our study in the future. And last, we hope our proposed editing interface could inspire additional research on

intuitive material design and interaction. The paradigm of material editing is similar to color picking but with more complexity and high dimensionality. However, few efforts have been made to improve the intuitiveness and accuracy of the interface for material editing.

Chapter 4

The Role of Subsurface Scattering in Glossiness Perception

4.1 Introduction

In this chapter we consider attributes that are typically presented for adjustment in material appearance editors. For an intuitive editor the attributes should be easily recognized and should be independently adjustable. In particular we consider whether the attributes of gloss and translucency can be considered as independent perceptual attributes for editing.

Humans are adept at identification of materials [73, 74] and can easily characterize their appearance [42, 73]. A typical human with a normal vision does not need much effort or prior training to tell the difference between shiny and matte objects, or whether a material transmits light. Assessment of material appearance has a vital importance in our daily lives - just by visual inspection, we know whether food is edible or spoiled, whether the road is slippery or not. Tactile expectations derived from the visual appearance can guide our haptic interaction with the surrounding objects - for instance, we touch glossy, transparent crystal-looking objects with more care than we do for jelly-looking, matte objects expecting the latter to be soft and elastic, while the former is deduced to be fragile. How the human visual system (HVS) calculates these appearance properties from the physical stimulus is far from being fully understood. Comprehending the physical processes and inverting optics [75], as well as the calculation of image statistics by our brain [76] have been named

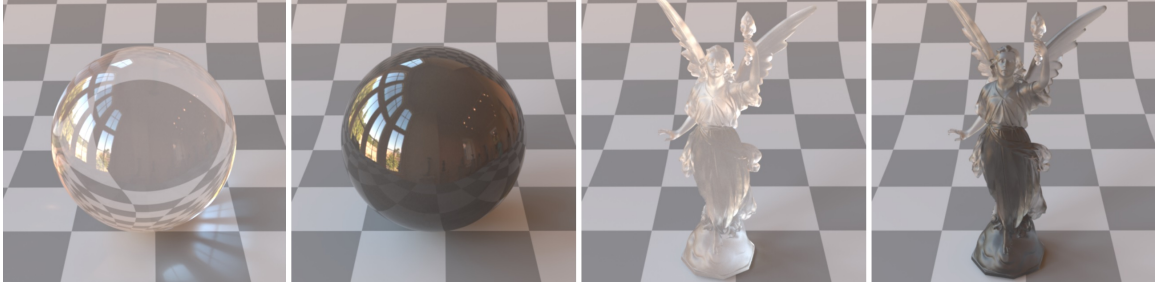


Figure 4.1: Examples of materials and shapes used in the study of the impact of subsurface scattering on gloss.

among the potential explanations, both criticized on several grounds [31, 77, 37].

Gloss is among the most important visual attributes of a material [78, 79]. It is usually associated with shininess [80] due to the specular reflection and is formally defined as an *"angular selectivity of reflectance, involving surface reflected light, responsible for the degree to which reflected highlights or images of objects may be seen as superimposed on a surface"* in the ASTM Standard Terminology of Appearance [81]. The six distinct dimensions of gloss: specular gloss, contrast gloss, distinctness-of-reflected-image gloss, absence-of-bloom gloss, absence-of-surface-texture gloss, and sheen, have been proposed by Hunter et al. [82] back in 1937. Since then, gloss has been accepted as a surface-related quality and perception of gloss has been studied in the context of surface scattering models [5, 4, 83]. Various image cues have been proposed to be used by the HVS for gloss perception (for instance, the total area covered by specular reflections, contrast between specular reflections and surrounding areas, the sharpness of the edges of the specular regions [84, 85]). Although it has been demonstrated that shape and illumination co-vary with the image cues proposedly used for gloss estimation [85], these cues can also be affected by the subsurface light transport.

Traditionally, the studies addressing gloss perception have been limited to surface reflection and fully opaque media (e.g. [5, 4, 83, 86, 87, 88, 89, 84, 85, 67, 90, 47, 91]), while a lot of materials we interact with on a daily basis, are both glossy and light-transmissive - water, glass, marble, or human skin can be named among many. The knowledge about the peculiarities of gloss perception on transparent and translucent materials is very limited.

In this chapter, we hypothesize that subsurface scattering impacts glossiness perception. The hypothesis is reasoned from the following notions:

1. Due to the limited dynamic range and poor capability of the HVS to comprehend and invert

the complex optical path of the light [31], human observers might have difficulty unmixing transmitted and surface-reflected light. Hence, caustics, direct transmission or volume scattering can be mistaken for specular reflections. Imagine a transparent crystal vase with a complex shape. It shines, has sparkles and highly luminant areas. Is it possible to tell whether the highlights are due to the reflection, direct transmission or subsurface scattering of light? Do not all these shiny parts evoke a feel of glossiness regardless of their origin?

2. It has been demonstrated that darker objects look glossier than lighter ones [5, 83] due to higher contrast between specular and diffusely-reflecting areas (Hunter’s contrast gloss [82]). As volume scattering and absorption can impact the contrast between specular and non-specular areas, they might also impact apparent gloss.
3. Observation of the mirror-like reflection image on the surface has been identified to be a strong glossiness cue [80] (Hunter’s distinctness-of-reflected-image gloss). While it has been thought to be correlated with surface roughness only [5], the distinctness of the reflected image can be dependent on light transmission properties as well. The same applies to the sharpness of the highlights, which is another glossiness cue [84, 85].
4. Subsurface light transport can influence the size of the highlights on complex-shaped objects. It has been demonstrated multiple times that the size of the highlights is correlated with perceived glossiness [92, 84, 85, 93].
5. For transparent objects, as the transmitted and reflected light integrate, overall luminance reaching the human retina is higher and the object shines more [42, 80]. Overall shine as an inherent characteristic for gloss, might evoke a perception of glossiness.
6. Finally, caustics and light transmission might facilitate material identification. If a stimulus is associated with a familiar, usually glossy material, the expectations about this material can impact the perception of glossiness [94].

In order to test this hypothesis, we have conducted a series of pair-comparison experiments. In the first (pilot) experiment, we studied how surface and subsurface scattering affect gloss perception on the example of spherical objects. The results of the pilot experiment have indicated that the impact

of subsurface scattering on gloss varies among different levels of microfacet-scale surface roughness. This can be explained by the fact that glossiness cues vary dramatically between mirror-like and Lambertian-like surfaces [82, 86, 90]. We have interviewed several participants (members of our lab) in the pilot study. They noted that if the shape of the stimulus were different, it could have affected their answers. This correlation was deemed reasonable by us, as the macro-scale shape of the object can impact translucency and subsurface light transport [31, 42, 43]. In order to investigate further, the second experiment was arranged, studying objects with five different shapes each with five different levels of surface roughness. We analyzed the depth and curvature of object shapes and identified interesting trends in how the contribution of subsurface scattering to gloss varies among object shapes. Our contributions in this chapter are the following:

- We experimentally test the hypothesis that subsurface scattering impacts gloss perception for materials with identical shape and identical surface scattering.
- We identify whether the contribution of subsurface scattering to the glossiness perception varies among different macro-scale and micro-scale (microfacet-level) shapes, and characterize this impact qualitatively.
- We discuss the need for inclusion of subsurface scattering in future studies, opening a new avenue in gloss perception research.

The chapter is organized as follows: in Section 4.2, we summarize the related work. In Sections 4.3-4.4, we present the two experiments and their results, respectively, followed by the Discussion section (Section 4.5). Finally, we summarize the conclusions and overview the open points for future work.

4.2 Related Work

The perception of gloss and translucency has attracted scholarly interest in vision, psychology and computer graphics alike. While substantial progress has been achieved on both topics, the two attributes have usually been studied separately from each other.

4.2.1 Gloss perception

One of the most widely discussed hypotheses about gloss perception is that the HVS calculates skewness of luminance histogram or a similar measure of asymmetry when assessing gloss [76, 95, 96]. Interestingly, many glossy objects have positively skewed histograms. However, it has been shown by Anderson et al. [97] that non-glossy images can also produce similar histograms and image statistics do not fully explain the complex neurophysiological processes of gloss perception (e.g. [77, 98, 96]). Other widely studied image metrics that are proposedly related to gloss are contrast [5, 83, 84, 85], sharpness [5, 84, 85] and coverage area [92, 84, 85, 93] of the highlights. The glossiness of a given material has been demonstrated not to be constant and can vary to a great extent, e.g. across different shapes [47, 99, 84]. In some particular cases, even Lambertian surfaces are capable of evoking gloss perception [90, 86, 100]. Gloss has been shown also to be impacted by illumination geometry [67, 99], motion [89, 101, 51] and color [102, 89]. Pellacini et al. [5] have used multidimensional scaling (MDS) and identified two perceptual dimensions of gloss that are similar to contrast and distinctness-of-image. They conclude that *"darker objects look glossier than lighter ones"*. Wills et al. [4] tried to embed bidirectional reflectance distribution functions (BRDFs) into the perceptual space. These perceptual dimensions have been modeled with physical material properties in Ward's reflectance model [20], ignoring subsurface light transport. Toscani et al. [91] have recently proposed that surface reflection has at least three perceptual dimensions: lightness, gloss, and metallicity. However, the authors did not address how these dimensions behave on highly transparent and translucent media.

4.2.2 Translucency perception

Translucent appearance is a result of subsurface scattering for the materials where the light can penetrate into the volume. Although Chadwick et al. [103] have reported yet imperfect still reasonable perceptual unmixing of absorption and scattering by humans in "milky tea" images, Fleming et al. [31] argued that the HVS has poor ability to reconstruct complex processes of light and matter interaction and instead it relies on simple image cues to perceive translucency. These cues co-vary with various properties of an object. Image cues as well as the amount of light exiting the volume depend on the shape complexity and thickness of a given object. For instance, it has been shown

that sharp geometric details of the object impact apparent translucency [104] and the other way round, translucency affects perception of geometric edge sharpness [105]. Sawayama et al. [106] have reported that *"sensitivity to translucent discrimination was high when the object has rugged surfaces"*. Furthermore, Gigilashvili et al. [42] have observed that objects with thin parts look more translucent and that the HVS is more sensitive to translucency differences when an object has thin parts Gigilashvili et al. [43]. Nagai et al. [107] discussed luminance statistics of potential "hot spot" image regions that are especially informative about translucency. Later, particularly edges have been proposed to contain a vital portion of the information for translucency assessment Gkioulekas et al. [41]. Similar to gloss, the translucency of a material is not constant either. It has been shown to be dependent on the illumination geometry [108, 109] and shape [42, 31]. Gkioulekas et al. [30] have examined translucent appearance in the context of computer graphics and found that the phase function of volume scattering affects translucent appearance.

4.2.3 Impact of translucency on gloss

Gigilashvili et al. [42] reported no significant differences in gloss perception of five physical spherical objects with identical surface roughness but different translucency and color. The authors revisited the study in [80] and after analyzing the observer interviews, they discovered that different people rely on different cues. The authors have identified three groups of people with different approaches to solve the gloss-based ranking task. While objects with identical surface were automatically considered equally glossy by some subjects, two other groups used different cues for ranking, either overall shininess of the object - mostly present in transparent and translucent spheres, or distinctness-of-image and contrast - that were higher for more opaque ones. When the experiment was conducted using complex-shaped objects instead of spherical ones [80], the majority of the observers considered translucent objects glossier than their opaque counterparts. The authors hypothesize that this happens due to the complex shape, which generated more caustics and back-reflections for translucent and transparent materials, while lacking distinctness-of-image for the opaque ones. They refer to the reasoning by Fleming et al. [31] about poor optics inversion ability of the HVS and propose that subjects might have mistaken caustics for specular reflections. If that is possible for physical objects during direct interaction, confusion can be even larger in computer graphics, where haptic interaction is impossible and tactile information is absent. It is worth mentioning that these works have been

primarily of a qualitative nature. To the best of our knowledge, this is the first work quantitatively evaluating the impact of translucency on gloss.

4.3 Experiment 1: Pilot Study

4.3.1 Methodology

Objectives

The objectives of this experiment are two-fold: firstly, we test a hypothesis that subsurface scattering impacts gloss perception when surface scattering and object shape are identical; secondly, we observe how surface and subsurface scattering impact perceived gloss together.

Stimuli

We began our study by considering different scenes to use for our experiments. For illumination, we followed the previous work [30] using the side-lighting by rotating the environment map provided by Mitsuba [68] to a proper angle. We created synthetic images of spherical objects using a physically-based rendering in Mitsuba. Spheres have been widely used in the past for studying gloss perception (e.g. [5, 83, 42, 110, 67]). For surface reflectance, we used an isotropic rough dielectric microfacet model with the Beckmann distribution [68]. The model is defined by roughness *alpha* (the root mean square slope of microfacets) and an index of refraction *IOR*. As we restrict our attention to subsurface scattering effects, we use a fixed *IOR* of 1.5 which is typical for translucent media such as glass, wax and polymeric materials [111, 112]. All objects were placed on a Lambertian checkerboard. The experiment was conducted in two rounds: since our primary goal was to explore whether subsurface light transport influences gloss perception, in the first round we compared objects with an identical surface roughness parameter (also referred to as *alpha*) and different parameters of subsurface scattering. In order to explore how the impact of volume scattering on gloss perception varies among the different levels of surface roughness, we have repeated the experiment for the different *alphas* separately. In the second round, we compared the stimuli with different *alphas*. We select roughness from the set $\{0, 0.05, 0.1, 0.25, 0.5\}$ to cover a wide range of surface reflectance behavior. Some of the stimuli are illustrated in Fig. 4.2-4.3.

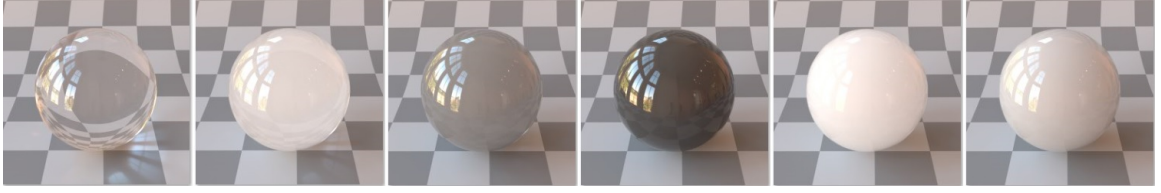


Figure 4.2: Sphere examples with the same surface roughness but different subsurface scattering properties.



Figure 4.3: Sphere examples with the same subsurface scattering properties but different surface roughness.

We used a homogeneous isotropic subsurface scattering model to simulate the translucent appearances. For this pilot we assume an isotropic phase function and wavelength-independent scattering and absorption for subsurface light transport. The subsurface scattering parameters are the extinction coefficient σ_t and *albedo*. For the extinction coefficient, we found through experimentation that increasing σ_t over 10 does not yield significant differences in appearance for our shape because the material becomes opaque. Therefore, we selected $\sigma_t \in \{0, 0.1, 0.5, 1, 2, 3, 4, 5, 10\}$. For albedo we selected $albedo \in \{0.01, 0.1, 0.2, 0.3, 0.4, 0.5, 0.6, 0.7, 0.8, 0.9, 0.95\}$. Such a dense sampling of parameters covers a wide range of appearance but would require an enormous number of comparisons to be evaluated. Many pairs of parameter values lead to indistinguishable appearances, which are redundant for the user study. To select a smaller set of parameter combinations for stimuli with the same surface reflectance, we used the K-means clustering algorithm to find six distinctive clusters based on different subsurface scattering parameters. We used the averaged Euclidean distance of pixels from the rendered images as a metric to perform K-means clustering. We have explored other clustering algorithms, such as affinity propagation [113], but K-means has provided the best clustering results according to the silhouette coefficient. We used the cluster center as our stimulus for the user study. Since the K-means has been conducted separately on different groups of surface roughness, the cluster centers were not identical for all surface roughness levels. The variation in the cluster centers was small, however, and so we selected identical subsurface scattering parameters

for all levels of surface roughness. 30 different stimuli were used in total (5 different levels of surface roughness and 6 different combinations of σ_t and albedo). We used the volumetric path tracing integrator of Mitsuba to render the stimuli with 512×512 pixel resolution and 16384 samples per pixel. The tonemapped (clipped) low dynamic range images have been used to ensure the compatibility with the user displays.

Experimental Design

We considered two different designs of 2 alternative forced-choice task: either displaying two stimuli and asking the subjects (also referred to as users) to select a glossier stimulus, or displaying three stimuli and asking to select two stimuli closer to each other in terms of gloss (a setup similar to Wills et al. [4]). We ran a preliminary study with both designs. 8 members of our lab completed the tasks and participated in informal post-experiment interviews. 7 subjects out of 8 mentioned that selecting a glossier stimulus between the two was an easier task than comparing the three by similarity. They also admitted that oftentimes they had found it difficult to isolate gloss from total appearance and were tempted to judge similarity by overall appearance or lightness. Therefore, we selected the former option for the task design.

First, we conducted separate paired-comparison experiments for each level of *alpha*. The users were shown two spherical objects with the same surface roughness and different subsurface scattering parameters. They were asked to select the one with a glossier appearance. The proper command of English among subjects was ensured with the Amazon Mechanical Turk average approval rate filter (see section 4.3.1). Only the users with a positive track record of similar tasks were allowed to participate. The following instruction was given to them: **"Select the image with the glossier object."** No further definition or guidance was provided. The reason for abstaining from a definition is the following: any particular definition for *gloss* could have biased subjects' decisions. For instance, as mentioned above, the ASTM Standard Terminology of Appearance [81] defines *gloss* as *"angular selectivity of reflectance, involving surface reflected light, responsible for the degree to which reflected highlights or images of objects may be seen as superimposed on a surface."* Reference to the definition that highlights gloss as a *reflectance* property might have had an implication for some subjects that *subsurface scattering effects* should be ignored. This contradicts the objective of this experiment. The research objective of this study was the identification of the factors impacting

the overall sensation of gloss, not the psychometric measurement of an internal function for a given visual cue. It is worth mentioning that seminal works on gloss perception (e.g. [5, 4]) usually have no mention that the term was defined for the subjects, unless the objective is a psychophysical measurement of a particular, explicit cue (such as *specular contrast* and *specular sharpness* in [85]).

There was no time limit for each trial. Each user was asked to complete 100 trials in random order, of which 75 were unique trials (6 different materials yield 15 trials for each roughness level, totalling to 15×5) and 25 were repeated trials with images in reverse order. We used the repeated trials to assess *intra-rater reliability* by counting the number of pairs (out of 25) the subject selected the same stimulus on both trials. We designed our system with a delay mechanism: the users could only select the candidate image two seconds after the pair was displayed. This mechanism makes sure that users take time to examine the images.

To understand how surface reflectance and volume scattering influence gloss perception together, we conducted a second round of paired-comparison experiments, where the two candidate images had different surface roughness. Instead of dividing the 30 stimuli into 5 groups and conducting experiments separately for each roughness level, this time the users had to compare the stimuli from different roughness groups, yielding 360 unique pairs in total (each of the 30 stimuli was compared with other 24 stimuli of different *alpha*; from the first round of the experiment we already had the data for the objects with the same *alpha*). 25% of the pairs were shown twice for controlling *intra-rater reliability*.

Analysis: Hypothesis testing

We formulate a null hypothesis that subsurface light transport has no impact on gloss perception. In order to test the null hypothesis, we conducted Binomial exact statistical significance tests, as our outcome is binary. Under the null hypothesis, the expected probability of each stimulus being considered glossier is 0.50. We assess observed frequencies and calculate the probability of observing those frequency values when the null hypothesis is true. As it is not important at this stage which of the two stimuli is glossier (we just want to show that subsurface scattering makes them look different in terms of gloss), we conduct a two-tailed test - i.e. it does not matter whether the observed frequency is larger or smaller than the expected one. If the probability of observing given frequencies is less than 0.05 under the null hypothesis, the difference is deemed significant and the null hypothesis is

rejected. In order to avoid falsely rejecting the null hypothesis due to multiple testing (type I error), we applied Holm-Bonferroni [114] correction to the data.

Analysis: Z-scores

A further method to analyze the pair-comparison data is Z-scores (Standard scores) [115, 116]. It is based on Thurstone's law of comparative judgment [117] - assuming that each sample has a quality that is being assessed by a subject and these qualities are Gaussian random variables. Each time a subject compares the two samples, realizations from both random variables are drawn and compared, selecting the one with higher quality. The probability of selecting a given option is found using the standard normal cumulative distribution function (CDF). The inverse CDF of the standard normal is a Z-score showing how many standard deviations away is a given option from the mean. Usually, Thurstone's simplified Case V model is used assuming that all samples are independent and have equal variance [116]. For all samples we present the mean Z-scores and their 95% confidence intervals as error bars (calculated using MATLAB Colour Engineering Toolbox [118]). The mean Z-score shows how far a given stimulus is from the mean of the set of stimuli being assessed. If the 95% confidence intervals of the Z-scores do not overlap, we can tell with 95% confidence that the qualities of the two stimuli are significantly different.

Subjects

The sample size is found by desired statistical power, significance level and effect size for the Binomial null hypothesis testing. The desired statistical power was set to 0.8 (the probability of rejecting the null hypothesis when the alternative hypothesis is true) and the significance level was set to 0.05 (the probability of falsely rejecting the null hypothesis when it is actually true). As per the null hypothesis two stimuli are equally glossy, the expected probability is 0.5. In order to decide on alternative proportion, two different effect size metrics [119] were used: Cohen's g - usually used for the cases where the expected proportion is 0.5 and simply found as a difference between the proportions, and Cohen's h - that is found as:

$$h = 2(\arcsin \sqrt{p_1} - \arcsin \sqrt{p_2}) \quad (4.1)$$

where h is Cohen's h (sometimes reported as an absolute value) and p_1 and p_2 are the two proportions. Under an alternative proportion of 0.75, $g=0.25$ and $h=0.52$, being interpreted by Cohen [120] (cited in [119]) as large and medium effect sizes, respectively. Thus, we set an alternative proportion to 0.75. Considering these values, the needed sample size was approximated as 29.

We conducted our experiments on Amazon Mechanical Turk (MTurk) and collected responses from 50 users per pair. In total, around 250 subjects participated in both rounds. The users were compensated for participation. In order to ensure the reliability of the users, two filters were applied: firstly, only the MTurk users with an average approval rate above 50% were allowed to participate; and secondly, the participants were ranked by their performance in the *intra-rated reliability* test, i.e. by the consistency of their responses on the validation set (how many times they selected the same stimulus in the pairs shown twice). Eventually, 30 most consistent subjects were considered per stimuli pair, around 150 subjects in total, all of them demonstrating at least 70% consistency. In addition to that, the results with concurrent clicks from the same IP address were discarded, because it was impossible to calculate their intra-rater reliability and to identify how many unique subjects were responding.

4.3.2 Results

The results for the fixed roughness experiment are shown in Fig. 4.4-4.5. Fig. 4.4 shows that the difference is significant and the null hypothesis can be rejected for a substantial number of image pairs. This is especially true for smooth objects. The number of pairs that are significantly different gradually decreases, but for $\alpha = 0.50$ it starts increasing again. While the two-tailed Binomial tests can just tell whether the difference is significant, the Z-score plot in Fig. 4.5 illustrates which stimuli have been deemed glossier. If the null hypothesis were true, all stimuli were expected to end up with similar Z-scores. However, the observed trend is consistent with the Binomial tests - the difference among some stimuli is significant and it is large for smooth objects while the difference gradually diminishes but starts increasing again for the highest α . The materials either with low σ_t or albedo were considered glossiest, while the ones with high albedo turned out less glossy. The results including all comparisons among the 30 stimuli are shown in Fig. 4.6-4.7. The significance table shows that the vast majority of the differences between different roughness levels are significant, while no significant differences are usually observed among the objects with the same roughness.

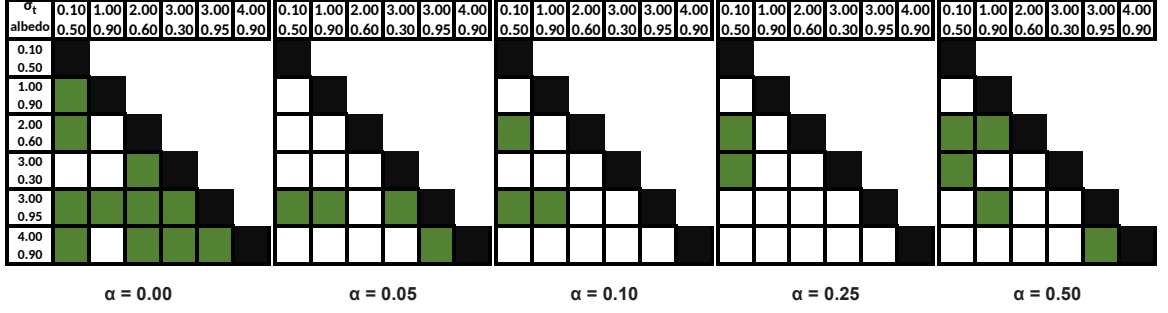


Figure 4.4: Significance tables for each roughness level for Experiment 1.

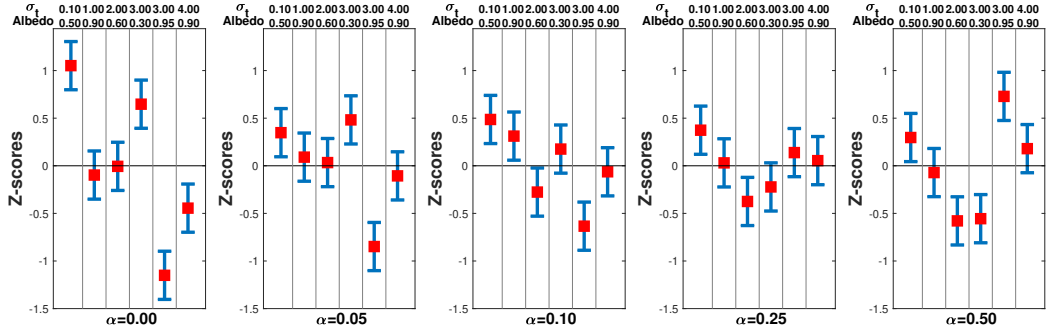


Figure 4.5: Z-scores for fixed roughness experiments.

However, there are a few exceptional instances - the materials with high albedo (0.95) are not significantly glossier than some other objects with a rougher surface (Fig. 4.6).

A clear trend is visible in Z-score plots (Fig. 4.7) - with the increase of surface roughness, the perception of glossiness is decreasing monotonically, being consistent with the prior works [121, 87]. It is worth noting that although it is the identical data, the Z-score differences among the stimuli within each roughness group decreases when considered together with all other stimuli (compare Fig. 4.5 and 4.7). This can be explained by the fact that a Z-score for a given stimulus is relative and depends on the judgment against all other stimuli in the set. Within a larger pool of stimuli and various *alphas*, the subjects tend to focus more on the surface reflectance instead of the subtle effects of subsurface light transport. All these observations demonstrate that even though the subsurface light transport has an impact, the surface reflectance still plays a major role in the perception of glossiness.

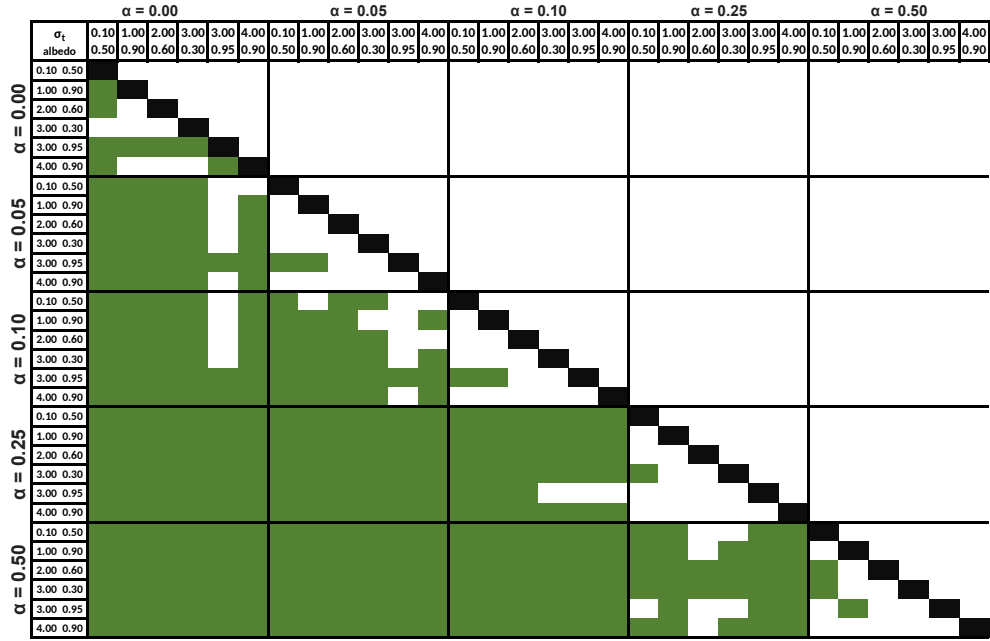


Figure 4.6: The significance table for all 30 stimuli.

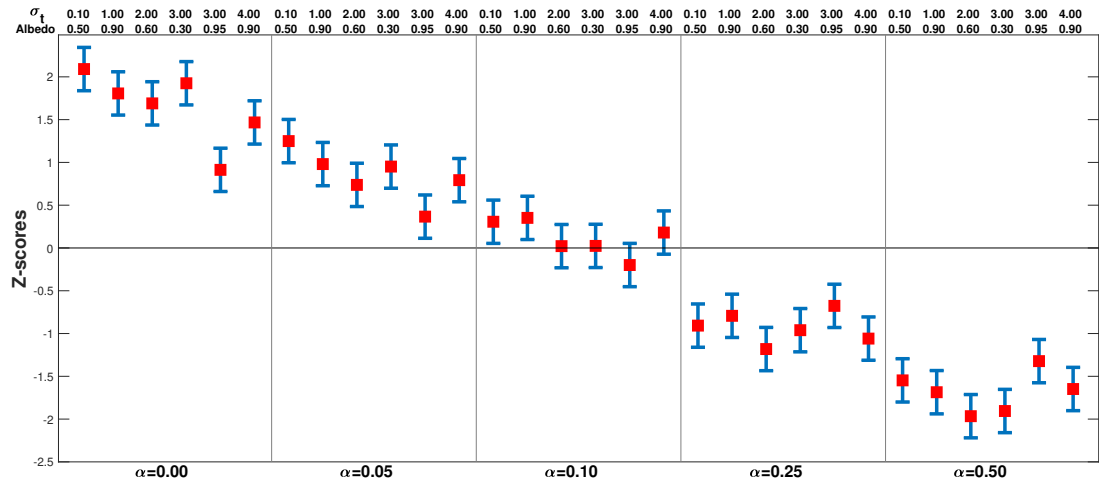


Figure 4.7: Z-scores for the comparisons of all 30 stimuli.

4.3.3 Discussion

While surface roughness has a strong negative impact on gloss (being consistent with [5, 83]), for numerous pairs of the stimuli with identical surface roughness, we have rejected the null hypothesis and observed a significant gloss difference induced by subsurface scattering of light. The way subsurface scattering impacts gloss perception differs among different levels of surface roughness and changes non-monotonically.

When *alpha* is low and σ_t is high, gloss increases as the albedo decreases. With a high extinction coefficient, the subsurface light penetration is reduced, yielding appearance closer to diffuse reflectance. This scenario can be paralleled with a diffuse component in Ward’s surface reflectance model: decreasing the diffuse reflectance leads to glossier appearance - proposedly, due to increased contrast, making our observations consistent with that of Pellacini et al. [5].

When the stimuli are rough (high *alpha*) and do not have strong glossiness cues (such as specular highlights), caustics or the overall shinier look created by high volume scattering could potentially be considered a glossiness cue. This might explain why people can still tell the difference between the stimuli with high *alpha* in our experiments, and why Lambertian surfaces are capable of evoking perception of glossiness [86, 87]. In general, the stimuli with low σ_t and *alpha* were selected as the glossiest. The caustics and back-reflections from the background might be reasons for this (a similar trend has been observed for some subjects in Gigilashvili et al. [42, 43]). Furthermore, the glass-like appearance can also evoke a stronger perception of glossiness due to material identification and the association with the properties of a familiar material, as proposed by Schmid et al. [94]. Several important points have been learned from this experiment that guided the subsequent experiments:

- Since the way subsurface light transport contributes to gloss depends on the surface scattering, we decided to study this contribution for each surface roughness level individually.
- If the change in surface scattering induced by subtle changes in microfacet slopes has a dramatic impact on the behavior of subsurface scattering, we believe the same will be true for macro-scale changes of the object shape. Therefore, we decided to study the contribution of subsurface scattering for multiple different shapes individually and to compare the trends among them.

4.4 Experiment 2: Impact of Shape

4.4.1 Methodology

Objectives

Experiment 1 provides evidence that subsurface scattering can impact gloss perception for spherical objects, and this impact depends on the amount of surface scattering. The objective of Experiment 2 is to quantitatively study whether subsurface scattering impacts glossiness perception in shapes other than a sphere, and to explore qualitatively how these effects vary with the shape complexity expressed in depth and curvature.

Stimuli

The same scene and rendering technique was used as in Experiment 1. In order to study a broad spectrum of stimuli, we varied the same three parameters as in Experiment 1 and also the shape of the object, where $shape \in \{sphere, spiky\ sphere, Stanford\ Lucy, low\ resolution\ Lucy, cylinder\}$ and $alpha \in \{0, 0.05, 0.1, 0.25, 0.5\}$.

The sphere had already been studied in Experiment 1, while Experiment 2 was conducted on four new shapes. Several factors were considered when selecting the shapes: we need a shape that differs from a sphere by surface complexity and curvature, i.e. does not have large curved areas and does not reflect the mirror image of the environment (if you pick it up, you cannot see yourself); has many fine details; is not compact, has thin parts that transmit light well; we selected the *Lucy* from the Stanford 3D Scanning Repository STANFORD, as it satisfies these conditions and has been used in other works for studying the appearance of translucent materials (e.g. [30]). Afterwards, we wanted to isolate several features and selected the following objects: is as thick as a sphere but has more complex surface geometry - *spiky (bumpy) sphere*; has little thickness, similar to *Lucy*, has thin parts, but lacks fine details, has relatively simple surface geometry and lower curvature - the *low-resolution Lucy*; the main body is as thick as that of *Lucy*, but lacks thin parts and has very simple surface geometry and a very low curvature - a *cylinder*. The objects are illustrated in Fig. 4.8.

We defined the initial pool of subsurface scattering properties as $\sigma_t \in \{0, 0.1, 0.5, 1, 2, 3, 4, 5, 10\}$ and $albedo \in \{0.01, 0.1, 0.2, 0.3, 0.4, 0.5, 0.6, 0.7, 0.8, 0.9, 0.95\}$. We performed a clustering pro-



Figure 4.8: Five different shapes have been studied throughout the experiment. Left to right: sphere, spiky sphere, Stanford Lucy, low-resolution Lucy and cylinder.

cess similar to that used in Experiment 1 (described in section 4.3.1). As the clustering was conducted for each individual shape and surface roughness, the cluster centers were not identical among them. Although the difference was negligible among the surface roughness levels, it was substantial between the sphere and the Lucy. Therefore, we selected two sets of $[\sigma_t\text{-albedo}]$ pairs, $\{[0.1, 0.5]; [1.0, 0.9]; [2.0, 0.6]; [3.0, 0.3]; [3.0, 0.95]; [4.0, 0.9]\}$ for spiky sphere (identical parameters had already been used for a sphere in Experiment 1), and $\{[0.5, 0.8]; [1.0, 0.4]; [3.0, 0.4]; [3.0, 0.7]; [3.0, 0.9]; [5.0, 0.1]\}$ for the Lucy, low-resolution Lucy and the cylinder.

Experimental Design

The experimental design was identical to the first round of Experiment 1. The objects were compared only with the objects of similar shape and *alpha*.

Analysis

Similarly to Experiment 1, Binomial tests were conducted to test the null hypotheses for each pair, and Z-scores were calculated to assess the big picture. In addition to this, a scatter plot of Z-scores as a function σ_t and albedo was plotted to identify how these individual parameters of subsurface light transport affect gloss. Finally, we used the variance of the Z-scores and the number of significantly different pairs for a given shape and *alpha*, to compare the magnitude of the subsurface scattering impact on perceptual gloss. The shapes have been quantified in terms of *depth* (thickness) and *surface curvature*. The 3D models were presented in dimensionless units - the radius of a sphere was considered 1, and all other shapes were quantified relative to that. *Depth* was defined as a range of coordinates in all three dimensions separately, covered by the point cloud of a given object. *Local surface curvature* (Gaussian and mean) has been calculated for all points on the object

surface [122, 123] and average values have been reported.

Subjects

The procedure was identical to Experiment 1.

4.4.2 Results

With this experiment, we wanted to answer three questions:

1. Does subsurface scattering affect gloss for object shapes other than a sphere?
2. How does the impact of subsurface scattering on gloss co-vary with surface roughness for object shapes other than a sphere?
3. How do σ_r and albedo relate with the perceived glossiness and how does this differ across the shapes?

Does subsurface scattering impact gloss?

In Experiment 1 we demonstrated with spherical objects that subsurface scattering impacts gloss perception. The results for the Lucy are shown in Fig. 4.9-4.10. Although the results are not one-to-one comparable with that of a sphere due to the differences in subsurface scattering parameters, the following contradiction in the overall trends still stands out (compare with Fig. 4.4-4.5): the impact is subtle for smooth Lucy objects and the contribution of subsurface scattering increases with *alpha*, while the opposite is true for spherical objects. The null hypothesis was rejected for 13 out of 15 pairs when *alpha*=0.5, while it was rejected for one pair only when *alpha*=0. The results for the spiky sphere and low-resolution Lucy closely follow the trends of a sphere and Lucy, respectively. Interestingly, a cylinder was the least affected object by the change in subsurface scattering.

Impact of alpha across different shapes.

We compared the variance of the mean Z-scores, as well as the number of statistically significantly different pairs (out of 15) for each shape and *alpha*. The results are shown in Fig. 4.11. As expected, the results are very consistent between the two metrics. The large variance of the Z-scores or the

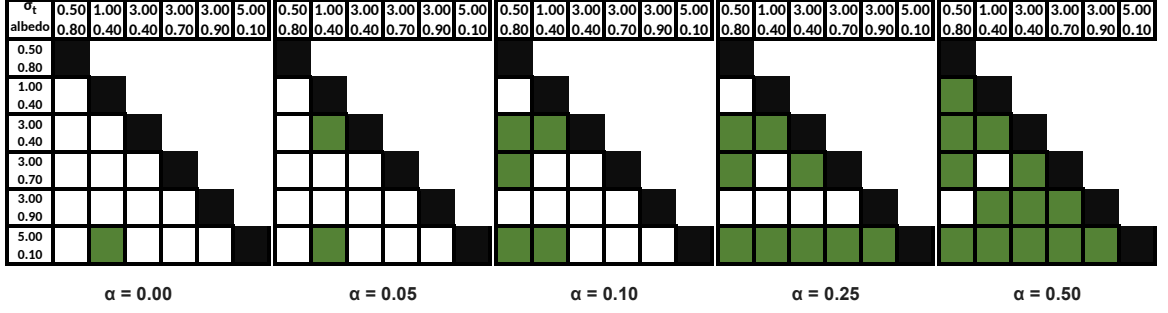


Figure 4.9: Significance tables for each roughness level of Lucy.

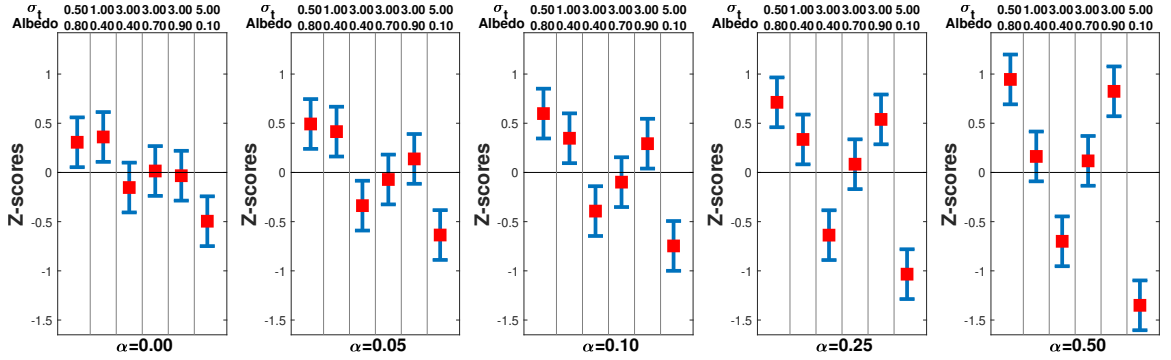


Figure 4.10: Z-scores results for Lucy. The difference among Z-scores grows with the increase of roughness.

higher number of significantly different pairs means that the variation in subsurface scattering leads to larger gloss differences. The σ_t and albedo parameters used for rendering, although subtly, still differ between a sphere and spiky sphere, on the one hand, and the Lucy, the low-resolution Lucy and the cylinder, on the other hand. This makes it challenging to directly compare the results between the two groups. However, we can still observe how the variance changes with *alpha* for a given shape. For spherical objects, the impact of subsurface scattering on gloss is larger when *alpha*=0. The impact gradually diminishes as *alpha* increases, but interestingly, the impact starts climbing again when *alpha*=0.5. Conversely, the impact of subsurface scattering on Lucy-shaped objects increases with the *alpha*. It is also worth noting that the cylinder remains the least affected object for all *alphas*.

Gloss, σ_t and albedo.

Till now the impact of subsurface scattering on gloss perception was discussed as a whole, single phenomenon. However, for modeling purposes in the future, it is of vital importance to identify how each particular physical attribute relates to the perceived gloss. Mean Z-score as a function of σ_t

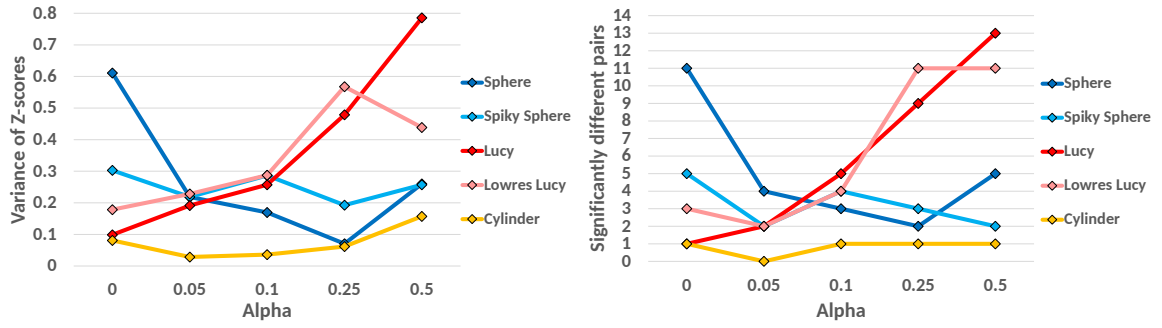


Figure 4.11: The variance (left) of the mean Z-scores and the number of significantly different pairs (right).

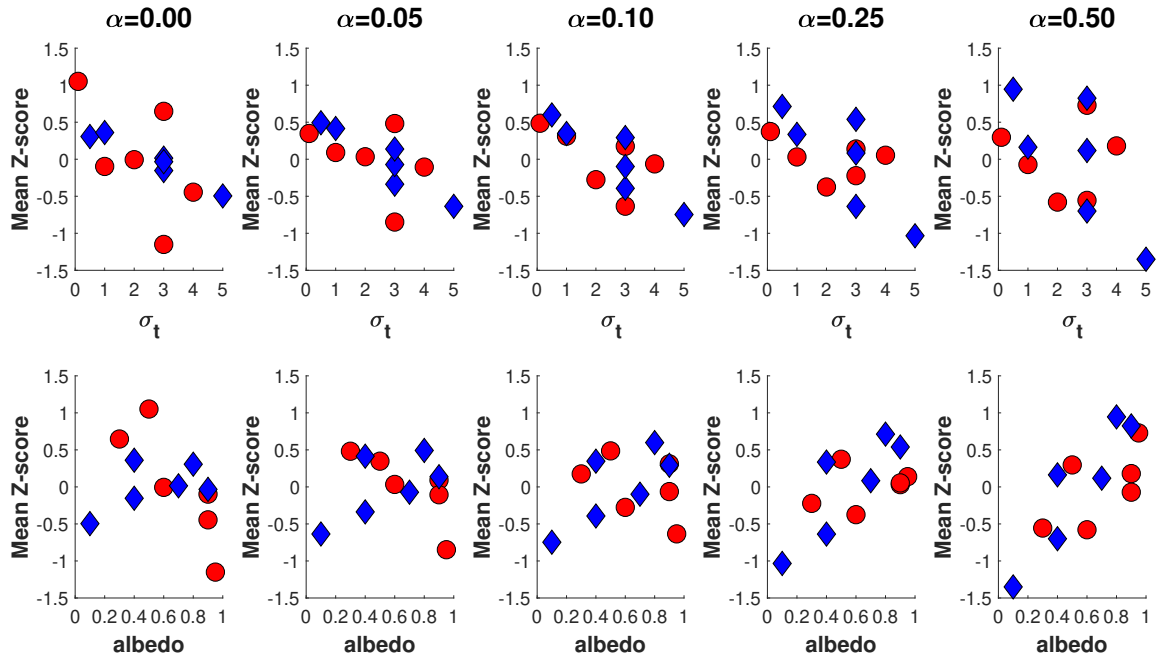


Figure 4.12: Z-score as a function of the extinction coefficient (top row) and albedo (bottom). Sphere (red circles) and Lucy (blue diamonds).

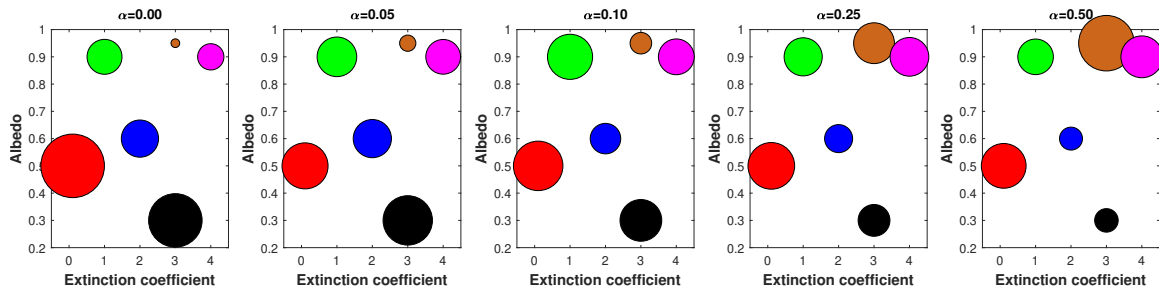


Figure 4.13: Z-score results for Sphere. Larger circle diameters represent a higher mean Z-score.

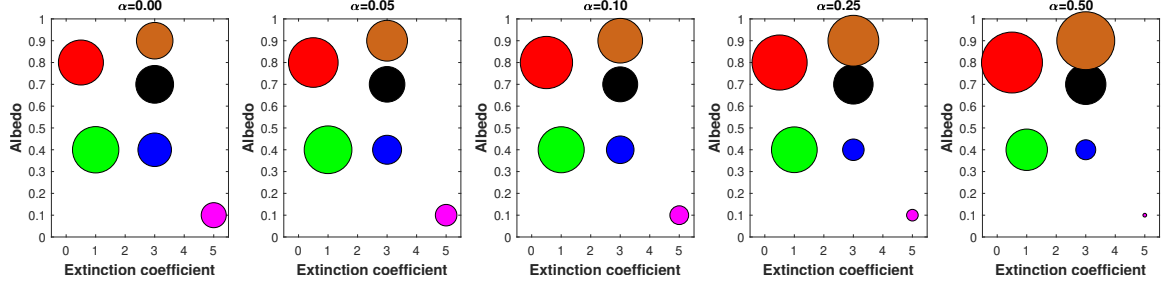


Figure 4.14: The results for Lucy. High albedo and low extinction coefficient usually yield glossier stimuli.

and albedo for sphere and Lucy is shown in Fig. 4.12, and the mean Z-scores in the σ_t -albedo space is shown in Fig. 4.13-4.14. Interestingly, for Lucy, there is a negative linear correlation between Z-scores and σ_t , and a positive linear correlation between Z-scores and albedo. As for the sphere, the albedo is negatively correlated with Z-scores when *alpha* is low, but it becomes positive for large *alphas*. We can see on Fig. 4.13-4.14 that the increase in *alpha* has a negative impact on low albedo materials for both shapes and a positive impact on high albedo ones.

4.4.3 Discussion

The object shapes come in different surface curvature and thickness (depth). The thickness of the objects is normalized to a unit sphere radius and is shown in Table 4.1. It is an important parameter, because the extinction coefficient is meaningful in terms of object size - the larger the distance light needs to travel within the medium, the larger the probability of absorption and scattering is. In other words, object depth directly impacts the appearance of the dielectric materials. This explains why the trends are similar between a sphere and a spiky sphere, as well as Lucy and low-resolution Lucy. Only subtle differences have been observed between a sphere and a spiky sphere, and between Lucy and low-resolution Lucy. However, an essentially different trend has been observed in cylinders, even though its thickness is nearly identical to the body of Lucy. This observation indicates that thickness does not account for all differences caused by shape and surface complexity - thus, curvature should also be considered.

Local surface curvature has been found on all points of the 3D object and an average value has been calculated. The curvature at a given point can have a positive or a negative sign. However, we are primarily interested in how rugged the overall surface is, and not in the directionality of the

Table 4.1: The depth of the objects in X, Y and Z dimensions.

	X	Y	Z
Sphere	2.00	2.00	2.00
Spiky Sphere	2.09	2.10	2.10
Lucy	0.94	1.48	2.73
Lowres. Lucy	0.88	1.48	2.68
Cylinder	0.45	0.45	1.90

Table 4.2: Gaussian curvature (GC) and mean curvature (MC) are found locally for each point of the 3D object.

	GC	MC
Sphere	1	1
Spiky Sphere	742.81	22.48
Lucy	22691.61	58.44
Lowres. Lucy	89.11	7.61
Cylinder	0	2.48

curvature, neither in convexity or concavity of the shape. Therefore, the average has been calculated among absolute values. The curvature measure is summarized in Table 4.2. Note that both Gaussian and mean curvatures are equal to 1 for a unit sphere, and Gaussian curvature is equal to 0 for a cylinder. marlow et al. [85] demonstrate that the weighted average of sharpness, contrast, and size of the highlights account for most of the variance in gloss judgements. The authors argue that these cues are constrained by the macro-, meso-, and microscale shape of the object. For instance, specular sharpness can vary as a function of curvature, as *"specular reflections will be sharpest in image regions that run parallel to local directions of high curvature, and will be most shallow (stretched) along directions of low curvature."* Their experiments have shown that higher curvature leads to higher specular sharpness and contrast, thus - higher glossiness, albeit the correlation with specular coverage is subtle. However, their findings are based on fully opaque media. Sharpness and contrast will certainly be dependent on the light exiting the volume after subsurface light transport. The curvature of the surface can also influence the coverage area (size of the highlights) due to subsurface scattering, as it has been the case for high albedo Lucy in our experiment (image C in Fig. 4.15). This indicates that their findings are not directly transferable to translucent materials. In the future work, cross-shape comparisons are needed (e.g. sphere with Lucy) in order to identify whether objects with higher curvature look glossier for translucent objects as well.

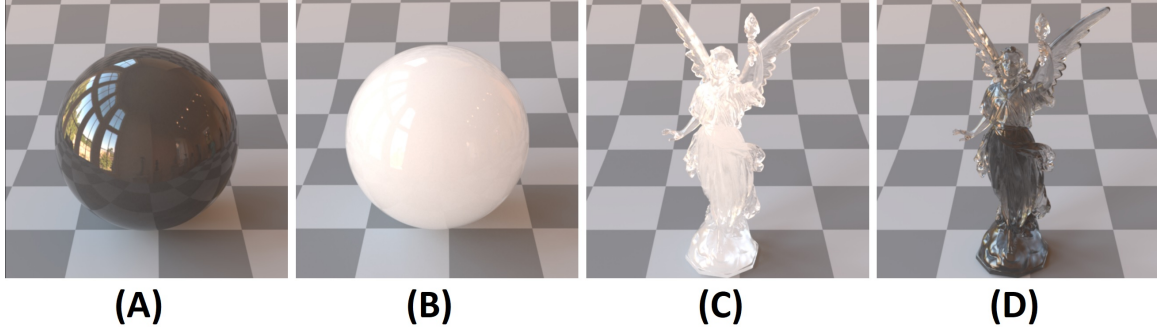


Figure 4.15: Comparison between objects with identical shapes and surface roughness but different albedo of subsurface scattering.

Interestingly, for low curvature objects, low σ_t materials (transparent) and materials with high σ_t and low albedo (dark opaque) are considered glossiest. We conducted an additional experiment with 15 smooth spherical objects and applied the nonclassical nonmetric multidimensional scaling analysis (MDS) with raw user response frequency as a distance matrix. From the extracted features, we can see that transparent low σ_t and dark opaque materials were placed close to each other in 2D embedding. The same trend holds for higher dimensions. Marlow et al. [85] also see similarities between the two types of materials and propose that similar mechanisms might be used in both cases, as the clear image of the surrounding "*inside or behind the depth*" of the object body is visible in both cases - although one is the result of direct transmission, while the other is a mirror reflection image. The mirror reflections on dark opaque objects are intuitively associated with perceived gloss, but the link between the background image seen-through the transparent media and gloss certainly deserves further study.

Curvature could however explain the primary difference, as well as similarities in trends between a sphere and a spiky sphere (although we have not compared them directly). For low alpha, a low albedo dark opaque sphere (image A Fig. 4.16) is among the glossiest, while that is not that case for a smooth spiky sphere made of the same material (image B Fig. 4.16). This is because the high curvature of the spiky sphere does not permit a clear mirror reflection to be observed. On the other hand, the transparent object is the glossiest for both shapes (images C and D Fig. 4.16). However, the image cues differ dramatically between the two. The transmission image is not visible for a transparent spiky sphere (image D Fig. 4.16), but the curvature of spikes produces shiny highlights due to internal scattering (the resulting image is also affected by the limited dynamic

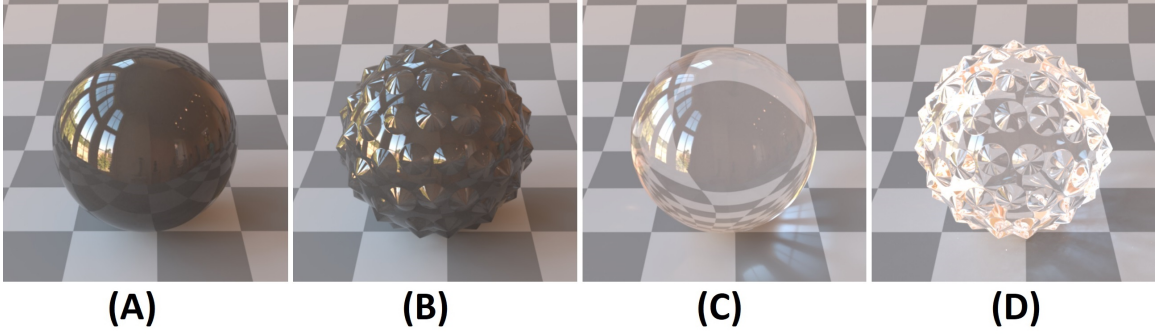


Figure 4.16: Curvature influences glossiness cues - thus, the perceived relative glossiness of the objects.

range). Similarly, the lower curvature of low-resolution Lucy makes transparent one glossiest for all alphas, while that is not the case for Lucy, as its curvature does not permit clear transmission.

4.5 Discussion

The effect of subsurface scattering was statistically significant for numerous material pairs. This is a clear indication that subsurface scattering is a contributing factor to perceived gloss and should be considered in future studies on gloss perception. However, this impact differs among the object shapes. We hypothesize that this difference comes from different image cues present in objects of different shapes and surface roughness. For more opaque smooth spherical objects lower albedo led to a glossier appearance. As the lower curvature of a spherical object produces a distinct reflected image of the environment, we believe that this is a widely used cue by the HVS for glossiness perception. The darker the object, the more distinct the reflected mirror image is. Besides, the contrast between specular and non-specular areas is also large and the reflections stand out more. This phenomenon is demonstrated in Fig. 4.15 - object A and B have an identical shape and surface roughness, but the subsurface scattering albedo of A is substantially lower, which makes it easier to observe the mirror reflection of the environment on it. This is consistent with the previous findings [5, 83]. As the sphere becomes rougher, the reflection of the environment, as well as specular reflections, disappear and the cues used for judgment of glossiness changes. As rough objects look all Lambertian and non-glossy, the difference among them decreases. However, objects with higher albedo look lighter and shinier, which could potentially become a cue for glossiness [121, 100, 86, 87]. While the impact of *alpha* on gloss is monotonic, the impact of subsurface scattering is not. Qi *et al.* [87]

have demonstrated the monotonic relationship between *alpha* and gloss, while they showed that the contribution of meso-scale roughness is non-monotonic. Further study is needed to explain why the impact is non-monotonic for spheres and why it starts increasing for $\alpha=0.5$. It is interesting that for smooth spheres, the materials with the lowest extinction coefficient looked glossiest. We have speculated above that the presence of the transmission image inside the object can be reminiscent of mirror reflection, while the association with familiar material (e.g. glass), as well as caustics could have also played the role.

For Lucy-shaped objects, the opposite trend was observed. Usually, the albedo was positively correlated with gloss, the extinction coefficient was negatively correlated, and the overall impact was increasing with the roughness. If we inspect the Lucy-shaped images, we will see that the surface geometry does not allow to observe a clear reflection image, neither clear specular reflections. Subjects seemingly rely on highlighted areas that result not only from the specular reflections, but from internal scattering and caustics as well. It is difficult to tell which highlight is a specular reflection, which one is caustic, and which ones are produced by subsurface scattering - especially in low dynamic range scenarios. Naturally, high albedo objects with lower extinction coefficient produce more highlights. Refer to images C and D in Fig. 4.15. High albedo and limited dynamic range make it challenging to tell whether the highlights of image C were produced by specular reflections or subsurface scattering. The same task is a lot easier when the albedo is low (image D). The size of the highlights has been shown by Marlow et al. [85] to be positively correlated with perceived gloss. The curvature of the surface (as in the case of Lucy) can lead to large highlight areas due to high subsurface scattering. Interestingly, all smooth objects were considered equally shiny, while the differences between highlights start to prevail when the roughness is increased, producing a broader range of gloss perception.

These observations are consistent with Gigilashvili et al. [80]. They observed that the impact of translucency on gloss was different between spheres and complex female bust objects, qualitatively similar to Lucy. They interviewed the subjects and learned that the cues used for gloss estimation were different for different shapes, but they were also subject to individual interpretations. Further study is needed to investigate the reasons for the dramatic difference between sphere and Lucy results. Interestingly, the trends were similar between a sphere and a spiky sphere, as well as between Lucy and low-resolution Lucy. We believe this is correlated with the size of the objects. First of all, spheres

and spiky spheres cover larger field-of-view, having a more apparent reflection of the environment than a low-resolution Lucy, which has simple surface geometry itself, but still occupies too little space of the field of view to reflect clear images of the environment. Secondly, translucency varies with the thickness of the object [31, 42] and the path light travels inside the volume is indeed more similar between a sphere and a spiky sphere than between a thick sphere and thin Lucy. However, these speculations need concrete experimental evidence. On the other hand, a cylinder is the least affected shape by subsurface scattering. The reason for this could be the fact that its curved surface enables a clear reflection image for all smooth ones, while the rough ones resemble in highlight coverage cues - in the end yielding little difference among the cylinders with the same *alpha*.

It remains an open question exactly which image cues and which psycho-visual mechanisms of gloss perception are affected by the subsurface scattering, and rigorous future work is needed to answer it. Similarly to Marlow et al. [85], psychophysical studies should be conducted in the future to measure how perceived coverage, sharpness and contrast of the highlights (or other visual cues) co-vary with the perceived glossiness of the materials of different shapes and light transport properties. This will help us understand the differences observed in this chapter, and the robustness of the state-of-the-art will also be tested in the context of light-transmissive media. Moreover, particular image statistics should be studied to quantify and model the impact of subsurface scattering on the gloss cues in the image space. Additional interviews with the subjects could potentially help with the identification of the most salient cues and interpreting the results. Particularly, eye tracking experiments in the controlled conditions could provide deeper insight into the actual image cues used for glossiness assessment. And last but not least, we believe that perceived gloss is *at least* two dimensional - distinctness and contrast, as proposed by Pellacini et al. [5], being the major perceptual dimensions of gloss, even for translucent objects. However, the model quantifying these perceptual dimensions should include σ_t and albedo along with other physical parameters, to enable accurate placement of the translucent stimuli in the perceptual gloss space. We have observed in Experiment 1 that for high σ_t , when the light does not penetrate deep into the volume, the processes and findings are phenomenologically similar to Ward's model used by pellacini et al. [5]. Multidimensional scaling analysis (MDS) similar to [5] could reveal how σ_t and albedo contribute to distinctness and contrast, given that the stimuli are sampled densely enough in σ_t -albedo space. With that being said, we believe a separate embedding might be needed for each *alpha*, as the HVS might apply different

internal perceptual functions to the stimuli with different roughnesses (i.e. with different gloss cues).

Our findings have very practical implications for computer graphics, perception, as well as material appearance measurement and reproduction research. They demonstrate that when material appearance is modelled, it should be done on the shape we are particularly interested in and generalization of the findings based on one shape or surface roughness should be taken with extreme care. Besides, we propose that future work on gloss perception should include materials that permit subsurface light transport and the perceptual models of gloss should be updated so that they could account for potential contribution from subsurface scattering. Finally, gloss measurement setups and metrological protocols should accommodate materials with various degree of subsurface light transport.

4.6 Conclusion

We have conducted psychophysical experiments to test whether subsurface scattering contributes to gloss perception and to characterize this impact qualitatively and quantitatively. The results support our hypothesis and provide ample evidence that gloss perception is impacted by subsurface scattering. The impact varies across shapes and surface roughness levels; this we believe is the result of different low- and high-level image cues being used (by the HVS) for different shapes to assess gloss. Our findings propose that modelling appearance should be taken with care and findings should not be generalized to other shapes and surface scattering models. Moreover, the state-of-the-art findings based on fully opaque materials might not be valid for transparent and translucent media. Understanding *why* subsurface light transport contributes to apparent gloss and *how* it is used by the HVS would be an important future direction. Eventually, in order to scrutinize the contribution of subsurface light transport, a higher number of stimuli (ideally in HDR) will be needed to build a complete perceptual space of gloss. We believe the future work addressing gloss perception should not be limited to fully opaque materials and the perceptual models should account for subsurface scattering. Rigorous work is needed in the future to identify the exact mechanisms for predicting perceptual gloss from materials' surface and subsurface light transport properties. We also believe our study could raise more attention for material design applications that involve translucent materials.

Chapter 5

Material Design in Augmented Reality with In-Situ Visual Feedback

5.1 Introduction

Given the results of the user studies from previous chapters, we understand how humans visually perceive different materials, which helps us to define an intuitive perceptual parameter space. Our next step focus on how user could intuitively interact with materials during the design process. Materials in the physical world have unique appearance properties including color, glossiness and spatial texture. The same material may appear quite different under different illumination conditions. Material design is the process of specifying the properties of a virtual surface so that it will have the same appearance as a real world material in different environments. Many software packages (e.g. Maya, Blender) provide material design interfaces. In these interfaces users specify properties with visual feedback provided on a simple geometric form rendered with a simple background (often a checkerboard pattern). Systems have been proposed to provide feedback by rendering more complex geometries in more realistic environments. However, designing materials in a realistic environment has not been studied.

This chapter represents a first step towards quantitatively evaluating the effectiveness of a real environment for material design, by comparing it with material design in the virtual environment. We introduce Augmented Reality (AR) into the process of defining material properties. According to

[124], the definition of Augmented Reality is a system that (1) combines real and virtual objects in a real environment, (2) runs interactively, and in real time; and (3) registers (aligns) real and virtual objects with each other. Our AR-based setup allows material properties selected by the designer to be interactively superimposed on a real 3D object against a real background. The designed materials are rendered in the context that the users are exposed to, which helps users understand better how the materials behave under real lighting and shading conditions. The real-time interaction of AR makes sure that every modification made by users can be interactively viewed.

To test how AR contributes to material design, we build an AR material design prototype, where tracking is enabled to superimpose virtual materials on test objects and lighting conditions are estimated in real time to display material behaviors. To achieve real-time high resolution rendering, we use GPU-based ray-tracing with an irradiance caching algorithm for global illumination. We present a user study to compare the AR material design system with a 3D synthetic virtual material design system. We ask users to match materials to real world target objects on the two systems, and compare their results based on authenticity and similarity to the real materials. We want to compare the two systems to evaluate how the real environment influences users' behaviors during material design process, rather than which system is superior. To achieve our goal, we simplified the AR system to avoid bias caused by system settings.

The study consists of four parts. First, users conduct experiments matching materials. Second, users are asked to fill in a questionnaire after they finish the experiment in order to provide subjective feedback. Third, raters who are familiar with material design are asked to rate the designed materials based on the similarity to the real target materials (color, intensity, reflectance behaviors and so on). Finally, we use a light dome to measure the target materials used in the experiment and fit BRDF models to estimate the parameters, which are compared with parameters of designed materials from the two systems. We simplify the material design tasks so that users can focus on how the real and virtual scenes influence the materials. The same rendering system and user interface are used in both the systems to avoid bias.

From the objective and subjective evaluations, we observe the following:

1. Generally, users perform better on the AR material design system compared to the virtual synthetic material design system in terms of efficiency and quality of designed materials.

2. Users report superior experience with the AR material design system because of intuitive interaction style, the use of real lighting conditions and the sense of immersion created by having a realistic background.
3. Our study shows the presence of common preferences and usage patterns across users. For example, users prefer using the color spectrum tool over sliders, and they prefer adjusting parameters one at a time.
4. The geometry consistency (shape and orientation) between reference models and test objects influences the process of material design.

As with any other human experiments, our conclusions apply only within the context of our user study. However, we believe that the trend can be generalized and used for other related applications. We anticipate that our findings will lay out the foundation for lines of research that will further exploit the synergistic combination of AR and material design.

5.2 Related Work

5.2.1 User Study in Appearance Design

Kerr et al. conducted two user studies to evaluate different material design interfaces [1] and lighting design interfaces [125]. They built a prototype for evaluating and comparing different interfaces and systems involving user studies, where they defined the concept of *matching trial* and *open trial* based on whether an exemplar should be matched, or whether the user should create a new design. We choose the matching trial approach since we want to match the design materials to real world materials. Rather than giving the users image exemplars however, we provide physical exemplars to be matched.

5.2.2 Material Editing

Currently, many off-the-shelf software products provide material design features, such as Maya [2] and Blender[3]. Existing tools provide synthetic scenes to set a context within which users design materials. These synthetic background scenes include but are not limit to a grey or checkerboard

background, virtual lightings and cameras, and the use of virtual primitives on which the material is applied.

Many systems focus on editing material parameters and modifying BRDF models. Different prototypes can be divided into three categories: physical sliders, perceptual sliders and image navigation. Physical slider is a way to directly modify the parameters of BRDF models (e.g. diffuse, specular) to change materials. Maya uses this method for material design. Perceptual slider is another prototype where each parameter represents a perceptually-meaningful dimension of surface appearance such as luminance and contrast. Pellacini et al. [5] proposed a Ward BRDF model using perceptual parameterization. Westlund et al. [6] and Wills et al. [4] developed different measurements for perceptual parameterizations based on the material surfaces and BRDF models. Image navigation provides users with a group of materials with certain variations. Instead of modifying parameters, users can browse through the materials and pick the one that is closest to their goals. Other lines of work [65, 52] and software [66] further explored this idea and developed interfaces based on it. The experiment results from [1] show that users perform well on both physical sliders and perceptual sliders, but poorly on image navigation. Further, they found no significant difference on performance between physical sliders and perceptual sliders. Therefore, we implement our interface using the physical slider prototype.

Fleming et al. recorded in [67] that users can estimate surface reflectance properties reliably and accurately with the help of realistic illumination, which further stresses the importance of introducing real lighting into material design process. Following this idea, Colbert et al. [58] proposed an intuitive painting mechanism to create physically correct BRDFs with natural environment lighting. However, it is placed in an entirely virtual environment.

5.2.3 Material Display

Various systems have been developed to project virtual materials on real world objects. For example, Raskar et al.[126] projected rendered images onto a real object to artificially replace the material properties. Aliaga et al.[127] proposed a system using multiple projectors to superimpose high resolution appearance. Miyashita et al.[128] presented a material display system to overlay high resolution materials on a physical sphere in a zoetrope using compositing and animation principles. However, the generated materials are still rendered in an ideal synthetic scene (checkerboard in

their system) and users cannot move the objects to see how materials change with real lighting in different angles. All systems mentioned above work for static models and some of them are not view dependent, which makes it difficult for the user to physically interact with the targets (e.g. move and rotate) during material design process. Based on Raskar's system, Bandyopadhyay produced a movable 3D painting system[129] using projectors. To reproduce various materials, Hullin et al.[130] proposed methods using projection mapping techniques and specialized displays. However, objects and materials in these systems are illuminated by fixed virtual lights without adaptations to real environments.

5.2.4 High Resolution Rendering in Augmented Reality

The traditional techniques for high resolution rendering in AR is based on rasterization, and achieve a high rendering speed to support the interactivity of AR. There are many algorithms developed based on this technique. For example, Irradiance Environment Mapping was proposed in [131] in order to generate the illumination from real scenes onto virtual objects. Knecht et al.[132] and Grosch et al.[133] developed algorithms to simulate high-quality diffuse global illumination in AR. However, it is difficult to calculate specular effects such as reflection, refraction and caustics in high resolution using rasterization-based rendering.

Another rendering approach is to use ray-tracing, which can achieve high resolution rendering and accurate light transport calculations. There are many offline ray-tracing rendering algorithms which are used in mixed reality to render virtual objects and simulate global illumination [134][135]. Although high resolution and photorealism can be achieved by these algorithms, they cannot be used for interactive material design systems due to the low rendering speed. Kan et al. [136] implemented an AR system using GPU based ray-tracing and photon mapping, which provides realistic and physically correct rendering effects. We adopt their algorithm to implement the rendering pipeline of both material design systems, since it can accurately simulate different material reflection behaviors under real lighting conditions.

5.2.5 Global Illumination in Mixed Reality

It is important to use global illumination in material design systems since lighting plays a significant role in the simulation of realistic materials. A solution to fast global illumination calculation in mixed reality with automatic 3D scene reconstruction was proposed in [137], where the Reflective Shadow Maps [138] algorithm is used for the indirect illumination calculation. However, they only support diffuse illumination. Many other algorithms [139][133] use preprocessing to calculate the indirect illumination for possible directions and store the irradiance in Spherical Harmonics. Then the irradiance can be dynamically applied in real time according to the directions of incident direct light. However, these methods are limited since they cannot deal with non-static objects and the preprocessing takes time due to the large irradiance volume.

Irradiance caching (IC) proposed by Ward [140] is a widely used algorithm for global illumination. It takes advantage of spatial coherence to accurately interpolate irradiance records in sparse location. Many algorithms have been developed based on this idea, such as IC with Neighbor Clamping [141], where the average distance to the nearby geometry is clamped based on the distance to the neighboring cache records, and IC with improved error metrics [142][143], which improves the cache record placements. Kan et al.[144] developed a system using the irradiance caching algorithm to simulate the light transport between virtual objects and real world in mixed reality. They use rasterization to interpolate the indirect illumination between cache records and calculates the direct light using ray-tracing, which achieves real-time rendering. Their work can efficiently simulate physically correct reflection and refraction behaviors under various lighting conditions and we use their algorithms to achieve global illumination.

5.3 Study Overview

5.3.1 Goal

We try to evaluate how providing visual feedback by rendering in an environment familiar to the user influences the performance of 3D material design. To be more specific, we compare the traditional material design in synthetic 3D virtual scenes with a new Augmented Reality material design prototype, in order to test whether users can perform better in designing material appearances

with the help of Augmented Reality, and in what aspects Augmented Reality can contribute to their improvements. We mainly focus on the comparison of interaction, lighting and the authenticity of designed materials.

5.3.2 Users

In order to draw generalized conclusions, we recruited participants who are familiar with computer graphics and material design, as well as novice users. According to [1], novice users are capable of designing and editing complex realistic materials. Furthermore, we want to see if different knowledge levels in material design will lead to different results. We asked all the subjects to rate their level of knowledge regarding material design from 1 to 5 before the experiment (1 represents extremely unfamiliar and 5 extremely familiar). Subjects who rated themselves 1 or 2 in a certain field were considered as novice users and viewed a small lecture to equip them with necessary knowledge.

5.3.3 Task

Since long experiments may cause fatigue, we try to balance between length and complexity of the experiment. On the one hand, we want to complete an adequate number of trials and complex-enough materials for editing to get meaningful results. On the other hand, we try to avoid bias and fatigue caused by a long experiment. Therefore, we designed eight independent trials, half on the AR material design system and half on the synthetic material design system. The total experiment length is set as one hour per person which promises good measurements and results while keeping a low level of fatigue. In each trial, subjects are asked to match as close as possible a material to the surface of a real world model. The material is designed on the same geometry as the real world model. We use the same models on both systems for ease of comparison.

5.3.4 Materials

Materials Considering that material design is time-consuming, we simplified the task by providing only a few parameters to edit, so that subjects can focus on the different material behaviors between real and synthetic scenes. The parameters include specular, diffuse albedo, ambient, transparency and shininess. Taking into account that not all subjects are experienced users in material design,

we decided to only provide one BRDF model for the experiment and we chose Phong model for simplicity.

5.3.5 Models and Geometries

Four different real models and geometries are chosen as targets in our study, including cubes, cylinders and complex geometries. Tasks are arranged in increasing order of geometry and material complexity. Matching materials to a standard cube with a diffuse surface serves as the warm-up for the subjects, while working on complex geometries with a dark copper material is most challenging since irregular surfaces and their unpredictable behaviors. Subjects were given the real target models and asked to design materials on the exact same geometries on the computer. For all the cubes and cylinders, no textures applied. Complex geometry comes with an initial texture. The real target models are either pre-existing objects or 3D printed with painted materials.

5.3.6 Interaction

While Augmented Reality can be presented in various display systems, we stick to computer screens as the display media for both the AR material design system and the synthetic material design system, since we believe that the difference of display devices between AR and synthetic systems might introduce noise and bias in the results. For the AR material design system, models with tracking markers (Figure 5.2) are superimposed by the designed materials and rendered in the real scene. Subjects can physically interact with the models with overlaid materials using their hands. For the virtual synthetic material design system, the designed materials are placed in a synthetic scene with a checkerboard background. Subjects work on the 2D screen and interact with the object via their mouse.

5.3.7 Lighting

Lighting In the AR material design system, real world light estimate is used for simulating of global illumination so that the material behaviors under a real environment can be generated. Users can adjust both the light (position and orientation) and the objects to see how materials react to the environment. For the synthetic material design system, we follow the widely used setup, where the

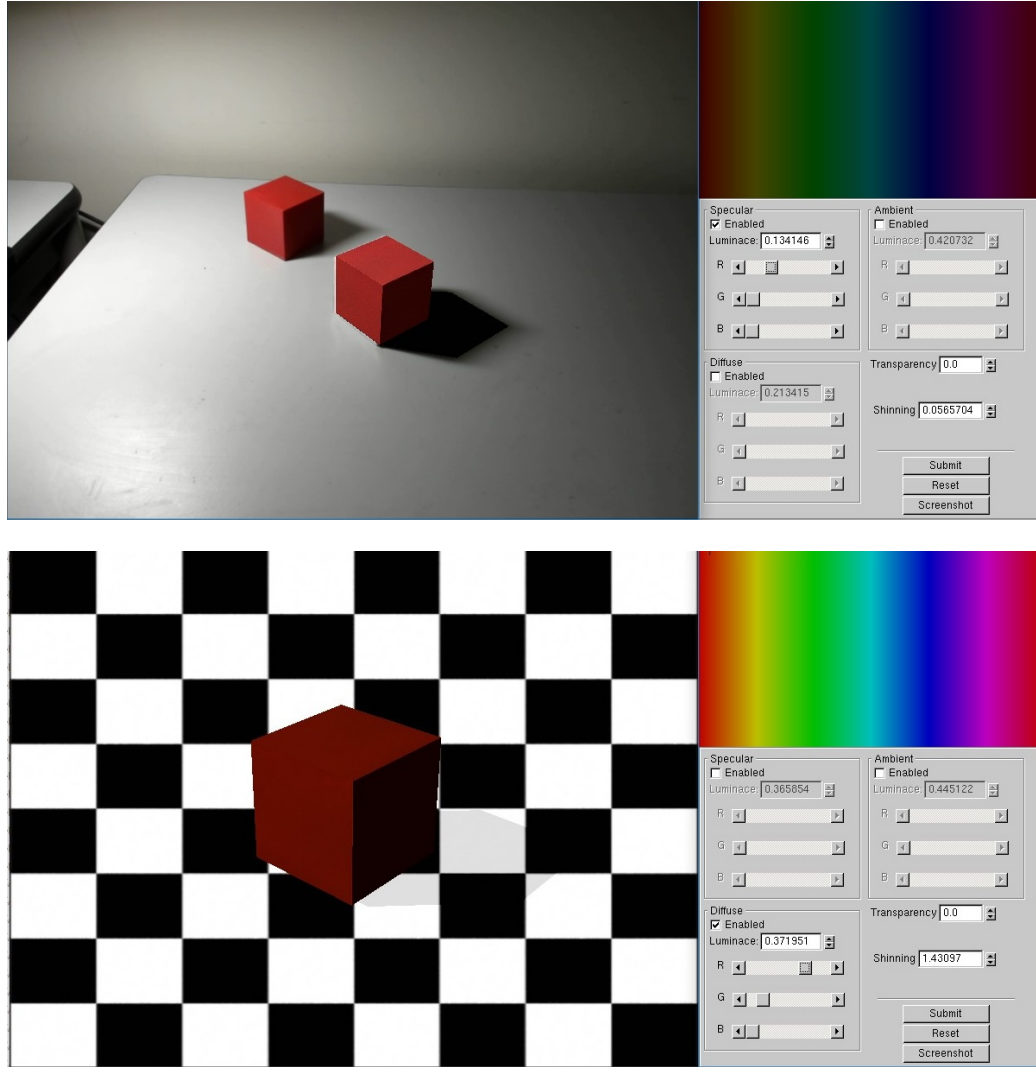


Figure 5.1: Augmented Reality material design user interface and Virtual Synthetic material design user interface.

lighting is fixed relative to the object.

5.3.8 User Interface

Both systems use the same interface for material design (Figure 5.1). For parameters such as specularity, diffuse albedo and ambient, subjects can edit RGB channels by dragging corresponding sliders. They can also use the spectrum with a luminance slider to directly pick colors. The luminance changes with the RGB value. They can also modify the transparency and shininess by changing the slider. A screenshot button helps subjects to make a screenshot for current material and a reset button give subjects a chance to start over. After finishing the material design, subjects can use a submit

button to automatically generate a report recording the material properties they just designed.

5.4 Experiment

We ask subjects to complete eight independent trials, during which their performances and actions are recorded. The trials vary in the geometry of models, target materials and presence of textures.

5.4.1 Trials

We conducted pilot experiments on 5 additional subjects, the results of which are not presented in this chapter. We also revisited the trials based on the feedback from pilot experiments.

Subjects were asked to finish all four trials on one system and then switch to the other one. The order of the systems was balanced. We used different real world materials as targets for each trial. We diversified the target materials by choosing materials with different properties and select different geometries. For Trial 1, a fully saturated glossy plastic red cube was used as the target. For Trial 2, the goal was to match a half saturated green glass cube. For Trial 3, the target was a brown cylinder with half diffuse and half specular surface. For the last trial, a complex geometric form (a cartoon character) with copper paint served as the target. For Trial 1 to 3, a glossy diffuse grey cube/cylinder was provided to subjects as the initial state. For Trial 4, a virtual object with the same geometry and texture was given to subjects at the beginning of the trial. Each trial had a fixed time limit, which was set based on the pilot experiments. Subjects could end the trial earlier if they were satisfied with their results.

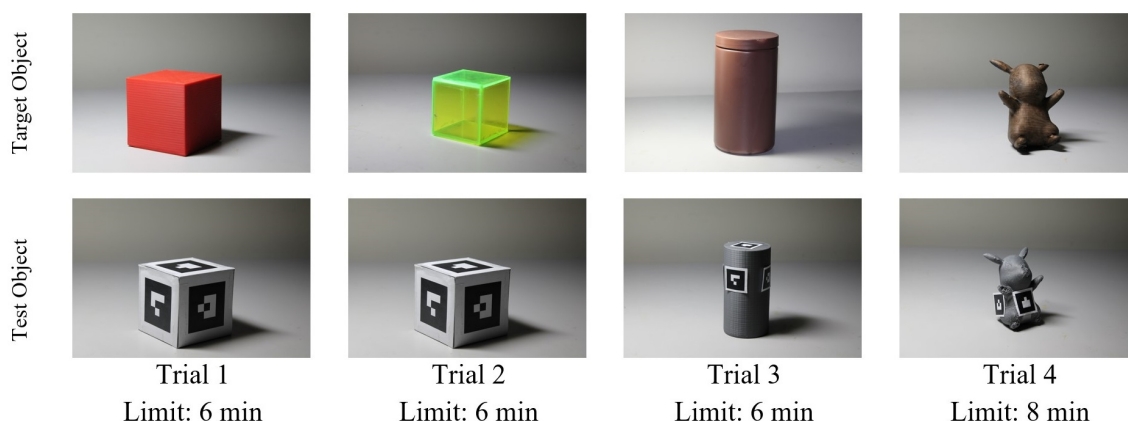


Figure 5.2: Reference materials, test objects for AR tracking and time limits for all trials.

5.4.2 Procedure

Procedure Sixteen subjects from different age groups and education background participated in our study. Half considered themselves as novice users. All subjects had normal or corrected-to-normal vision and did not suffer from color blindness. Before the experiment, novice subjects were given a small lecture (around 15 minutes) about material design and Augmented Reality. Before they started the experiment on each system, all subjects were given a training session to help them get familiar with the user interface and basic operations. Only when the experimenter verified that subjects were familiar and comfortable enough with material design and system operation could they start the experiment. Each subject spent around one hour to finish all the trials. To avoid bias, subjects were asked to start with one of the two systems randomly. After finishing all the trials on that system, they switched to the other system.

As part of the experiments, we conducted three different kinds of evaluation: questionnaire, human rating and BRDF parameter evaluation. The first two provide subjective feedback, while the last one gives us objective comparison.

5.4.3 Questionnaire

Questionnaire After finishing all the trials, subjects completed a questionnaire immediately, where they rated how satisfied they were with their result for each trial on a scale of 1 to 5 (1 represents worst and 5 represents best). Subjects were also asked to rate both the systems in the following categories: (1) lighting setup, (2) interaction style, (3) overall performance and (4) personal preference. Subjects could also leave feedback for each system.

5.4.4 Rating

Rating We introduced 10 raters from those who were familiar with material design into our experiment during the evaluation process. Their goal was to compare the authenticity of materials designed by subjects from both systems. Raters voted for the designed materials that had better performance (more similar to the target material and fit better in the environment) and select reasons (multiple selections) from provided options (color, intensity under lighting, diffuse and specular behavior) for each vote. Raters did not participate in the matching trial to prevent bias. Since our goal is to

improve the authenticity of the materials in real environment, we used the AR system for rating. During the rating process, all the designed materials were imported into a new real environment (scene), which was different from the scene used for experiment. We used a new environment so that the raters would be evaluating the similarity of the materials, rather than the similarity of a particular view or image. Raters were blinded to the order of subjects' results and the information on which system produced the result.

5.4.5 BRDF Parameters Evaluation

BRDF Parameters Evaluation To fully evaluate the authenticity of designed materials from both systems, we first estimate the BRDF parameters of our real target materials, and then compare them with the subject-specified BRDF parameters from the matching trials using mean squared errors. We focus on the estimation of diffuse and specular since those parameters play important roles in material appearances.

To estimate the BRDF parameters, we use a dome with 45 light sources. With 3D coordinates recorded, these light sources are located on four different layers towards the center of the bottom circle where test materials are put. The first two layers have 15 light sources each, the third layer has 10 light sources, and the highest layer has 5 light sources. There is a camera right at the apex of the dome to capture raw responses. We use an achromatic striped spectralon that has the pure diffuse reflectance of 0.12, 0.25, 0.50, and 0.99 to calibrate the system. Coefficients are calculated to represent how the response corresponds to the diffuse albedo and to compensate for the light color. After recording 45 images for these four materials, we compute the average color of the object region as a BRDF measurement, and then fit the Phong model to estimate the parameters of diffuse ρ_d , specular ρ_s . To avoid overfitting, we interactively try different shininess n and set an upper bound to minimize the fitting error.

Similar to the method in [7], we consider each average color as a BRDF sample of the material and we can plot 45 sampling points of response with respect to the incident angle θ for RGB channels of each material. We assume that the specular component is not significant for light sources on the first two layers, so we fit a pure diffuse model to estimate ρ_d . With ρ_d fixed, we use the rest data to fit the whole Phong model with the parameters of ρ_s . Fitting the BRDF model can be considered as

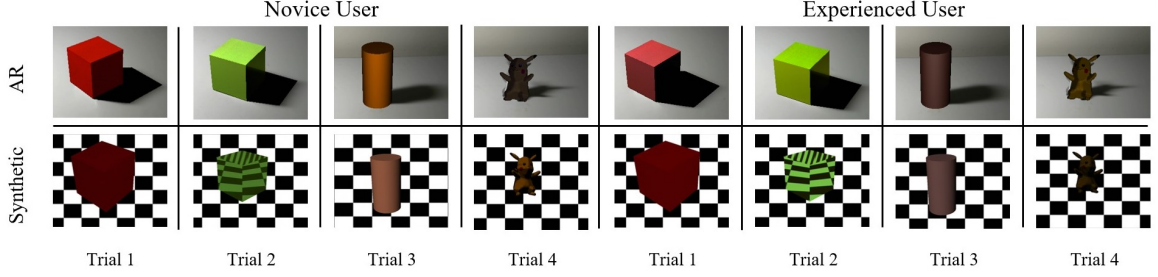


Figure 5.3: Example of designed materials of two subjects using different systems.

an optimization problem, and we use linear least squares in this process.

$$\rho_d = \underset{\substack{0 < \rho'_d < 1 \\ i \text{ on layer 1 and layer 2}}}{\operatorname{argmin}} [S(\theta_i, \phi_i) - M_{\rho'_d, 0, 0}(\theta_i, \phi_i)]^2$$

$$\rho_s, n = \underset{\substack{0 < \rho'_s < 1, 0 < n' < 5 \\ i \text{ on layer 3 and layer 4}}}{\operatorname{argmin}} [S(\theta_i, \phi_i) - M_{\rho'_s, n'}(\theta_i, \phi_i)]^2$$

Where $S(\theta_i, \phi_i)$ is the BRDF sample values and $M(\theta_i, \phi_i)$ represents the Phong model we want to fit, where its subscripts are the parameters used in the Phong model. We fix the shininess at a time so that we can separate the linear components, which improves the efficiency and stability of the optimization, and we iterate the shininess to converge to the global minimum.

5.5 System Implementation

In this section, we describe the implementation of the AR material design system. Figure 5.4 shows system setup.

5.5.1 System Structure

System Structure Our system includes two high resolution cameras for input, a PC for processing and a monitor for display. One of the cameras is used for real-time video input and the other one is used to capture the environment image for environment mapping and real world light source estimation. For each frame, the images from both cameras are converted to HDR by using inverse tone mapping. Image of the real scene captured by the first camera is used for marker detection to provide the location for virtual object registration and relative camera position. The environment



Figure 5.4: Augmented Reality system setup.

image captured by the second camera is used for environment mapping and the estimated light source information is used to set up the virtual lighting. Then, all the calculation and estimation results are passed to a GPU ray-tracing pipeline for rendering, the result of which is composited with real scene images and delivered to an output device. The processing of video input (including rendering and composition) and light source estimation run on two different threads to make sure the calculation is fast enough for real-time interaction.

5.5.2 Rendering

Rendering To generate more realistic material appearances, we use global illumination in both the AR material design system and the synthetic material design system. We follow the methods in the paper[144] to use the differential irradiance caching algorithm in combination with ray-tracing to enable multiple bounces of global illumination. Monte Carlo integration in GPU ray-tracing is used to evaluate differential irradiance at irradiance cache records in one pass. Diffuse light transport between virtual and real worlds can be efficiently calculated in our system to produce a high-quality result while preserving interactivity. The NVIDIA OptiX ray-tracing engine [145] is used to take

full advantage of parallel power of GPUs. We use GPU ray-tracing where differential irradiance is evaluated at the locations of cache records. We calculate direct illumination and specular indirect illumination by ray-tracing.

5.5.3 Light Estimation

Light Estimation We use a camera to capture the environment and estimate the light source to simulate the material behavior under real lighting conditions. Following the method mentioned in [136], we use the image-based lighting technique to estimate the real light in the environment for AR system. After acquiring the basic lighting information, we apply adjustments to the estimated light source based on the difference of position and orientation of the real object (markers) between frames. The adjustment ensures that the relative position and orientation between virtual light and virtual object remain the same with the real situation, especially when a subject physically interacts with the real object. To reduce computational cost, we do not directly perform the transformation of real object on the virtual object. The whole system is set up in a controlled lighting environment for accurate light estimation.

5.5.4 Tracking

Tracking For Augmented Reality, tracking is important since it provides location and orientation for 3D virtual object registration. In our AR material design system, we use the multi-marker tracking technique provided by ARToolKit[146]. We use multi-marker tracking instead of single-marker tracking because we want the designed materials to entirely overlay and move smoothly with the real object. A single marker can easily be occluded when subjects try to physically interact with the real object. Using multi-markers, at least one marker can be detected, even if some markers are hidden. We carefully designed and measured the location and orientation of multi-markers before the experiment to ensure accurate tracking and material overlay.

The synthetic material design system uses the same rendering pipeline. Since the whole scene is virtually generated with the checkerboard background, there is no need for video input, real light estimation and tracking.

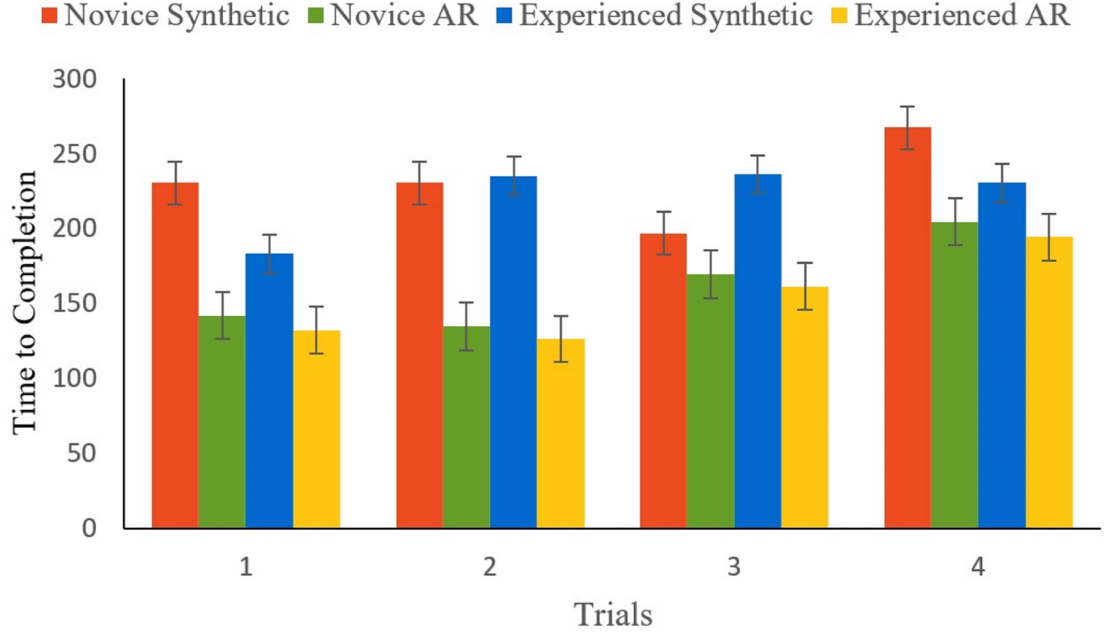


Figure 5.5: Average time to completion for all trials over novice and experienced users (in seconds).

5.5.5 Hardware Description

Hardware Description We use a 24-inch HP Compaq LA2405wg screen with 1920×1080 resolution for display. The systems ran on a computer with Intel Core i7 3.30GHZ CPU, 16 GB RAM and NVidia GeForce GTX1080 GPU. The two cameras used for video input and environment map are Logitech BRIO 4K pro and Logitech HD C615 respectively.

5.6 Results

As mentioned in Section 4, we present an analysis for the data collected from our experiment in three different steps. First, we evaluated the data and feedback from subjects and questionnaires. Second, we collected results from raters and analyzed the reasons they selected for each vote. Last, we compared the subject-defined material parameters with our estimated BRDF parameters of real target materials. We use repeated measures analysis of variance (ANOVA) [147] to compute statistical significance. This method is appropriate to calculate correlations with within-subject factors (in our experiment, each subject using two systems) and violates the assumption of independence in standard one-way ANOVA. A p value represents the confidence of difference between two sample

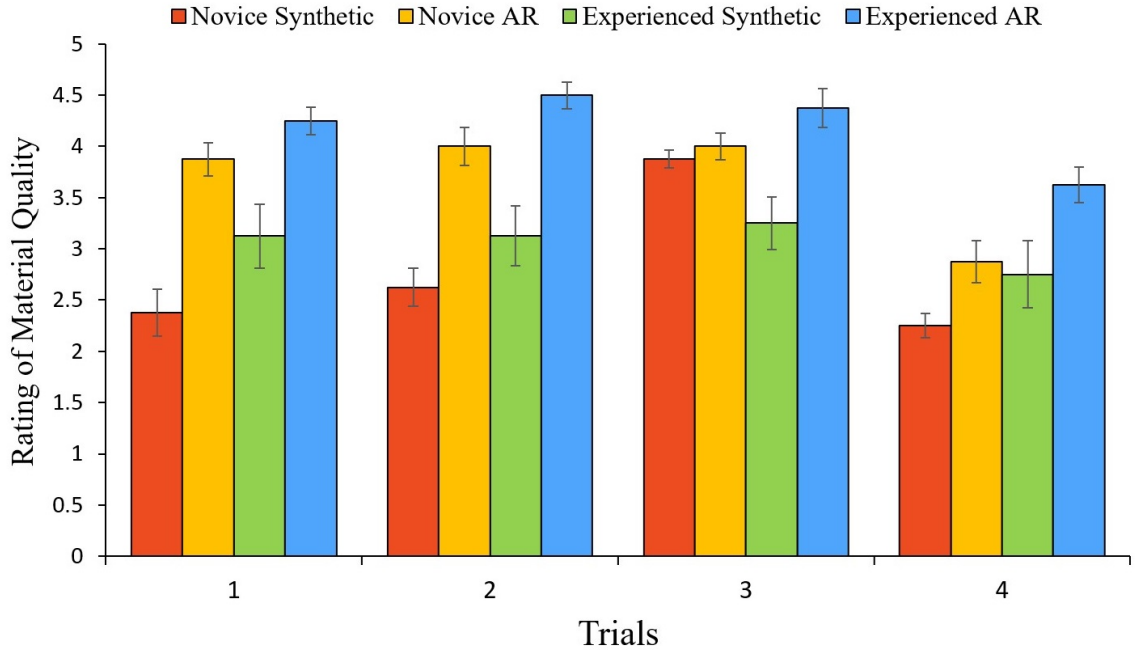


Figure 5.6: Average material quality rating over novice and experienced users.

groups. A p value below 0.05 indicate 95% confidence of difference.

5.6.1 Time to Completion

We recorded the time that each subject used for each trial. Subjects were usually able to finish each trial within the time limits. Figure 5.5 shows the average time to completion for each trial over novice and experienced users. Time to completion on synthetic system is significantly higher than AR system for all trials ($p < 0.030$) for all users. Not unexpectedly, novice users spent more time on both systems compared to experienced users (except trial 3 on synthetic system) due to the lack of familiarity with the task.

5.6.2 Satisfaction for Material Quality

Subjects were asked to rate their own results for each trial after the experiment on a scale from 1 to 5, with 1 being the worst and 5 being the best. Results were rated in terms of the closeness the designed materials and real target materials. Screenshots were provided so that subjects could compare their results with the real target materials. Figure 5.6 shows the average rating results for each trial.

Subjects rated their work on the AR system significantly higher than their work on the synthetic

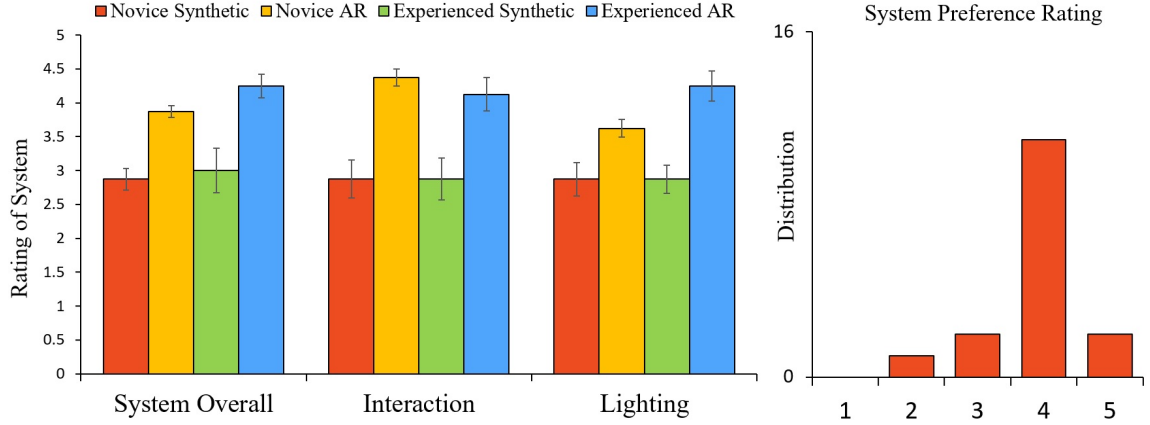


Figure 5.7: Average system rating over novice and experienced users and distribution of preference rating.

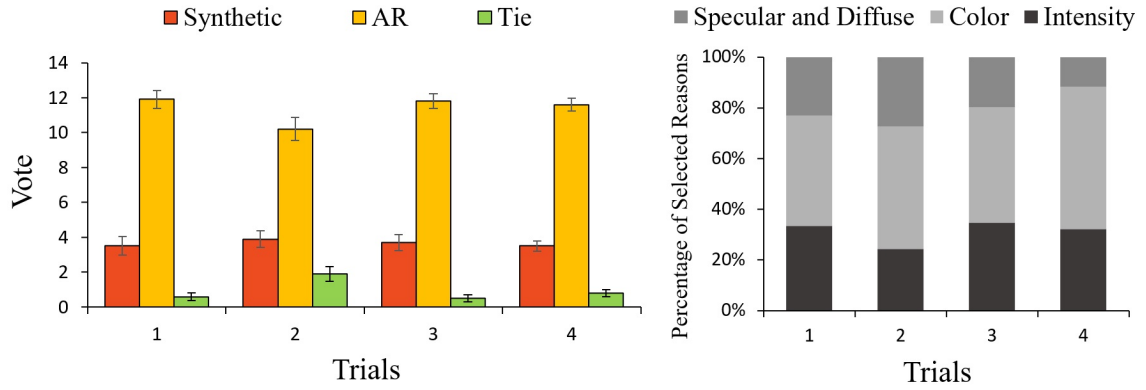


Figure 5.8: Average number of votes for each system and percentage of selected reasons of votes for AR systems.

system ($p < 0.045$). We believe the behaviors of novice users on Trial 3 differs because it was difficult for novice users to duplicate the same size of specular highlight on the real target object. According to our observations, for trial 3, novice users gave up trying earlier on both systems due to the impatience caused by failed attempts, which lead to less time spent on this trial compared with experienced users and more similar self-ratings between two systems. The average rating of experienced users is relatively higher than that of the novice users on both systems ($p < 0.011$), which can be explained by the fact that experienced users were more familiar with material design tasks and could create results that met their expectations. Compared with other trials, ratings for trial 4 were relatively lower, indicating that all users were unsatisfied with their results for complex geometries.

Object	ρ_{d_R}	ρ_{d_G}	ρ_{d_B}	ρ_{s_R}	ρ_{s_G}	ρ_{s_B}
Red Cube	0.8669	0.0874	0.0788	0	0.0405	0.0469
Cylinder	0.2509	0.128	0.0789	0.173	0.1815	0.2015
Complex Geometry	0.2346	0.1389	0.079	0.1784	0.1245	0.0775

Table 5.1: Estimated BRDF parameter values for all target objects in experiment.

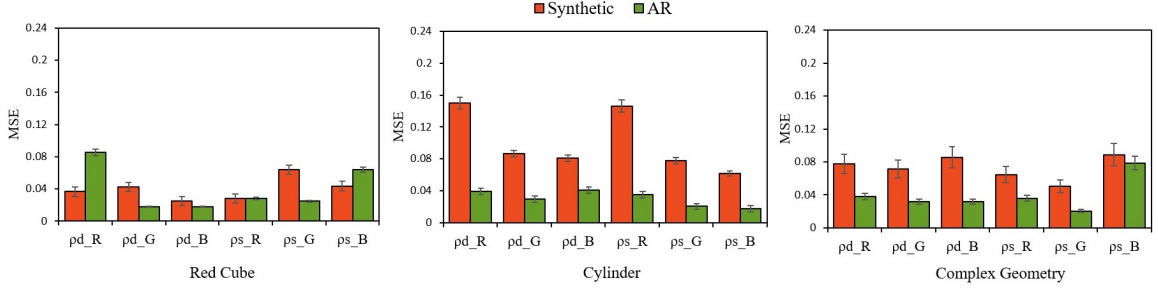


Figure 5.9: Mean square errors between user defined material BRDF parameters and estimated BRDF parameters over two systems.

5.6.3 Subjective System Ranking and Rating

Subjective System Ranking and Rating Subjects rated each system in three different categories based on their preferences (lighting, interaction style, system overall) on a scale from 1 to 5, with 1 being the worst and 5 being the best. They were also asked to rate their preferences over two systems, with 1 preferring synthetic system most and 5 preferring AR system most. Average ratings are shown in Figure 5.7. In all categories, the AR system outranks the synthetic system ($p < 0.001$) for both novice and experienced users. No statistical difference was observed between ratings of novice and experienced users ($p > 0.181$). The majority of subjects preferred the AR system over synthetic system.

5.6.4 Raters' Evaluation

Raters were asked to go through all subjects' results for each trial, and were asked to compare the two materials from the two systems respectively, which were designed by the same subject, and gave votes based on the authenticity of materials and similarity to real targets (see Figure 5.8). We can see that the number of votes for the AR system is significantly higher than that of the synthetic system ($p < 0.001$). No statistical difference was observed between trials ($p > 0.801$). To further explore why raters prefer results from AR system, we analyzed the reasons tied to each rating for AR (details in

Section 4). Intensity and color are the main reasons ($p < 0.041$) that raters preferred the AR system over the synthetic system, and there is no significant difference between the ratings for intensity and color. We can make two conclusions based on the data. Our results agree with made in [1] that color is a very important factor in overall material appearance. We also conclude that with the help of real scenes in AR, users can perform better in color and intensity adjustment for material design.

5.6.5 BRDF Parameter Comparison

Table 5.1 shows the estimated BRDF values of the target materials we used in our experiment, except for Trial 2, which involves with transparent material which cannot be accurately measured using the light dome, we focus on the BRDF parameter comparison for other trials. To qualitatively compare the overall performance of each system, we analyze the mean square error between user defined material BRDF parameter values and estimated BRDF parameter values. The lower mean square error (MSE) indicates that user designed materials are closer to the real target material on average. Figure 5.9 shows that the MSE values over all parameters of the AR system are relatively lower than that of the synthetic system, except some parameters for the red cube. This could be partly due to the high saturation of the material, which is not close to natural materials and influences users judgement of color. In addition, the dark side of the red cube with attached shadow could have given subjects an impression of a darker material appearance in the AR system against the real scene with controlled lighting.

5.7 Workflow Observation

In this section, we discuss behaviors of subjects during the experiment. Unless stated otherwise, our observations apply to both novice users and experienced users.

5.7.1 Lighting Adjustment

For the AR material design system, the majority of subjects made small lighting adjustments, including lighting intensity and orientation, in simple geometry trials (cubes and cylinders) before they started to edit the materials, even if everything in the scene was pre-calibrated. Based on their own judgements, they adjusted the lighting and shading of test objects to match real target models.

However, for the trial using complex geometry models, only a few subjects adjusted the settings at the beginning. This leads us to believe that users do care about the lighting and shading of the materials and how materials react to the real environment. Given more freedom of control, they would like to explore different lighting possibilities based on their own preferences and judgements, which might be beyond their capabilities since lighting design is another complex task. It also suggests that different people have different perceptions and sensitivities on how lighting changes materials. The sensitivity to lighting decreases when the geometry complexity increases. In other words, people may not be able to perceive how lighting changes materials when complex models are used for material design. It is worth mentioning that after subjects finished the lighting adjustment at the beginning, they were inclined to keep the light source fixed without modifying it for the rest of the trial.

5.7.2 Geometry Consistency

Based on our observations, many subjects rotated and moved the test objects to match the orientation of real target objects at the beginning of each trial for both systems, which suggests that users do care about the geometry consistency (shape and orientation) of models used for material design. To further test our observation, we conducted a sub-experiment. Instead of real target objects, we used images as references. The object orientations in the images were different from the initial orientations of the test objects. We asked five subjects to design materials on both systems using the images. In this situation, all subjects started trials by modifying the orientations of the test object based on the given images. Based on these results, we believe that geometry consistency does influence the material design process, and for 3D material design, it would be better to keep the test objects and references in the exactly same shape and orientation.

5.7.3 Object Interaction

Subjects were more likely to interact with the objects superimposed with applied materials in the AR system than the virtual objects in the synthetic system. For the AR system, subjects often rotated the objects to see materials on different sides during the matching trials, while for the synthetic system, most of the subjects stick to the positions and orientations of the virtual objects after the adjustments at the beginning. These observations also agree with the rating on interaction from the

questionnaires.

5.7.4 Real Scenes vs. Synthetic Scenes

We noticed that users prefer real scenes in the AR system to the virtual checkerboard background in the synthetic system. When asked "which background do you prefer most, real scene or checkerboard?", 14 out of 16 subjects chose real scene. Subjects commented, "I felt like it was very realistic when working in a real scene, while the checkerboard gave a sense of fake and weird", and "It (the real scene) is better to judge the reflection, especially for the transparent one (Trial 2)". These are some typical comments that many subjects mentioned or expressed in similar ways. Their preferences also agree with their ratings and performances mentioned in Section 6. However, a minority of subjects mentioned that the rendered materials were a little bit too perfect compared to the real scene. We believe that the contrast is caused by the difference of noise in captured video input. Adding noise and distortion into rendered materials can be considered as future work to register the virtual materials better into real scenes.

5.7.5 One-Parameter-at-a-Time

The most noticeable trend of material editing is that subjects prefer to focus on one parameter instead of modifying multiple parameters simultaneously. To be more specific, given RGB three dimensions (luminance is calculated based on these dimensions) for parameters such as specular, diffuse and ambient, subjects were more likely to work on one parameter until they were content with the appearances. However, it does not mean that subjects would fix the parameter values permanently after they modified them. Based on our observations, subjects revisit some parameters to further polish their work after the whole appearance was roughly settled .

5.7.6 Spectrum vs. Sliders

We noticed that subjects spent more time picking colors directly from spectrum instead of dragging sliders in both systems. This applies to the majority of novice users and some experienced users. This fact suggests that subjects, especially novice users, may not be able to precisely anticipate color when dragging a slider in RGB color space. On the contrary, spectrum can provide a more intuitive

display of color and is preferred among subjects. However, we also notice that even if working on spectrum, subjects were not able to pick their preferred color in their first few attempts. They were inclined to narrow down to a small range in the spectrum, and blindly try different colors until they were satisfied or gave up. Based on these observations, we believe that adding more features on spectrum, such as range selection and zoom-in to provide more accurate interpolation and detailed color display, may help users for color selection.

5.8 Discussion

In this section, we draw conclusions for our experiment based on evaluations and observations. We want to remind our readers that our conclusions are drawn from a limited number of test cases and only apply to experiments we conducted. Also, we stress that the main goal of our project is not to prove that one system is better than the other. Instead, we want to explore how a real environment influences material design and user behavior.

Comparison of Material Design Systems Overall, we found that users perform better on the Augmented Reality material design system in terms of efficiency and quality of designed materials, regardless of their experience level. They also have better user experience on the AR system than the traditional synthetic system, which makes them prefer the AR system.

Interaction Based on users' feedback, users are more willing to interact with real objects in the AR system than manipulating virtual objects in the synthetic system. It is easier and more intuitive for users to perform physical interaction and observe material behaviors, which makes them feel confident in material design process.

Lighting Lighting setups influence users behaviors in material design. Users prefer the adjustable lighting setup in the AR system compared to the fixed lighting in the synthetic system. Given more freedom of control for lighting, users can try different lighting conditions in order to observe how materials adapt to the environment.

Background Scenes We find users prefer real scenes as background during material design instead of virtual scenes. The real scenes give users a realistic and immersive feeling, and can be used to generate authentic reflection, especially for mirror and glass materials.

Influence of Geometry Consistency Geometric properties, such as shape and orientation of

the models used for material design, influence how users perceive materials. Users are inclined to adjust and match the geometry properties of test objects based on the target models. With the same shape and orientation, users can directly observe the behaviors of target materials and use them as references, which helps them match material appearances.

Common Workflow There are common patterns in editing material parameters among our subjects. We notice that most subjects are inclined to use color spectrum rather than RGB sliders to define a color. Our subjects also prefer to edit one parameter at a time, especially when the parameter has multiple editable dimensions. Revisiting modified parameters happens when results are close to targets and small modifications are needed.

Limitation and Future Work There are some limitations to our work. First, considering the potential fatigue of tedious parameter adjustments, we only provided a limited number of parameters and BRDF models for users to edit. Secondly, target materials used for references in our experiment are relatively simple, because we use real life materials instead of synthetic material sample images, which are often used in virtual environment material design tasks. Since our goal is to evaluate the influence of real environment on material design, real objects serve our purpose better. Moreover, we use the same display format for both systems to present the designed materials to avoid bias. However, we believe there are many better display formats for AR, such as multiple projection and head mounted devices, which can be considered as future work to further improve user experience.

5.9 Conclusion

This chapter presents a first step towards quantitatively evaluating the performance of material design in real environment. To compare with the traditional 3D virtual synthetic material design system, we created an Augmented Reality material design prototype, where users can observe their designed materials against real environment with physically correct material behaviors under real lighting conditions. They can also interact with the test object superimposed by the virtual materials in real life, which enhances user experience during the design process. To further evaluate the influence of real environment on material design, we conducted a user study where we asked subjects to design materials based on real world materials on both AR and virtual synthetic systems. The evaluation for the user study includes three parts: (1) subjects' feedback collected from questionnaires, (2) human

rating for subjects' results based on authenticity and similarity to target materials and (3) comparison between estimated BRDF parameters and subject-defined material parameters.

Our results show that compared to the traditional virtual synthetic material design system, Augmented Reality material design has better performance in terms of efficiency, authenticity of designed materials and user experience. The advantage of AR material design system is that it can provide more intuitive interactions and display different material behaviors influenced by estimated real lighting conditions. We also evaluated workflow patterns based on our subjects' behaviors, such as the preference of spectrum over sliders and editing one parameter at a time.

We acknowledge that we have studied only a small subset of factors and models that influence material design, and we believe Augment Reality material design systems can be further improved in the future. Expanding material models and parameters and introducing more immersive display formats would be of interest.

Chapter 6

Learning-Based Inverse Bi-Scale Material Fitting from Tabular BRDFs

6.1 Introduction

In previous chapters we considered the design of materials that appear the same at all scales. In this chapter we consider designing materials that look qualitatively different when viewed closely and when viewed at a distance. This is the bi-scale material design problem. It is particularly important when objects are to be physically fabricated.

Given a target appearance created by the users, fabricating the physical material is the final step of the design pipeline. However, bringing virtually designed materials into the real world is a challenging problem. Physical properties including structures and reflectance behaviors determine the appearance of a material. For manufacturing industries, small-scale geometric patterns are introduced for molding textures¹ in order to enhance material performance and increase the gamut of appearance. However, achieving a particular large-scale target appearance is challenging given the diverse choices for meso-scale geometry and micro-scale material reflectance. Without an automatic solution, the traditional design process relies on tweaking parameters to match a specific appearance, which can be a tedious (and computationally expensive) process of trial and error.

Our goal is to solve this problem by providing an automatic solution to fit a target large-scale

1. <http://www.stpaulengraving.com/texturing-plastic-injection-mold.html>

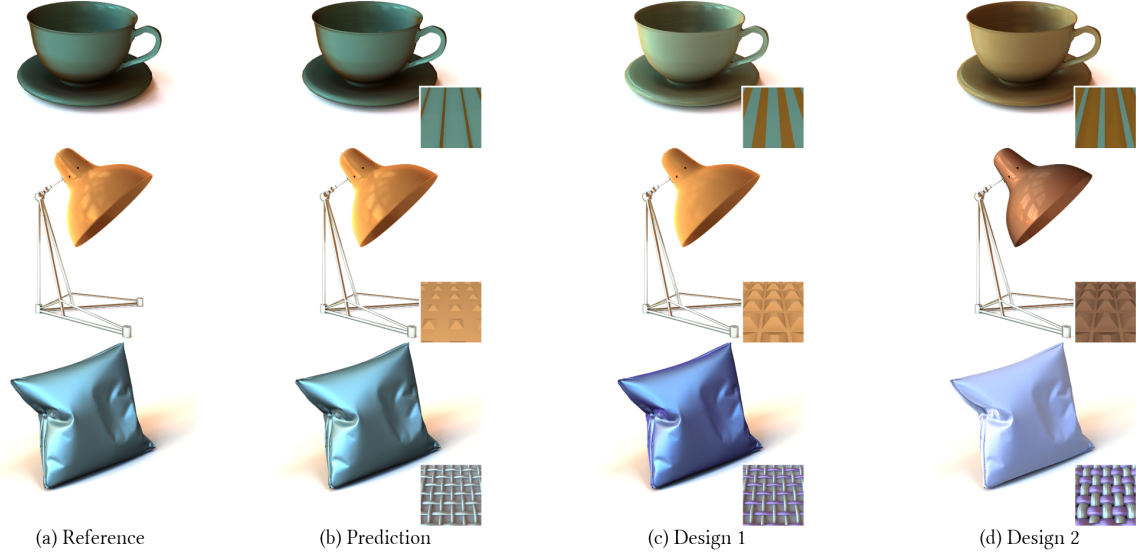


Figure 6.1: Bi-scale material fitting framework with given the large-scale appearance, reconstruction, and new designs

macro-BRDF with a meso-scale geometry and a micro-scale BRDF. We use the term “large-scale appearance” to refer to the material appearance when viewed from a relatively far away distance (typically measured by meters), which can be modeled by a macro-BRDF. When we zoom in, we can take a close up view of the “small-scale details,” which are made up of the meso-scale geometric structures (typically measured by millimeters). We use the micro-scale BRDF to define the basic reflectance of each facet at this level. The difference in the macro-BRDF and the micro-BRDF is caused by the shadowing and masking effects created by the meso-scale geometries. Figure 6.2 shows an example of a physical material at two different scales. We will refer to the combination of the meso-scale geometry and the micro-scale BRDF as the “small-scale details.” We do not seek a unique solution for the small-scale details but the reconstructed large-scale appearance should be identical (or very close) to the target. At first glance, this is similar to previous BRDF fitting problems [7, 8, 9, 10, 11, 12, 13], where a single analytical model is fit to BRDF data and only a few parameters need to be optimized. However, fitting bi-scale materials is different because the search space of small-scale details is not completely continuous. The meso-scale geometries are defined by different categories, such as woven or bricks structures, and each category has unique properties and representations. There is no “universal formula” that can model the appearances of different categories, which makes the fitting problem highly nonlinear. Therefore, it is almost impossible to



Figure 6.2: Example of bi-scale material in real life.

apply previous optimization-based solutions in a straightforward manner.

In this chapter, we propose a learning-based solution using a convolutional neural network with synthetic data to learn the mapping between two scales. There are major challenges at both scales – the representation of materials at the large scale and the diverse combinations of geometric patterns and basic BRDFs for each facet at the small scale.

In computer vision and graphics the most common representation for learning materials is an image of an instance of the material in a particular context. Images are used due to the simplicity of data collection. However, material appearance in an image context depends on the scene description (including lighting, camera angle, and geometric normals) that are irrelevant to the fitting and could produce unwanted bias in the result. For reliability and efficiency in our method, we propose a novel training pipeline to learn material properties directly from tabulated BRDFs. However, due to its high dimension, it is inefficient to conduct training on densely sampled tabulated BRDFs. We propose a new sampling method to create 2D BRDF slices for training. Compared with existing BRDF tabulations, our method well preserves the spatial features of BRDF by taking advantage of retro-reflection, which according to Dupuy et al. [28] provides an important cue to the microfacet normal distribution function. We analyze the physical interpretations and compare the performance of other BRDF tabular formats to provide explanations for our findings.

For small-scale details, we represent geometries and BRDFs in different categories with different physical parameters to define multiple independent continuous search spaces. According to [148, 37],

learning materials can be interpreted as two processes: classification and estimation. Classification identifies the boundaries separating different material categories and estimation establishes the true position within each category. We follow this framework and put forward an end-to-end model that takes as input a 2D BRDF slice and performs classification and parameter estimation on the small-scale details. The classification is based on predefined categories and the estimation is to fine-tune the corresponding parameters in a continuous search space. This framework also helps us to increase the generality of our model because the gamut of the search space is enlarged. Theoretically, there is no limit on the categories of geometric patterns and basic BRDFs that can be used in training as long as the computational power is available. This approach is not limited by the expressive power of a single BRDF model and we can fit materials with diverse properties.

For evaluation, we conduct experiments to compare the training performance of different tabular formats and explain why retro-reflection provides a strong cue for the learning process. We reconstruct large-scale appearance based on our fitting results and compare with ground truth. The rendering results evaluated with a user study demonstrate that there is no significant visual difference. Experimental results also show that our method can predict accurate small-scale details from real world materials.

In summary, this chapter makes the following contributions:

- A new learning-based solution for bi-scale material fitting that takes large-scale BRDF as input and predicts small-scale details as output.
- A new method that efficiently learns materials using sparsely sampled BRDF by taking advantage of spatial features and retro-reflection.
- An end-to-end model to handle diverse representations and combinations of meso-scale geometries and micro-scale BRDFs by classification and parameter estimation.
- A prototype using our proposed method for material editing and fabrication.

6.2 Related Work

We present background on the bi-scale design problem, microfacet models that relate geometry and appearance, previous work using machine learning in material modeling, and work in BRDF fitting.

6.2.1 Bi-Scale Design

Bi-scale design plays an important role in manufacturing appearance. In manufacturing, creating meso-scale geometry is called texturing (in contrast with the graphics usage of the term texturing.) Texturing molds to create meso-scale geometry such as leather patterns or stipples can make a relatively inexpensive material (such as plastic) look more luxurious, or can make a brand look more distinctive. Meso-scale geometry can also have functional properties such as hiding imperfections and making products easier to grip. Maniscalchi et al. [149] provide an in-depth study of the performance of various mold texture patterns. Several basic template patterns are given by Wisconsin Engraving [150] that can be used as the small-scale details for mold texturing, and St. Paul Engraving [151] gives a step by step introduction to mold texturing. These industry examples demonstrate how bi-scale materials can enrich the gamut of manufactured material appearance.

Several research projects consider bi-scale design for manufacture. Rouiller et al. [152] propose a method to 3D print spatially varying BRDFs by optimizing the normal distribution function (NDF) of discrete facets to match an analytical NDF. Weyrich et al. [153] optimize for a maximally-continuous and valley-minimizing height field to generate a desired reflectance. Zhao et al. [154] create volumetric models of woven cloth by matching an input weave pattern to a sample from a small database of volumetric exemplars. Lan et al. [155] present a method to 3D-print a surface with spatially-varying opaque reflectance and shading frames. These projects all consider specialized, rather than general bi-scale design. Wu et al. [156] propose a solution to prefilter high-resolution displacement maps and BRDFs jointly while preserving material appearance. However, their pre-computation for each micro-structure is time-consuming. Wu et al. [157] present a physically-based interactive system to design large-scale materials by editing small-scale geometry and BRDFs in low-rank matrix formulations. Their system can efficiently simulate material appearance from small-scale details with shadowing and masking effects. Their system provides the basis for our simulation. However, their algorithm suffers from a long pre-computation time and large memory allocation. We improve their algorithm to efficiently simulate a large number of materials for training.

6.2.2 Microfacet Material Modeling

Many analytical models describe large-scale material appearance with the geometry of a microfacet-based BRDF [158, 159, 23]. Walter et al.[160] give a review of microfacet theory and extend it to transmission through rough surfaces. Heitz [161] reviews different masking-shadowing functions in microfacet-based BRDFs. These papers illustrate basic microfacet theories and analytical models but are not concerned with meso-scale structures and bi-scale mapping.

The methods in [162, 163] introduce scattering and diffraction effects in microfacet material simulation. There also has been much progress for different types of microfacet materials, such as Aliaga et al.[164], Dong et al.[165], Nam et al.[166]. Belcour et al.[167] introduce an extension to microfacet theory for rendering iridescent effects caused by thin-films on a rough base layer. Dupuy et al.[168] propose a method to relate an analytical microfacet BRDF model to an input material by solving an eigenvector problem built from backscattering samples. Zhao et al.[169] produce large-scale fabric material appearance from small-scale structures measured with micro CT imaging. Heidrich et al.[170] use precomputed small-scale visibility to calculate large-scale BRDFs with indirect illumination. Kuznetsov et al.[171] propose a method for microfacet material rendering using generative models which can learn the generalized normal distribution functions (GNDF) from latent vectors. However, the geometric optics GNDF they used does not provide an explicit definition for geometry patterns for editing and the fabric GNDF only covers a small gamut of appearance. None of these methods are suitable for systematically simulating a large number of varying meso-scale structures for bi-scale training.

6.2.3 Inverse Rendering and BRDF Fitting

Traditional inverse rendering and BRDF fitting algorithms can also be used to specify materials from a particular appearance. Li et al. [172] derive a probabilistic formulation to jointly estimate the shape and BRDF of objects under known lighting from a synthetic dataset. Romeiro and Zickler [173] try to infer BRDF from a single image of a known shape in an unknown lighting environment, by assuming a statistical distribution of natural illumination. Many BRDF fitting algorithms [7, 8, 9, 10, 11, 12, 13] have focused on using analytical BRDF models to fit the MERL dataset [26]. Dupuy et al.[168] proposed an iterative method to extract the microfacet parameters from anisotropic materials. All of

these methods try to map a material appearance to a specific BRDF model, which can only cover a limited gamut of appearance. None of these algorithms provide a bi-scale description. The study closest to our work is Wu et al.[14]. They propose a search-based inverse rendering method; they search through libraries of materials and meso-scale geometries to find the best combination for a specified appearance. However, the searching results are the “nearest neighbor” defined in the training set, which limits reconstruction accuracy. We provide a detailed comparison between our work and theirs in Section 6.5.2.

6.2.4 Learning Materials in Image Space

Many projects relate appearance to material descriptions using machine learning techniques. Most of them rely on image-based training, where the same material sample is repeatedly rendered with different scenes to cover different appearances [174, 175, 176, 177, 178, 179, 180, 181]. They generate synthetic images as training data, where the same material is repeatedly rendered using a single BRDF model with different lighting and camera angles on a fixed geometry (sphere or plane). Normally, the gamut of their model is limited due to the single parametric BRDF model being used (Ward or Phong in many cases). Furthermore, iterating over different lighting conditions and other irrelevant factors is a waste in terms of sampling, and significantly increases the computational time and storage for the training set. Another disadvantage is the possible overfitting of the rendered scenes since the objects and lighting used for rendering could bias the training results. Zsolnai-Feh’er et al. [182] present an image-based learning system to learn shader parameters from rendered images with fixed lighting and viewing angle. However, their setting is tied to the Disney Principal Shader [72] and is customized for the input of their design system, which cannot be applied to other scenarios. To avoid sampling redundancies and reduce the dimension of the training set, we propose a tabular BRDF training scheme to learn appearance efficiently from BRDFs instead of from rendered scenes.

6.3 Method

Our goal is to find the combination of meso-scale geometries and micro-scale BRDFs that can accurately reconstruct the input material appearance. Our method takes as input macro-scale BRDFs in 2D slice tabular format and outputs the categories and related parameters for meso-scale geometry

and micro-scale BRDF. We conduct our training on synthetic data created from physically-based simulation (Section 6.3.1). We define the tabular BRDF as a 2D slice subset from the complete 4D BRDF (Section 6.3.2). We use an end-to-end model to find the small-scale representations that can accurately reconstruct the large-scale appearance (Section 6.3.3). The training data is generated in gray-scale by averaging the RGB of micro-scale BRDF for dimension reduction. Otherwise, the dimension of the training set will increase polynomially. To restore colors and enrich the gamut of our model, we propose a method to predict the multi-color weights for different parts of the meso-scale geometry after training (Section 6.3.4). In this chapter, we assume the macro-scale BRDF has been specified by the designer.

6.3.1 Simulation

We use synthetic data for training since it can be collected from computation easily (labeled bi-scale material data relating macro BRDF to small-scale details is difficult to obtain for physical samples). However, a concern is the speed of the simulation. State-of-art microfacet modeling methods focus on accuracy. The underlying structure is resolved in pixels in the rendering to produce very high-quality material appearance. However these methods are not suitable in our case due to the lengthy rendering time and implicitly defined meso-scale structures. Therefore, based on previous work [157, 183], we improve the simulation to efficiently approximate large-scale appearance using explicitly defined meso-scale geometries. Our simulation method is physically correct in accounting for shadowing and masking effects and runs at an interactive speed.

Following [157], we define

$$\bar{f}_r(\boldsymbol{\omega}_i, \boldsymbol{\omega}_o) = \frac{1}{a_v(\boldsymbol{\omega}_o)} \int_{S^2} f(\mathbf{n}, \boldsymbol{\omega}_i, \boldsymbol{\omega}_o) \gamma(\mathbf{n}, \boldsymbol{\omega}_i, \boldsymbol{\omega}_o) d\mathbf{n} \quad (6.1)$$

where \bar{f}_r is the macro-scale BRDF, f is the micro-scale BRDF, γ is the Bidirectional Visible Normal Distribution Function (BVNDF) computed from the normals of meso-scale geometry; $\boldsymbol{\omega}_i$ is the incident direction and $\boldsymbol{\omega}_o$ is the outgoing direction. $a_v(\boldsymbol{\omega}_o)$ is the visible projected area of a surface patch along $\boldsymbol{\omega}_o$, and S^2 is the surface of unit sphere. We tabulate the BVNDF N and micro-scale BRDF M as matrix format:

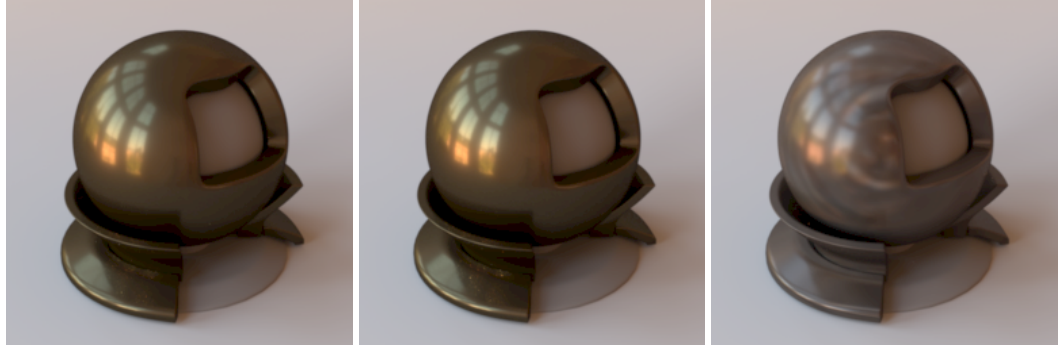
$$\begin{aligned}
\bar{f}_r(\boldsymbol{\omega}_{i,k}, \boldsymbol{\omega}_{o,k}) &\approx \frac{\sum_j f(\mathbf{n}_j, \boldsymbol{\omega}_{i,k}, \boldsymbol{\omega}_{o,k}) \gamma(\mathbf{n}_j, \boldsymbol{\omega}_{i,k}, \boldsymbol{\omega}_{o,k})}{a_v(\boldsymbol{\omega}_o)} \\
&= \frac{1}{a_v(\boldsymbol{\omega}_o)} \sum_j \mathbf{N}_{kj} \mathbf{M}_{jk}^T
\end{aligned} \tag{6.2}$$

$$\mathbf{N}_{kj} = \gamma(\mathbf{n}_j, \boldsymbol{\omega}_{i,k}, \boldsymbol{\omega}_{o,k}) \tag{6.3}$$

$$\mathbf{M}_{jk}^T = f(\mathbf{n}_j, \boldsymbol{\omega}_{i,k}, \boldsymbol{\omega}_{o,k}) \tag{6.4}$$

Each row of \mathbf{N} represents the distribution of normals of a patch subset that are visible along $\boldsymbol{\omega}_{i,k}$, $\boldsymbol{\omega}_{o,k}$, and each column of \mathbf{M} stores a tabulation of cosine-weighted BRDF, where \mathbf{n}_j defines the local frame. We can precompute the \mathbf{N} and \mathbf{M} and to perform efficient simulation by querying values from the matrices. Refer to [157] for details of the tabulation and applying SVD on matrix \mathbf{N}

For matrix \mathbf{M} , instead of uniformly mapping the rotated BRDF to a 2D grid using paraboloid maps[184] as in the original method, we use a data-driven method to importance sample the micro-scale BRDF [28], which can significantly reduce the precomputation time and artifacts in simulation. We first apply a log-relative mapping for a given BRDF, $\rho = \log(\rho \cos Map + \varepsilon)$ [57] to reduce the order of magnitude of the specular peak, where ε is set to 10^{-3} to avoid a singularity at zero. For each incident direction, we calculate a BRDF slice of possible outgoing directions weighted by the VNDF, which is computed from the retro-reflection. To importance sample the BRDF, we warp uniform variates on a unit grid so that their density is proportional to the luminance of the associated BRDF slice. To evaluate the BRDF values in \mathbf{M} , we first compute the half-direction vector and map it to local coordinates. Then we apply the inverse warp by the NDF and use the results to perform a lookup in the original BRDF slices to compute the BRDF value. The warp function details can be found in [28]. After filling the BRDF values in \mathbf{M} , we apply random-projection to accelerate SVD for the matrix. During the simulation, we first reconstruct \mathbf{M} from SVD, and then apply linear interpolation between samples and undo the log-relative mapping to get the BRDF value for the specific rotated normals. Figure 6.3 demonstrates a comparison between our improved simulation and the original [157] using gold-metallic-paint3 from the MERL dataset. The result shows that our method provides better reconstruction accuracy due to importance sampling. Also since our method



Reference

Ours

Wu et al.

Figure 6.3: Comparison of bi-scale simulations.

does not need to compute every single direction, the pre-computation time is decreased from the original 24 hours [157] to 40 minutes for this example.

Our simulation is an approximation for bi-scale materials, and we only use it to build the mapping between the material scales in our training. For meso-scale structures with steep slopes coupled with high-albedo micro-scale BRDFs interreflections, which are not accounted for in our simulation, would have a noticeable impact. However, as we will demonstrate in Section 6.6.2, our simulation works well with our model to predict small-scale details for real world materials. Alternative simulation methods could be used if sufficient computational power is available.

6.3.2 Tabular BRDF Representation

The reflectance properties of a material are embedded in a 4D macro-scale BRDF, which includes millions of entries when incident and outgoing directions are densely sampled. It is almost impossible to directly learn from such a representation. We need to intelligently sample the BRDF and keep its important features for learning. We represent macro-scale BRDF as a 2D tabular format, where each entry represents the BRDF value corresponding to a specific combination of incident and outgoing directions. The benefit of the 2D format is that the directions vary continuously, which allows us to learn BRDF gradients. We examine four tabular BRDF representations by analyzing their physical interpretations. We denote r, c as row and column index of the tabular BRDF and ω_i, ω_o as incident and outgoing directions respectively.

Sphere Table. The sphere table is constructed by fixing viewing direction and varying incident

direction sampled from a hemisphere [178, 185]. Figure 6.4 shows the specular peak concentrates on the center of the table and the diffuse part is located around the specular peak. The edge of the sphere represents the BRDF values of grazing angles. In the following equations, resolution n is used for normalization.

$$\omega_o = (0, 0, 1)$$

$$\omega_i = (1 - \frac{2r}{n}, 1 - \frac{2c}{n}, \sqrt{1 - (1 - \frac{2r}{n})^2 - (1 - \frac{2c}{n})^2})$$

Retro-Reflectance Table. This table samples retro-reflectance directions along the hemisphere to stress the contribution of meso-scale facets whose normals are oriented towards the incident direction. Hence, we can see that the specular peak is more converged to the center compared with the Sphere Table.

$$\omega_o = \omega_i = (1 - \frac{2r}{n}, 1 - \frac{2c}{n}, \sqrt{1 - (1 - \frac{2r}{n})^2 - (1 - \frac{2c}{n})^2})$$

Dense-Sampled Table. Adapted from the UTIA parameterization [186], the Dense-Sampled Table uniformly samples $p = 45$ from the azimuthal angles $\theta \in [0, \frac{\pi}{2}]$ and $q = 36$ from the polar angle $\phi \in [0, 2\pi]$ for both incident (rows) and outgoing (columns) directions. We increase p and q from the original parameterization to avoid significant discontinuities and “aliasing” problems. We use fewer samples for ϕ because BRDF values vary smoothly along this direction. The left top corner of this format represents the specular peak. The longest diagonal line represents the retro-reflective measurements and its value decreases when θ increases. Other highlighted diagonal lines represent specular lobes at different angles. The right and bottom parts represent the grazing angles.

$$\begin{aligned} \omega_{o,\theta} &= \text{floor}(\frac{c}{q}) \frac{\pi}{2p}, & \omega_{o,\phi} &= (c \bmod q) \frac{2\pi}{q} \\ \omega_{i,\theta} &= \text{floor}(\frac{r}{q}) \frac{\pi}{2p}, & \omega_{i,\phi} &= (r \bmod q) \frac{2\pi}{q} \end{aligned}$$

Half-Angle Table. The Half-Angle Table is constructed using the 2D slice in the Rusinkiewicz coordinate system. The slice is taken at $\phi_d = 90^\circ$ because it maximizes the valid region of the $\theta_d - \theta_h$

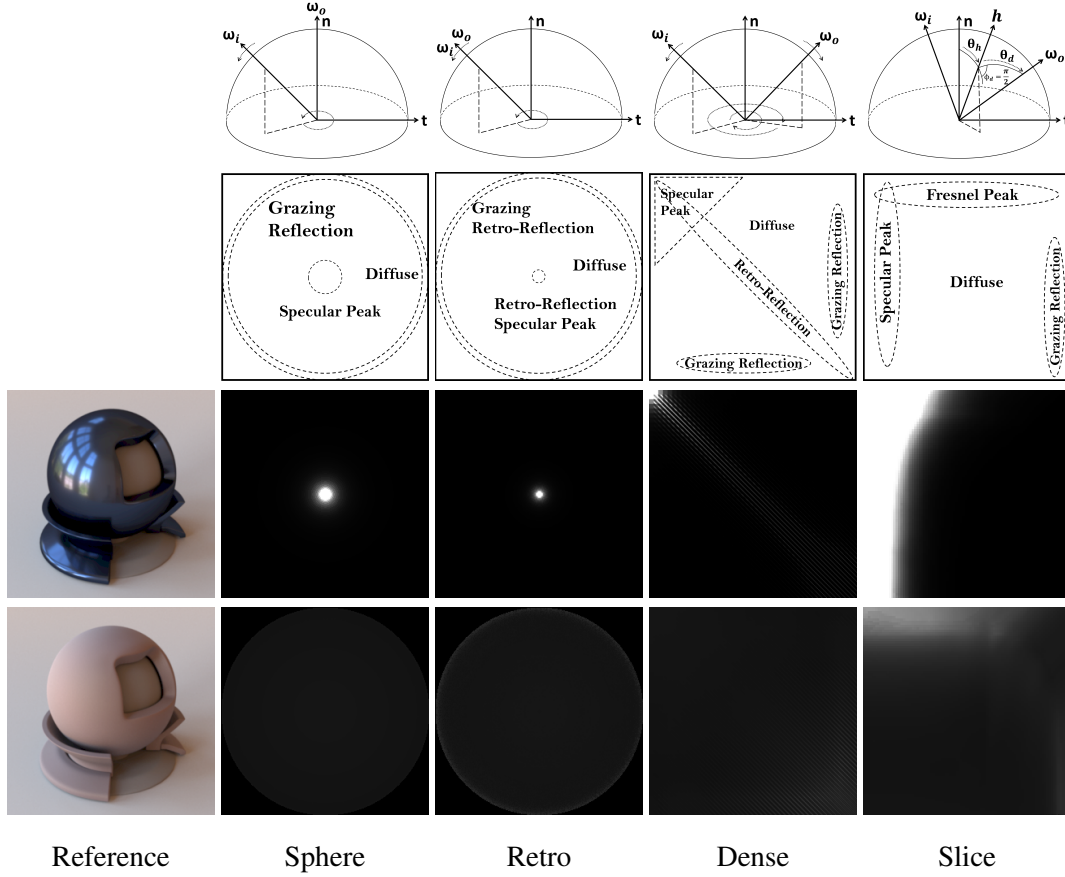


Figure 6.4: Examples of different tabular BRDF formats.

slice. The square root of θ_h is uniformly sampled from 0 to $\frac{\pi}{2}$, which provides denser sampling close to 0, in the region of the specular highlight. The physical meaning of this representation has been introduced in [72].

$$\theta_h = \left(\frac{r}{n}\right)^2 \frac{\pi}{2}, \quad \theta_d = \frac{c}{n} \frac{\pi}{2}, \quad \phi_d = \frac{\pi}{2}$$

We visualize different tabular BRDFs using two examples from the MERL dataset and demonstrate their physical interpretation in Fig. 6.4. We compare the training performance of these formats for learning bi-scale representations in section 5.1. We use the result of the comparison to choose the BRDF representation for our final bi-scale training.

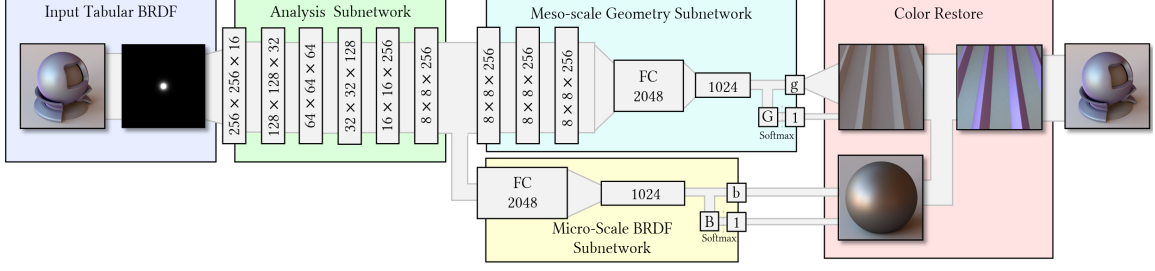


Figure 6.5: The pipeline of our bi-scale learning model and network architecture.

6.3.3 Network Architecture

Figure 6.5 shows our end-to-end training pipeline. Given a target macro-scale BRDF, we first create the 2D tabular format and feed it into the network. Our model learns the spatial features from tabular BRDFs, then categorizes the meso-scale geometry and micro-scale BRDF into pre-defined categories and fine-tunes their corresponding parameters within each category. Based on our observations, different categories can significantly change the appearance while the physical parameters influence the details, such as the shape of the highlight. For the micro-scale BRDF, the pre-defined categories include measured BRDFs (each one is a single category) and analytical ones (a separate category). Introducing measured BRDFs can significantly increase the gamut of our fitting model due to their complex and special reflectance behaviors. The physical parameters for the the micro-scale BRDF are only defined for analytical models including roughness, diffuse and specular albedo. For the meso-scale geometry, the category is defined by different primitives that are procedurally modeled, such as grooves, woven threads and so on. Geometries generated from texture height maps are not included since they are not intuitive for editing, and they are left to future work.

Our network includes three units. The first is an analysis subnetwork of six convolution layers, each followed by a batch-normalization layer and an ReLu activation layer [187]. Each convolution has a kernel size of 7×7 and a stride of 2. The analysis subnetwork is designed to extract the spatial features from tabular BRDFs, which are fed into the following subnetworks in separate branches. The second is a meso-scale geometry unit, which includes three convolution layers and two fully connected layers. Then we split the features into two sub-branches, each of which goes through an extra fully connected output layer with \mathbf{G} (number of categories) and \mathbf{g} (dimension of physical parameters) hidden units respectively. The third, micro-scale BRDF, unit shares a similar

branch structure (\mathbf{B} denotes the number of category and \mathbf{b} represent the parameters of analytical model) but with fewer convolutional layers to prevent overfitting due to its smaller search space. We find the joint learning on classification and parameter estimation have a better performance than learning separately, because the training errors on either side will be propagated to the other and back-propagated to the network. It also explains why the joint training of meso-scale geometry and micro-scale BRDF performs better than other network structures. We will presents the results of ablation tests in Section 6.5.2.

The loss function for our network includes category loss ($\mathcal{L}_{GeomClass}$ and $\mathcal{L}_{BRDFClass}$) and parameters loss ($\mathcal{L}_{GeomParams}$ and $\mathcal{L}_{BRDFParams}$). We apply a softmax layer at the end of the network to calculate the Cross-Entropy for category loss, and define the L2 loss between the predicted parameters and the input labels as parameter loss. All the parameters are normalized into the same range for training. We combine those loss terms using a weighted sum. The total loss function is defined as:

$$\begin{aligned}\mathcal{L}_{total} = & \lambda_1 \mathcal{L}_{GeomClass} + \lambda_2 \mathcal{L}_{BRDFClass} \\ & + \lambda_3 \mathcal{L}_{GeomParams} + \lambda_4 \mathcal{L}_{BRDFParams}\end{aligned}\tag{6.5}$$

where $\lambda_1 = 1$, $\lambda_2 = 10$, $\lambda_3 = \lambda_4 = 20$. We assign more weight to the BRDF category loss to improve the network performance for distinguishing between the measured and analytical BRDFs. We found that by adding up the loss functions, the classification and regression results are penalized by each other resulting in lower training loss.

6.3.4 Color Restoration

Given the predicted achromatic results, we need to restore the color to match the target material. One advantage of fitting bi-scale materials is that we can assign different colors to different facets to introduce spatially varying and anisotropic effects. We denote \mathbf{C} as a color matrix defined in RGB and each row $\mathbf{c}_j = (c_{j,r}, c_{j,g}, c_{j,b})$ is a color weight for a facet. To apply the color weight, we first cluster the facets into different groups based on their normals using the BVNDF obtained from Equation 6.3. We can use the geometric partition to guide the clustering, where each group represents a component of geometric structure, such as the face, ridge, slope and so on. We then

apply the corresponding color weights to the facets in each group by replacing the BVNDF matrix \mathbf{N} with $(\mathbf{C}_r \cdot \mathbf{N}, \mathbf{C}_g \cdot \mathbf{N}, \mathbf{C}_b \cdot \mathbf{N})$, where

$$\mathbf{N}_{kj} \leftarrow c_{j,l} \cdot \mathbf{N}_{kj} \quad \text{and} \quad l \in \{r, g, b\} \quad (6.6)$$

Assigning color weights can significantly change the appearance. For example it can introduce color variation at grazing angles. To obtain the color matrix, we use an image-based optimization with the following objective function:

$$\min_{\mathbf{c}_l} d(f, \bar{f}_r) \quad (6.7)$$

Where d is the distance metric, f is the target BRDF and \bar{f}_r is defined by plugging Eq. 6 into Eq. 2.

$$\bar{f}_r(\boldsymbol{\omega}_{i,k}, \boldsymbol{\omega}_{o,k}) = \frac{1}{a_v(\boldsymbol{\omega}_o)} \sum_j \text{Concat}(\|_{l \in \{r,g,b\}} c_{j,l} \cdot \mathbf{N}_{kj}) \mathbf{M}_{jk}^T \quad (6.8)$$

We optimize the color weights in image space, where a perfect sphere is used and lit by an environment map [135] under orthographic projection. We define the distance metric as

$$d(f_1, f_2) = \|R \cdot f_1 - R \cdot f_2\|_2 \quad (6.9)$$

where R is the light transport matrix transferring a BRDF into an image. Please refer to Sun et al. [13] for a detailed evaluation of different metric functions. We compute the per-pixel difference for the entire sphere to take into consideration the BRDF values at both the specular peak and the grazing angles. After optimization we can collect the color weights and reconstruct the chromatic large-scale appearance.

6.4 Implementation

We use the algorithm from Section 3.1 to create a bi-scale training set. For micro-scale BRDFs, we include 100 materials from the MERL dataset and 300 analytical BRDFs sampled from GGX Cook-Torrance models. These analytical BRDFs are created by randomly sampling roughness, diffuse and specular albedo in [0,1]. For meso-scale geometries, we procedurally generate 2000 meso-scale geometries by randomly sampling their physical parameters in their valid ranges (i.e. no

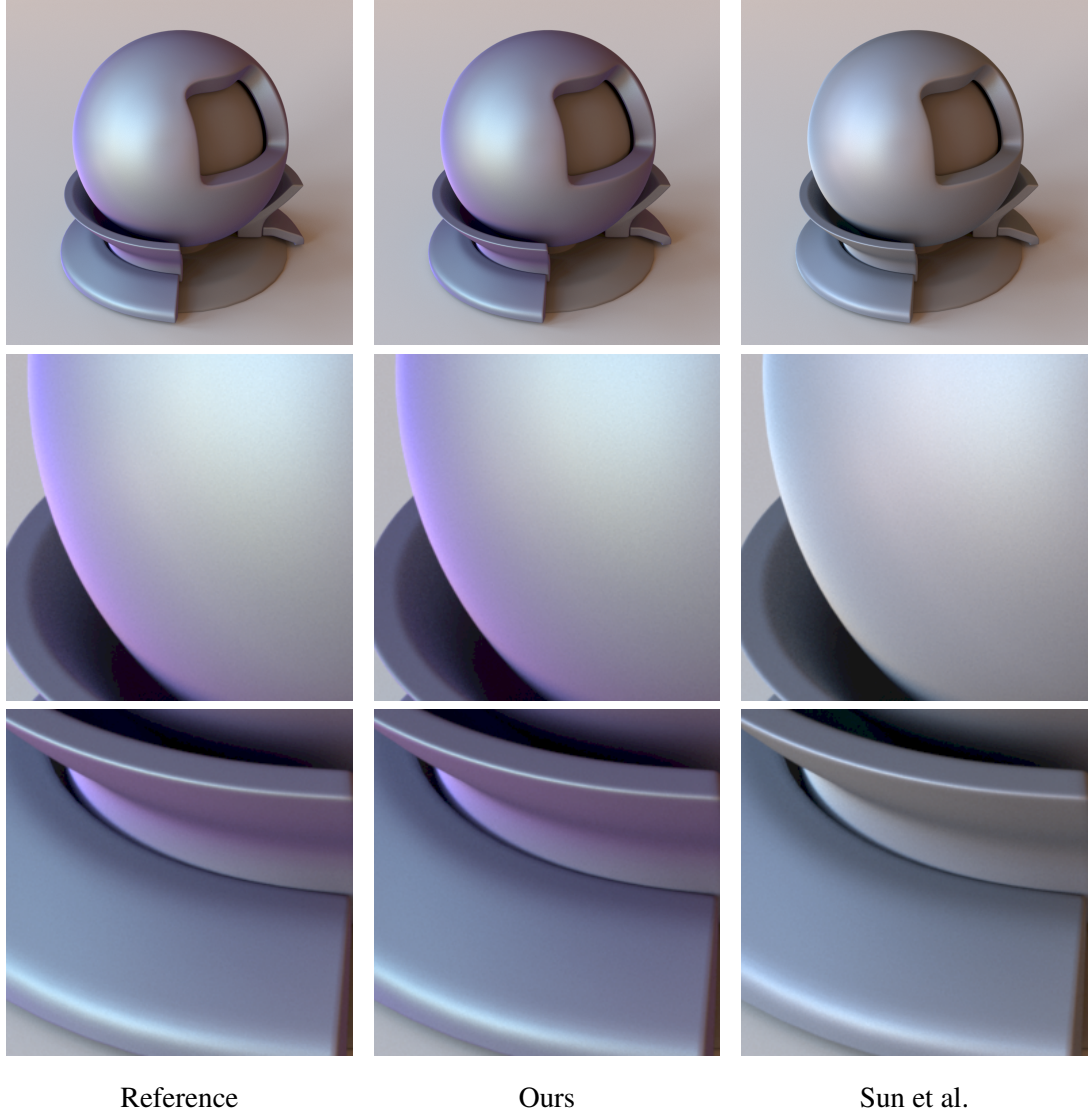


Figure 6.6: Compared to other color optimization approaches.

collision and global scale) from 8 basic geometry categories (Fig. 6.7). The details of the range and definition of physical parameters can be found in supplemental materials. All the physical parameters are normalized to $[0,1]$ during training and denormalized for reconstruction.

For comparison, we train four different networks using the same training samples but with the different tabular BRDF formats described in Section 3.2. The resolution for all tabular BRDFs is defined as $n = 256$. The Dense-Sampled Table is first created in its original resolution (45×36) and then down-sampled to 256 (directly creating Dense-Sampled Table in low resolution may lead to discontinuities and jumps). To reduce the size of the training set and time for simulation, we

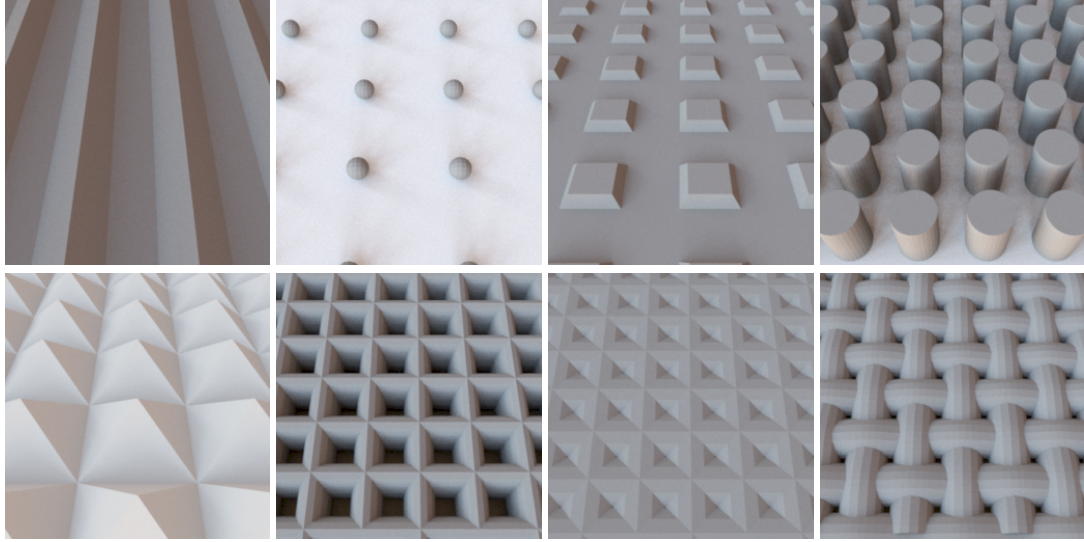


Figure 6.7: Examples of different meso-scale geometry primitives used for simulation.

use achromatic tabular BRDF by averaging the color channels for measured BRDFs and sampling parameters in gray-scale for analytical BRDFs. The simulation requires roughly a week on a standard machine for each dataset. We will open source these datasets for future research projects.

We implement our network using Caffe2 [188] and the ADAM optimizer [189] with a learning rate of 10^{-3} . The total training process took around 18 hours for 250000 iterations with a batch size of 32 on a computer with an AMD Ryzen 7 1700X 8-core CPU, 16 GB RAM and an NVIDIA GeForce GTX 1070 GPU.

6.5 Results

We first evaluate the proposed tabular BRDF training by comparing the performance of different tabular formats and analyzing their spatial features (Section 6.5.1). Then we provide the experimental results from our bi-scale fitting model and conduct an ablation study (Section 6.5.2). We then compare our method with existing solutions (Section 6.5.3) and validate our method with real-world materials (Section 6.5.4).

Table 6.1: Evaluation of Different Tabular BRDFs (8500 samples)

	Sphere	Retro-Reflectance	Dense-Sampled	Half-Angle Table
BRDF Mismatches	13	7	17	15
Geom. Mismatches	25	5	10	50
Parameter MSE	0.0064	0.0042	0.0041	0.0065

Table 6.2: Ablation Study (8500 samples)

	Our Model	Model 1	Model 2
BRDF Mismatches	7	42	8
Geom. Mismatches	5	32	7
BRDF Parameter MSE	0.0037	0.0076	0.0081
Geom. Parameter MSE	0.0043	0.0056	0.0051

6.5.1 Tabular BRDF Analysis

We consider the training results for different tabular formats and evaluate the embedded features. Similar to the creation of the training set, we generate 8500 test samples by randomly sampling the parameters and create a test set for each format. To avoid bias, there is no overlap between test samples and training samples. We use two metrics to evaluate network performance. For classification, we measure the number of mismatches between the predicted category and ground truth used to generate the test sample. For the parameter estimation, we compute the mean squared error for each normalized dimension between the prediction and ground truth.

We list the prediction errors in Table 6.1. In Fig. 6.8, we visualize an example of our fitting results using different tabular BRDFs. The bottom row shows the difference between the prediction and the ground truth magnified by 10 times. The results show that the Retro-Reflectance Table and the Dense-Sampled Table have better performance compared with the other two. The difference between the Sphere Table and the Retro-Reflectance Table is the shape and intensity of the specular peak. The Sphere Table has a relatively larger specular peak area and blurry boundary, which indicates that BRDF values decrease smoothly as θ_i gradually increases (small BRDF gradients). By contrast, the Retro-Reflectance Table has a smaller specular peak area and clear cut-off on the boundary, which indicates larger BRDF gradients in the retro-reflective angles. The large gradient comes from a significant jump of BRDF value, which is often caused by the change of sampling directions from the specular domain to the non-specular domain. Also note that the Retro-Reflectance Table has a higher range of BRDF values (larger intensity for specular areas and lower for diffuse areas) compared with the Sphere Table. For the Dense-Sampled Table, the sharp boundaries between highlighted diagonal

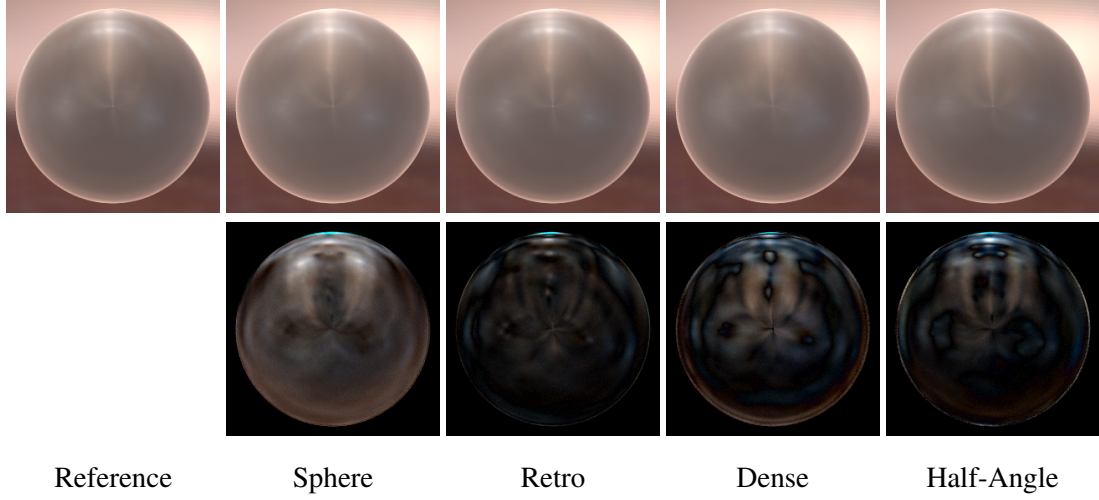


Figure 6.8: Comparison of reconstructed anisotropic appearance for different tabular formats with 10 times difference between predictions and the ground truth.

lines and dark areas indicate large BRDF gradients, separating the specular and diffuse area. As for the Half-Angle Table, the specular area smoothly blends into the diffuse area with a blurry boundary due to the small gradients in both the θ_h and θ_d increasing directions. Similar to the Sphere Table, the construction of the Half-Angle Table forces the BRDF value varies slowly between neighbors. These observations, combined with the training results, suggest that the large gradient components displayed in the Retro-Reflectance Table and the Dense-Sampled Table are important features to learn and distinguish BRDF in training.

To further explain our observations, we display the feature maps from the fifth convolutional layer of the analysis sub-network in Fig. 6.9. As we can see, after five convolutions, basically only the shape of the specular area remains on the feature maps. We also notice that the pattern in the Retro-Reflectance Table and the Dense-Sampled Table are much clearer and the shape is more consistent with the input, while the patterns in the Sphere Table and the Half-Angle Table’s feature maps look blurry. For example, the Sphere Table has a distorted circle for the specular peak with non-uniform intensity in both examples, while the Retro-Reflectance Table maintains a relatively clear and uniform circle. This indicates that the small gradients vanish and the large gradient components can remain after convolutions. Similarly, for the Half-Angle Table, most of the feature maps almost lose the pattern from the input, while the Dense-Sampled Table displays sharp diagonal line patterns in the feature maps. These results largely match with our observation:

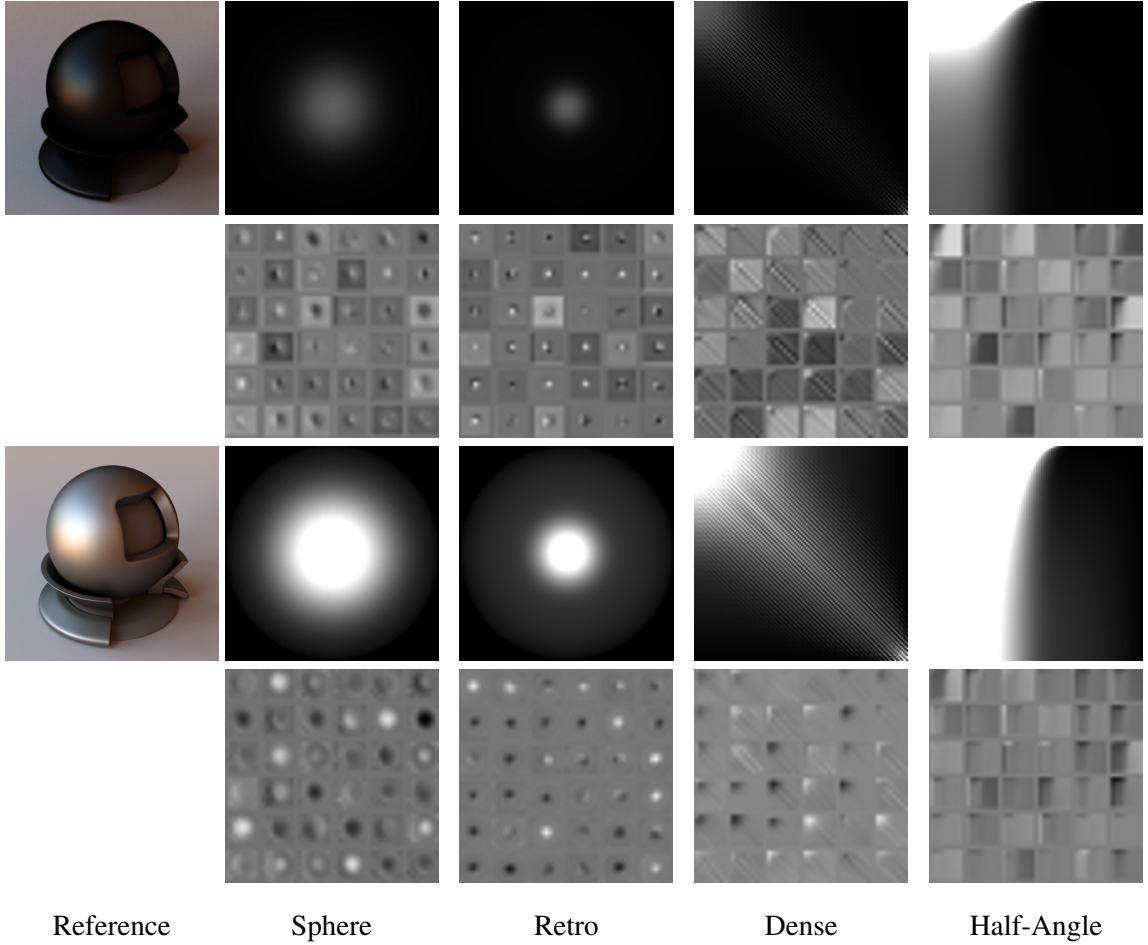


Figure 6.9: Two example materials and the feature maps of tabular formats from the fifth convolutional layer.

the large gradient components in the original tables lead to distinguishable patterns in the feature maps and contribute to learning material appearance.

We also experimented with 20 network settings, including different hyperparameters, weights, optimizer and number of convolutional layers. Although the absolute errors vary for each experiment, the Retro-Reflectance Table in most cases maintains the lowest errors. Although our conclusion is based on experiments and observations, we still want to stress the unique property of retro-reflectance for learning materials, which has been used in recent work such as Dupuy et al. [28] to retrieve the microfacet NDF. Our experimental results can provide insights for studying retro-reflection behavior in material learning and fitting. For the rest of the chapter, we use the Retro-Reflectance Table for our evaluation.

6.5.2 Training results

Neural network training. To evaluate bi-scale fitting results, we randomly select and render 200 samples from the previous test set. In Fig. 6.10, we display three of the best- and worst-cases and their four times difference from the ground truth. We use PSNR to measure the difference between our results and ground truth materials in image space. Also, we display the rendered small-scale details for comparison. In each case, the predicted images were close to indistinguishable from the ground truth for both scales.

Ablation Study. We compare our end-to-end model with two alternative structures and present results in Table 6.2. The first one is a separate training model, where we use three different networks to learn parameters, meso-scale geometry categories and micro-scale BRDF categories respectively (denoted as Model 1). We split the loss function defined in Equation 5 and use them for each network. The second one is a “one Branch” model, where no subnetwork exists and the input features go through the exact same network to output the meso-scale geometry and micro-scale BRDF (Model 2). The same loss function in Equation 5 is used. Each model is trained on the same training set and evaluated on the same test set. Compared with the results of Model 1, our network has a better performance in both classification and parameter estimation due to the existence of the shared analysis subnetwork and joint optimization. The loss of all branches back-propagates to the shared analysis subnetwork and optimize the weights together. Compared with Model 2, our network outperforms in parameter estimation with smaller MSE for micro-scale BRDF parameters. Using a single branch network to predict the meso-scale geometry and micro-scale BRDF together may cause overfitting because the search space of the micro-scale BRDF is much smaller. Our model, on the contrary, uses different subnetworks to process the meso-scale geometry and micro-scale BRDF to handle the two components, which provides more accurate fitting results.

6.5.3 Comparison

We compare our method with existing solutions, including the inverse bi-scale design Wu et al. [14] and Sun et al. [13] to demonstrate the fitting capability and gamut of different models. Wu et al. use a data-driven search based solution while Sun et al. fit BRDF into the GGX model using numerical optimization. We first randomly sample 200 BRDFs with uniform color-weights using our simulation

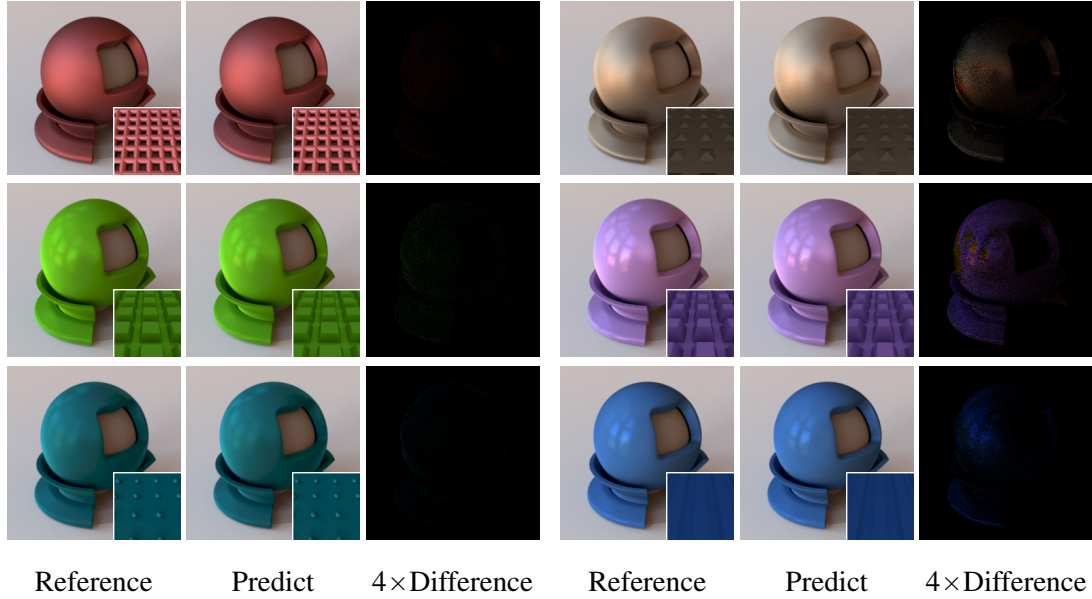


Figure 6.10: The best (left side) and worst-case (right side) predictions on a set of 200 images.

Table 6.3: Comparison of 200 randomly sampled materials

	Time(sec)	Isotropic PSNR(db)	Anisotropic PSNR(db)
Ours	0.71	42.36	34.65
Wu et al.	26.78	38.43	30.38
Sun et al.	30.68	42.81	31.67

method. Four randomly selected examples are presented in Fig. 6.11 and the statistics averaged over the 200 samples are listed in Table 6.3. We use the same training data for Wu et al. and our model. Based on the rendered results and PSNR value, we can observe the limited accuracy of their predictions since their results are exactly taken from the training samples. In our case, meso-scale geometries and micro-scale BRDFs are jointly optimized and defined in a continuous search space, which leads to higher reconstruction accuracy. Note that their method could be improved using their original dataset, but it is not available. We believe the comparison is still fair because the two methods are evaluated on the same training and test set. For Sun et al., the results from the two methods share similar visual appearance. However, their method does not provide small-scale details and requires more time to converge.

We also sampled 200 anisotropic materials for comparison, which are created using either anisotropic micro-scale BRDFs or multi-color weights for meso-scale geometries. Fig. 6.12 presents

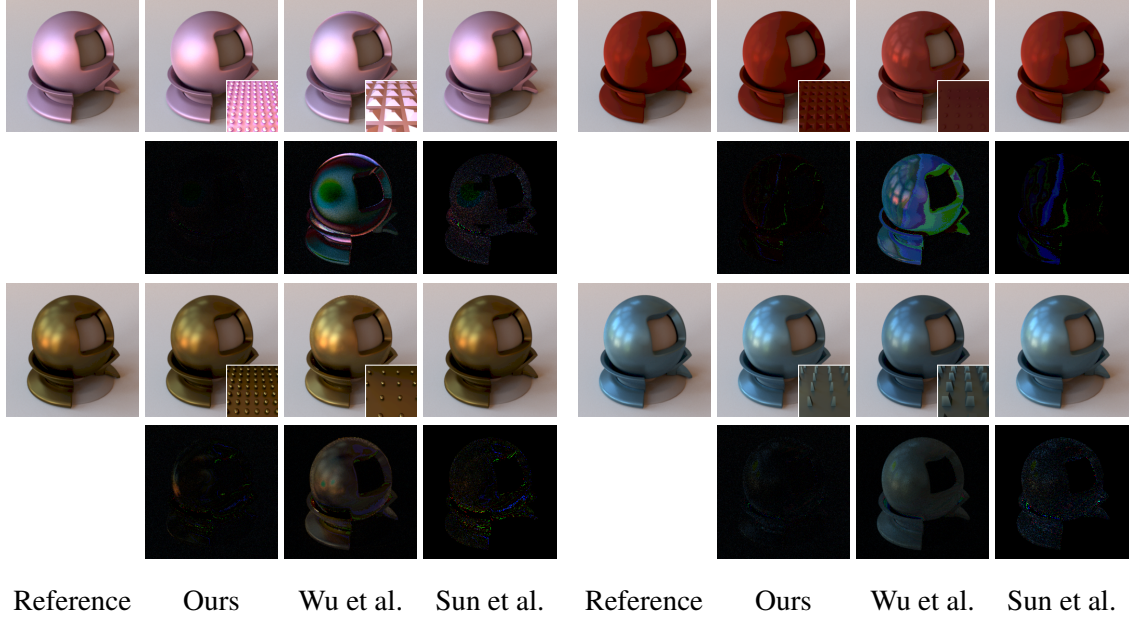


Figure 6.11: Qualitative comparison ($4 \times$ difference) between our method and previous work.

the selected results. As we can see from the zoomed images, compared with the other two methods, our method largely recovers the Fresnel effect at the grazing angle and faithfully maintains the color of the specular area from the ground truth. For Wu et al., the homogeneous color is selected from a predefined set of random colors. We can see that the discrete samples are not enough to cover a large gamut of appearances, leading to inaccurate colors for reconstruction. Sun et al. does not reconstruct BRDFs with varying color and can only yield an average color. Due to the limited gamut of the analytical model, their algorithm also fails to capture anisotropic effects. For both of these two methods, uniform colors are used to scale the achromatic BRDFs resulting in less variation in appearance. Our method, on the contrary, optimizes the spatially varying color weights on the small-scale details, leading to a wide variety of possible appearance.

We conduct a user study to further compare the three methods using Amazon Mechanical Turk. During the experiment, we gave users four images (one ground truth and three candidates) with materials rendered in the same settings, similar to the examples in Fig. 6.12 but without microstructures on the corner. We asked users to compare and select the candidates in order based on the visual similarity to the ground truth (most similar to least similar). We randomly selected forty groups of materials from the previous test set with half isotropic and half anisotropic materials. We presented

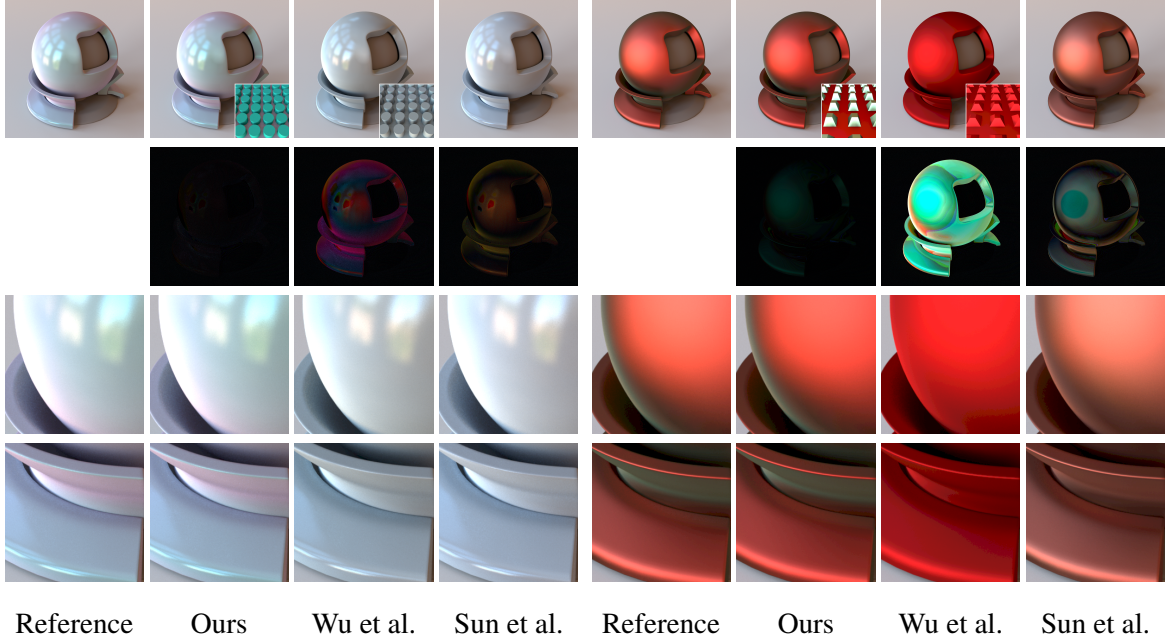


Figure 6.12: Qualitative comparison ($4 \times$ difference) between our method and previous work for multi-color materials.

the candidates anonymously and in random orders. Each group of materials was evaluated by 30 users independently without a time constraint. Fig. 6.13 demonstrates the results. Our method gets most of the votes for most similar to ground truth in both the isotropic and anisotropic cases (76.0%), significantly outperforming the other two methods. The percentage of isotropic materials voted for our method (70.5%) is slightly less than that of anisotropic materials (81.3%). It is interesting to see that our method shares similar PSNR value with Sun et al. for isotropic materials but still gets more votes from users. We believe it is because some of the reconstructions from Sun et al. have color off on the edge of the globe. Overall, the results from the user study match with the quantitative evaluation in Table 6.3.

6.5.4 Validation on measured materials

We also validate our algorithm using 41 measured BRDFs from the material library created by Dupuy et al. [28], which are not included in the training set. Fig. 6.14 demonstrates the bi-scale prediction and reconstruction results. We show the rendered image of reference BRDFs, our reconstruction and predicted micro-scale BRDFs and meso-scale geometries. The average PSNR for the differences

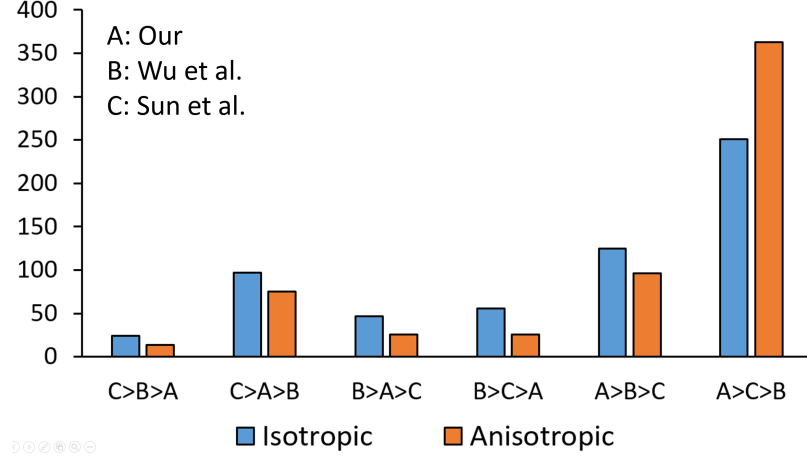


Figure 6.13: Results of user study using Amazon Mechanical Turk.

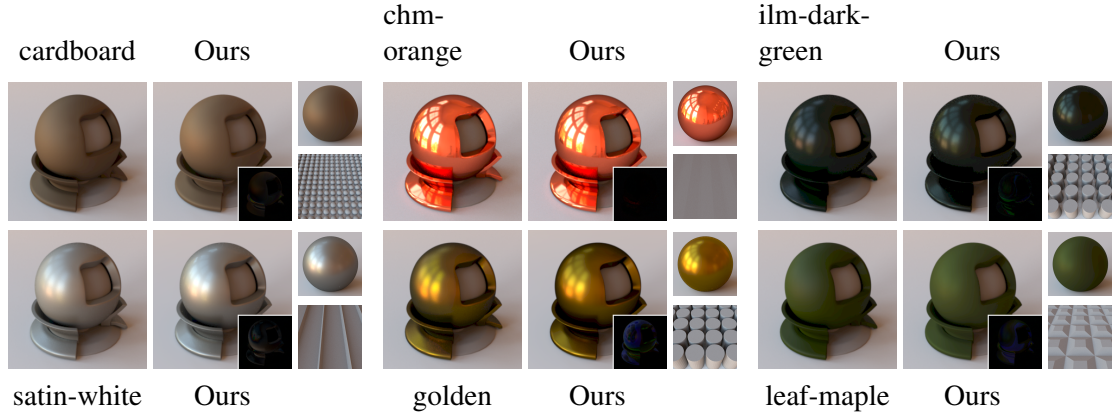


Figure 6.14: Validation on measured materials from RGL material database.

between our predictions and ground truth is 31.57dB, where the maximum is 50.56dB and the minimum is 20.75dB. From the results, we can see that our predictions capture both the intensity and color to a large extent. In Fig. 6.15, we qualitatively compare our results with ground truth over RGB channels separately using a slice of BRDF along the mirror direction, where we vary θ_d while fix θ_h at 0. We also show the comparison of the BRDF lobes at different angles. Our method is accurate by largely following the curve of the ground truth BRDFs in the specular part and the area of grazing angles.

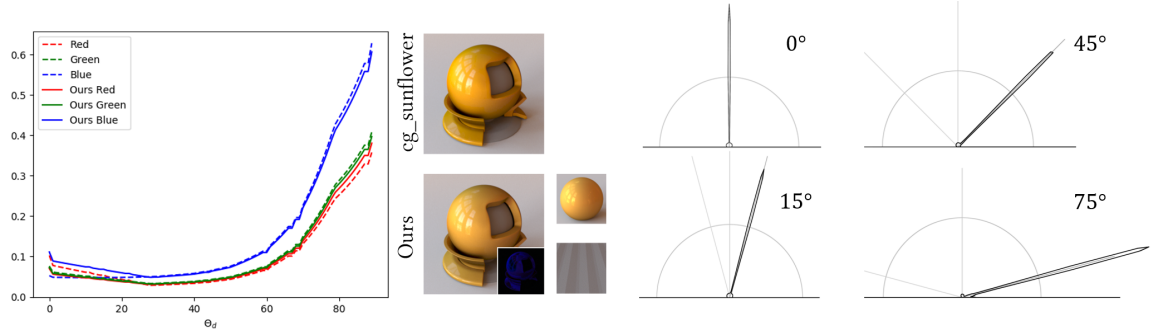


Figure 6.15: The BRDF slice along the mirror directions and lobe comparison.

6.6 Applications

6.6.1 Bi-scale design

The proposed bi-scale fitting provides a new material editing scheme to fine-tune a given material appearance in an intuitive way. Our algorithm supports users in designing materials with visualized small-scale details and maps them back to the large-scale appearance. Fig. 6.16 gives an example. Given a target material as input, our method can predict the meso-scale geometry and micro-scale BRDF, which can be used as a starting point for editing. We can let the appearance turn dimmer and duller by making the surface in the meso-scale rougher (Design 1), and increase its gloss and brightness by smoothing the surface (Design 2). Apart from adjusting the meso-scale geometry, we can also switch the micro-scale BRDF to change the appearance (Design 3). Fig. 6.17 demonstrates another example to design anisotropic materials from the isotropic ones. Given fabric materials on the left, our method predicts the woven thread structures and provides reconstructions in the middle. Using the prediction results, we can adjust the colors of different woven threads to generate anisotropic silk or fabric materials displayed on the right. Overall, our method provides a bi-scale design scheme that can help users intuitively edit materials to create a large variety of appearance.

The proposed tabular BRDF training can also be extended to solve analytical fitting problems. We provide a detailed implementation and compare the results with other analytical fitting solutions in the supplemental materials.

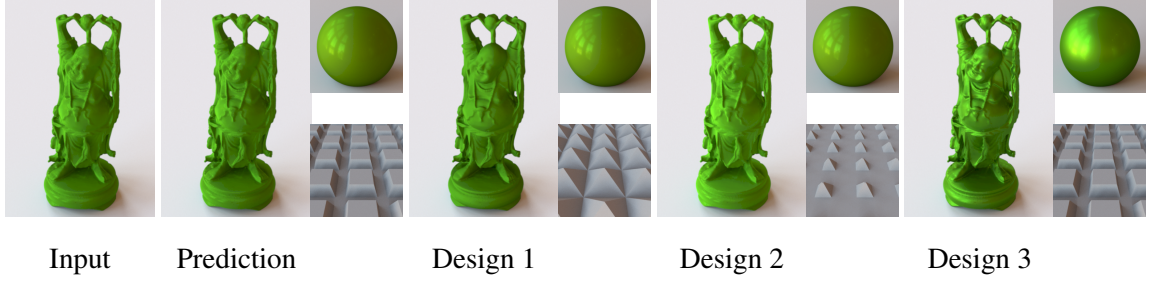


Figure 6.16: Bi-scale design example.

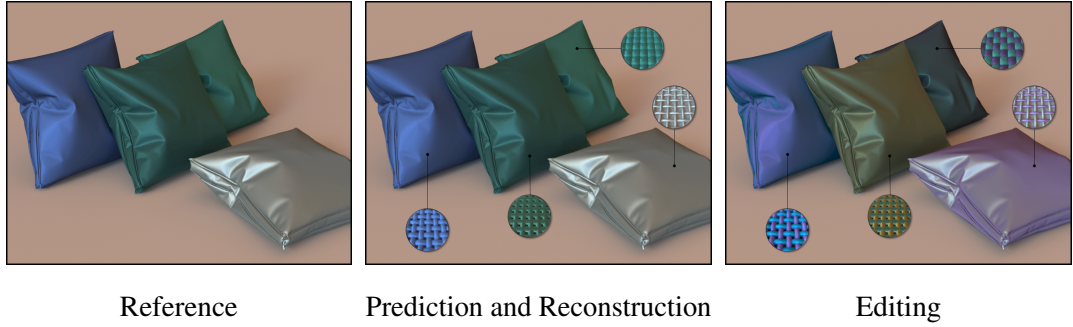


Figure 6.17: Bi-scale design for multi-color anisotropic materials.

6.6.2 Fabrication

The small-scale details obtained from our method could be used for material fabrication, and we show two woven examples in Fig. 6.18. Given a target appearance based on a fabric sample from real world, we first tabulate the BRDF and use our method to predict small-scale details. Then we render the prediction results and compare with real world sample in both scales. The same directional light and camera configurations are used to make it consistent between the rendering and photographs in large scale. Notice the inconsistency of shading for small scale is caused by the unknown lighting and camera setup of the close-up-view photographs. However, in terms of colors and structures, the predicted small-scale details largely match details of the woven fabric materials. Also considering large scale appearance, the reconstruction results are visually similar to the designed materials and the real world sample.

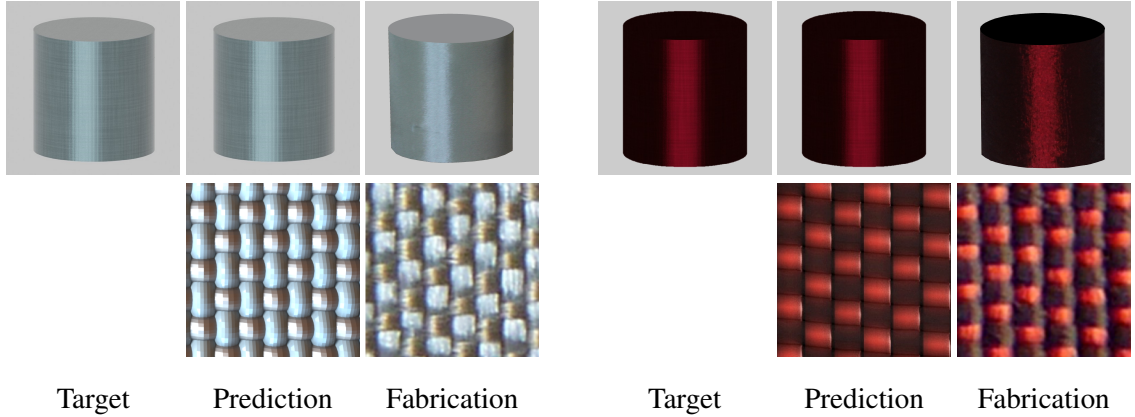


Figure 6.18: Fabrication example with target appearance modeled as a macro-BRDF for a given sample, the reconstruction using our method and small-scale details, and an image of the real world woven sample.

6.7 Discussion

Even with a larger fitting gamut, our bi-scale fitting model is still constrained by the diversity and complexity of training data, which could be solved by using alternative simulation methods. Fig. 6.19 shows a failure case. The reconstruction of material iris-purple-gem from the material library in Dupuy et al. [28] is less accurate due to the iridescent effect. Our simulation does not take into consideration the complex reflection effects like subsurface scattering and iridescent effects due to the limited computational power. We have experimented with alternative simulation solutions such as Wu et al. [156] to introduce inter-reflection, but the long precomputation time makes it impossible to simulate a large-scale training set like ours. As a trade-off, we use this relatively simple but efficient method and take different BRDF models or measured data into our training set to cover the larger fitting gamut. For future work, we could push the fitting gamut even further by introducing more diverse and complex materials or SVBRDF and find an efficient way to simulate materials with complex reflection effects.

Another limitation of our method is using a separate post-learning optimization to restore the material color. Although the optimization can produce anisotropy and multi-color at Fresnel angles, it is difficult to reconstruct the varying color in specular lobes, as demonstrated in Fig. 6.19. This is because the colors are assigned based on the facet groups of meso-scale geometry, which is not continuous and is low dimension. Furthermore, the local minimum of the optimization could also

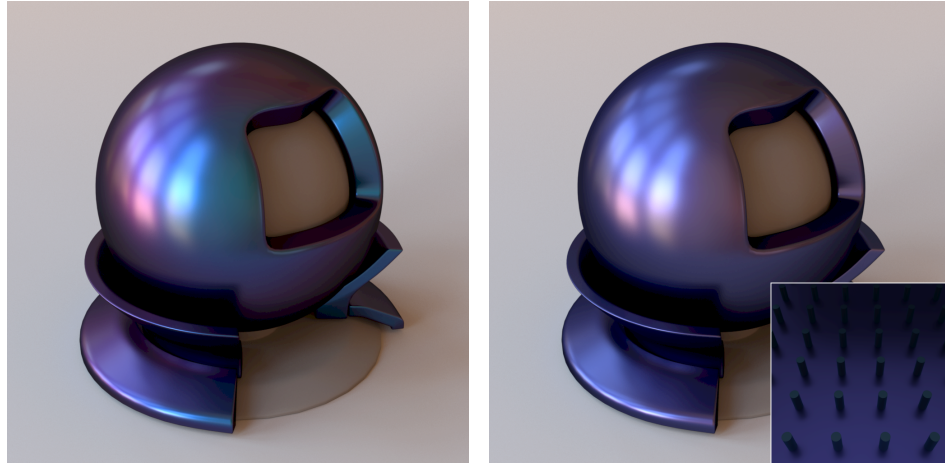
lead to the blending or averaging of the color of the ground truth. Ideally, given adequate computing resources, an end-to-end network that learns from chromatic data and fits colors as high dimension feature vectors would replace the optimization.

Moreover, although the focus of this chapter is BRDF fitting and acquisition is out of the scope, we want to mention that the macro-scale input to our model may not be easily acquired compared with an image or photograph with target appearance. Many existing solutions [57, 190] demonstrate the possibility to reconstruct full BRDFs using sparse samples from a given image.

Finally, we want to discuss how our method fits into the real world fabrication setting. To provide a larger fitting gamut and push the boundaries, we considered many cases in this chapter, such as using synthetic and measured BRDF for training and varying the color of different parts of the meso-scale geometry. Although for real life, only a limited palette of materials can be accessed, we do not consider this as a limitation. The key point of this chapter is to demonstrate the possibility of using a neural representation for material fitting, which releases the traditional constraints of using a single BRDF model with a limited gamut. In other words, the fitting gamut is now defined by the training data. Therefore, simple adjustments to our method can be considered to fit in the real-world scenarios, including using the available materials as training data since measured BRDF are supported, specifying the degree of freedom for colors and varying the meso-scale geometry that is available for fabrication. Although using the limited palette of materials for fitting may lead to lower reconstruction accuracy, a possibly close solution will be provided within the gamut for further iteration.

6.8 Conclusion

We present a learning-based solution to fit large-scale appearance using small-scale details, which provides a recipe for material design and fabrication. To accurately learn the properties from a given appearance, we introduce a new pipeline using tabular BRDF as a representation for training. Our method allows the network to directly learn the spatial features from tabular BRDFs without the bias of a particular context. Without redundant sampling for lighting and geometry, we can significantly reduce the required amount of training data and prevent overfitting to the rendering contexts. We demonstrated the effectiveness of our method by comparing with existing solutions and fitting real



Reference

Ours

Figure 6.19: Failure reconstruction of material example with iridescent effect.

world materials. We believe our method can be widely used for research in efficiently and accurately learning material appearances. We also believe our bi-scale network can be used for physically realizing virtually designed materials.

Chapter 7

Limitations, Future Work, and Conclusion

We have presented four different studies aimed at improving the accuracy and intuitiveness of material design and editing systems. Our work has included user studies of the human perception of material appearance, the creation of a perceptual parameter space, considerations of user interactions, and problems in physical realization. Our first work focuses on building a low-dimensional perceptual space for metal materials. We compute and analyze the perceptual embedding based on a large scale psychophysical user study and build an intuitive material editing interface using the proposed perceptual space. Our second work studies the relationship between glossiness and translucency in human perception. We conduct two experiments to study if subsurface scattering influences human perception of gloss and how the shape of the object contributes to this process. Our third work concentrates on user interaction in material editing. We design and implement an AR material design interface where users can edit materials in the real environment. We evaluate the user performance of the AR system by comparing it with the traditional material editing interface. With a target appearance, our final work uses a learning-based solution to map the large scale appearance to fabricatable meso-scale geometries. Our solution can accurately predict the recipe for the physical realization of the designed materials, which serves as the last step for the material design pipeline. In summary, the work in this dissertation focuses on improving material design and editing from different perspectives.

Our work has focused on understanding how humans visually perceive material appearance. We have also proposed practical algorithms and prototypes for accurate material design and editing. This dissertation has taken one step forward towards material recognition, interaction, and fabrication. We believe our work can inspire future research to further explore in these directions, and we hope our prototype systems can encourage more efforts to improve the experience of material editing applications. Here are possible future directions:

Multimodal Perception and User Interaction. Our work in this dissertation focus on improving material design system with visual perception. However, multi-sensory perception could significantly contribute to the design process. The AR material design system proposed in Chapter 5 is a first step to use human sensors beside visual perception in the appearance design process. One promising direction is to taking haptic perception into consideration. Humans can tell the difference between a rough surface and a smooth one by simply touching the material. Allowing users to touch and feel the materials could help them create the desired materials with a tactile impression. Eye-tracking is another direction that could improve the material design experience. We can use eye-tracking information to understand which part of the material users are most sensitive to during the design process. It can also help the material recommendation systems that allow users to choose from multiple available candidates, such as the image grid mentioned in Chapter 3. The eye-tracking system could help us understand users' preferences, which users themselves may not even notice.

Learning Based Material Editing. We have demonstrated how to use machine learning for bi-scale material editing in Chapter 6. There are many other material design applications that can benefit from machine learning techniques. Zsolnai-Fehér et al. have proposed to use machine learning for material recommendation [182]. Machine learning has also been used for switching materials between different objects and inpainting. However, robustly integrating machine learning techniques into interactive design applications is still a challenge problem. Collecting training data is the first problem that needs to be solved. The synthetic dataset is a possible solution for many research works that involve learning-based models. However, material editing may require large scale human-labeled data since it is based on human perception. Therefore, how to efficiently create the training data that can be used for perception tasks is still an open question. One possible direction would be exploring the idea of "self-learning", which combines the labeled and unlabeled perpetual data during the training process.

Material Fabrication with 3D Printing. We have proposed a solution in Chapter 6 to physically realize material appearance. However, it still could be challenging to fabricate materials with texture patterns because of the high dimensional input and limited resources to reconstruct complex appearances. Another promising direction is to combine the physical material design with the appearance design using the current 3D printing technologies. The physical properties of the available resource materials should be considered during the design process because they can significantly influence the fabrication results and make the solution more practical. However, this may come with the cost of more expertise and professional skills required. Therefore, an intuitive design system that involves resource material selection and management would help the designers to visualize target materials and put forward more practical fabrication solutions.

Looking back at all the projects from this dissertation, I realize there is much more to study to provide a user-friendly but also a powerful tool for material design and editing. The underlying visual processing of material appearance is complicated, and this definitely influences the behaviors when users have the power to edit an appearance. The goal of this dissertation is to understand this process first and then create a system that makes the editing process intuitive and efficient.

I believe the future of material design is relying on the development of VR/AR techniques and reliable recommendation systems thanks to machine learning techniques. The VR/AR techniques can enhance user experiences by triggering more sensors from a human. Although we have proposed an AR material design system in this dissertation, a more robust solution with advanced presentation techniques such as multi-projectors or VR goggles is still needed, especially for industrial purposes and product development. A reliable recommendation system that can recommend materials based on users' preferences and visual perception could push the design experience to another level. If a system can accurately predict the appearance a user wants to create based on his/her previous selections or descriptions, it would significantly reduce the time and energy of the trial-and-error process.

I acknowledge that any of the directions mentioned above would require a significantly huge amount of work. I think my dissertation provides a complete but still preliminary pipeline for the development of material design systems, and I do hope it could encourage more attention into this field.

Bibliography

- [1] W. B. Kerr and F. Pellacini. Toward evaluating material design interface paradigms for novice users. In *ACM Transactions on Graphics (TOG)*, volume 29, page 35. ACM, 2010.
- [2] Autodesk Inc. Maya 2017, 2017.
- [3] Blender Foundation . Blender, 2002.
- [4] J. Wills, S. Agarwal, D. Kriegman, and S. Belongie. Toward a perceptual space for gloss. *ACM Transactions on Graphics (TOG)*, 28(4):1–15, 2009.
- [5] F. Pellacini, J. A. Ferwerda, and D. P. Greenberg. Toward a psychophysically-based light reflection model for image synthesis. In *Proceedings of the 27th annual conference on Computer graphics and interactive techniques*, pages 55–64. ACM Press/Addison-Wesley Publishing Co., 2000.
- [6] H. B. Westlund and G. W. Meyer. Applying appearance standards to light reflection models. In *Proceedings of the 28th Annual Conference on Computer Graphics and Interactive Techniques, SIGGRAPH '01*, pages 501–51., New York, NY, USA, 2001. ACM.
- [7] A. Ngan, F. Durand, and W. Matusik. Experimental analysis of brdf models. *Rendering Techniques*, 2005(16th):2, 2005.
- [8] A. Fores, J. Ferwerda, and J. Gu. Toward a perceptually based metric for brdf modeling. In *Color and imaging conference*, volume 2012, pages 142–148. Society for Imaging Science and Technology, 2012.
- [9] J. Löw, J. Kronander, A. Ynnerman, and J. Unger. Brdf models for accurate and efficient rendering of glossy surfaces. *ACM Transactions on Graphics (TOG)*, 31(1):9, 2012.

- [10] M. M. Bagher, C. Soler, and N. Holzschuch. Accurate fitting of measured reflectances using a shifted gamma micro-facet distribution. In *Computer Graphics Forum*, volume 31, pages 1509–1518. Wiley Online Library, 2012.
- [11] M. M. Bagher, J. Snyder, and D. Nowrouzezahrai. A non-parametric factor microfacet model for isotropic brdfs. *ACM Transactions on Graphics (TOG)*, 35(5):159, 2016.
- [12] A. Brady, J. Lawrence, P. Peers, and W. Weimer. genbrdf: discovering new analytic brdfs with genetic programming. *ACM Transactions on Graphics (TOG)*, 33(4):114, 2014.
- [13] T. Sun, H. W. Jensen, and R. Ramamoorthi. Connecting measured brdfs to analytic brdfs by data-driven diffuse-specular separation. In *SIGGRAPH Asia 2018 Technical Papers*, page 273. ACM, 2018.
- [14] H. Wu, J. Dorsey, and H. Rushmeier. Inverse bi-scale material design. *ACM Transactions on Graphics (TOG)*, 32(6):163, 2013.
- [15] W. Shi, J. Dorsey, and H. Rushmeier. Learning-based inverse bi-scale material fitting from tabular brdfs. *IEEE Transactions on Visualization and Computer Graphics*, 2020.
- [16] W. Shi, Z. Wang, M. Sezgin, J. Dorsey, and H. Rushmeier. Material design in augmented reality with in-situ visual feedback. In *Proceedings of the Eurographics Symposium on Rendering: Experimental Ideas & Implementations*, pages 93–103, 2017.
- [17] E. Davis, W. Shi, H. Rushmeier, J. Dorsey, and H. Wu. Image-based brdf design. *Electronic Imaging*, 2019(6):482–1, 2019.
- [18] J. T. Kajiya. The rendering equation. In *Proceedings of the 13th annual conference on Computer graphics and interactive techniques*, pages 143–150, 1986.
- [19] S. Chandrasekhar. *Radiative transfer*. Courier Corporation, 2013.
- [20] G. J. Ward. Measuring and modeling anisotropic reflection. In *Proceedings of the 19th Annual Conference on Computer Graphics and Interactive Techniques*, pages 265–272, 1992.
- [21] B. Walter. Notes on the ward brdf. *Program of Computer Graphics, Cornell University, Technical report PCG-05*, 6, 2005.

- [22] B. T. Phong. Illumination for computer generated pictures. *Communications of the ACM*, 18(6):311–317, 1975.
- [23] M. Oren and S. K. Nayar. Generalization of lambert’s reflectance model. In *Proceedings of the 21st annual conference on Computer graphics and interactive techniques*, pages 239–246. ACM, 1994.
- [24] J. F. Blinn. Models of light reflection for computer synthesized pictures. In *Proceedings of the 4th annual conference on Computer graphics and interactive techniques*, pages 192–198, 1977.
- [25] K. E. Torrance and E. M. Sparrow. Theory for off-specular reflection from roughened surfaces. *Josa*, 57(9):1105–1114, 1967.
- [26] W. Matusik, H. Pfister, M. Brand, and L. McMillan. A data-driven reflectance model. *ACM Transactions on Graphics*, July 2003.
- [27] S. M. Rusinkiewicz. A new change of variables for efficient BRDF representation. In *Eurographics Workshop on Rendering Techniques*, pages 11–22. Springer, 1998.
- [28] J. Dupuy and W. Jakob. An adaptive parameterization for efficient material acquisition and rendering. In *SIGGRAPH Asia 2018 Technical Papers*, page 274. ACM, 2018.
- [29] A. Serrano, D. Gutierrez, K. Myszkowski, H.-P. Seidel, and B. Masia. An intuitive control space for material appearance. *ACM Transactions on Graphics (SIGGRAPH ASIA 2016)*, 35(6), 2016.
- [30] I. Gkioulekas, B. Xiao, S. Zhao, E. H. Adelson, T. Zickler, and K. Bala. Understanding the role of phase function in translucent appearance. *ACM Transactions on graphics (TOG)*, 32(5):1–19, 2013.
- [31] R. W. Fleming and H. H. Bühlhoff. Low-level image cues in the perception of translucent materials. *ACM Transactions on Applied Perception (TAP)*, 2(3):346–382, 2005.
- [32] C. Soler, K. Subr, and D. Nowrouzezahrai. A versatile parameterization for measured material

- manifolds. In *Computer graphics forum*, volume 37, pages 135–144. Wiley Online Library, 2018.
- [33] O. Tamuz, C. Liu, S. Belongie, O. Shamir, and A. T. Kalai. Adaptively learning the crowd kernel. *arXiv preprint arXiv:1105.1033*, 2011.
 - [34] M. Lagunas, S. Malpica, A. Serrano, E. Garces, D. Gutierrez, and B. Masia. A similarity measure for material appearance. *ACM Transactions on Graphics (SIGGRAPH 2019)*, 38(4), 2019.
 - [35] J. Dorsey, H. Rushmeier, and F. Sillion. *Digital modeling of material appearance*. Elsevier, 2010.
 - [36] B. L. Anderson. Visual perception of materials and surfaces. *Current biology*, 21(24):R978–R983, 2011.
 - [37] R. W. Fleming. Visual perception of materials and their properties. *Vision research*, 94:62–75, 2014.
 - [38] R. W. Fleming, S. Nishida, and K. R. Gegenfurtner. Perception of material properties. 2015.
 - [39] L. T. Maloney and D. H. Brainard. Color and material perception: Achievements and challenges. *Journal of vision*, 10(9):19–19, 2010.
 - [40] A. C. Chadwick and R. Kentridge. The perception of gloss: A review. *Vision research*, 109:221–235, 2015.
 - [41] I. Gkioulekas, B. Walter, E. H. Adelson, K. Bala, and T. Zickler. On the appearance of translucent edges. In *Proceedings of the IEEE Conference on Computer Vision and Pattern Recognition*, pages 5528–5536, 2015.
 - [42] D. Gigilashvili, J.-B. Thomas, J. Y. Hardeberg, and M. Pedersen. Behavioral investigation of visual appearance assessment. In *Color and Imaging Conference*, number 1, pages 294–299. Society for Imaging Science and Technology, 2018.

- [43] D. Gigilashvili, P. Urban, J.-B. Thomas, J. Y. Hardeberg, and M. Pedersen. Impact of shape on apparent translucency differences. In *Color and Imaging Conference*, pages 132–137. Society for Imaging Science and Technology, 2019.
- [44] T. Leung and J. Malik. Representing and recognizing the visual appearance of materials using three-dimensional textons. *International journal of computer vision*, 43(1):29–44, 2001.
- [45] J. J. R. Van Assen, P. Barla, and R. W. Fleming. Visual features in the perception of liquids. *Current biology*, 28(3):452–458, 2018.
- [46] V. Havran, J. Filip, and K. Myszkowski. Perceptually motivated brdf comparison using single image. In *Computer graphics forum*, volume 35, pages 1–12. Wiley Online Library, 2016.
- [47] P. Vangorp, J. Laurijssen, and P. Dutré. The influence of shape on the perception of material reflectance. In *ACM SIGGRAPH 2007 papers*, pages 77–es. 2007.
- [48] Y.-X. Ho, M. S. Landy, and L. T. Maloney. How direction of illumination affects visually perceived surface roughness. *Journal of vision*, 6(5):8–8, 2006.
- [49] P. Vangorp, P. Barla, and R. W. Fleming. The perception of hazy gloss. *Journal of vision*, 17(5):19–19, 2017.
- [50] J. Křivánek, J. A. Ferwerda, and K. Bala. Effects of global illumination approximations on material appearance. *ACM Transactions on Graphics (TOG)*, 29(4):1–10, 2010.
- [51] K. Doerschner, R. W. Fleming, O. Yilmaz, P. R. Schrater, B. Hartung, and D. Kersten. Visual motion and the perception of surface material. *Current biology*, 21(23):2010–2016, 2011.
- [52] A. Ngan, F. Durand, and W. Matusik. Image-driven navigation of analytical brdf models. *Rendering Techniques*, 2006:399–407, 2006.
- [53] T. Pereira and S. Rusinkiewicz. Gamut mapping spatially varying reflectance with an improved brdf similarity metric. In *Computer graphics forum*, volume 31, pages 1557–1566. Wiley Online Library, 2012.

- [54] T. Sun, A. Serrano, D. Gutierrez, and B. Masia. Attribute-preserving gamut mapping of measured brdfs. In *Computer graphics forum*, volume 36, pages 47–54. Wiley Online Library, 2017.
- [55] S. H. Westin, J. R. Arvo, and K. E. Torrance. Predicting reflectance functions from complex surfaces. In *Proceedings of the 19th annual conference on Computer graphics and interactive techniques*, pages 255–264, 1992.
- [56] P. Schröder and W. Sweldens. Spherical wavelets: Efficiently representing functions on the sphere. In *Proceedings of the 22nd annual conference on Computer graphics and interactive techniques*, pages 161–172, 1995.
- [57] J. B. Nielsen, H. W. Jensen, and R. Ramamoorthi. On optimal, minimal brdf sampling for reflectance acquisition. *ACM Transactions on Graphics (TOG)*, 34(6):186, 2015.
- [58] M. Colbert, S. Pattanaik, and J. Krivanek. Brdf-shop: Creating physically correct bidirectional reflectance distribution functions. *IEEE Computer Graphics and Applications*, 26(1):30–36, 2006.
- [59] V. Koltun. Exploratory modeling with collaborative design spaces. 2009.
- [60] C. H. Nguyen, M.-H. Kyung, J.-H. Lee, and S.-W. Nam. A pca decomposition for real-time brdf editing and relighting with global illumination. In *Computer Graphics Forum*, volume 29, pages 1469–1478. Wiley Online Library, 2010.
- [61] E. Cheslack-Postava, R. Wang, O. Akerlund, and F. Pellacini. Fast, realistic lighting and material design using nonlinear cut approximation. *ACM Transactions on Graphics (TOG)*, 27(5):1–10, 2008.
- [62] X. Sun, K. Zhou, Y. Chen, S. Lin, J. Shi, and B. Guo. Interactive relighting with dynamic brdfs. In *ACM SIGGRAPH 2007 papers*, pages 27–es. 2007.
- [63] I. Boyadzhiev, K. Bala, S. Paris, and E. Adelson. Band-sifting decomposition for image-based material editing. *ACM Transactions on Graphics (TOG)*, 34(5):1–16, 2015.

- [64] M. Mylo, M. Giesel, Q. Zaidi, M. Hullin, and R. Klein. Appearance bending: A perceptual editing paradigm for data-driven material models. In *Proceedings of the conference on Vision, Modeling and Visualization*, pages 9–16, 2017.
- [65] J. Marks, B. Andalman, P. A. Beardsley, W. Freeman, S. Gibson, J. Hodgins, T. Kang, B. Mirtich, H. Pfister, W. Ruml, K. Ryall, J. Seims, and S. Shieber. Design galleries: A general approach to setting parameters for computer graphics and animation. In *Proceedings of the 24th Annual Conference on Computer Graphics and Interactive Techniques, SIGGRAPH '97*, pages 389–400, New York, NY, USA, 1997. ACM Press/Addison-Wesley Publishing Co.
- [66] ADOBE SYSTEMS INC . Photoshop cs 4, 2009.
- [67] R. W. Fleming, R. O. Dror, and E. H. Adelson. Real-world illumination and the perception of surface reflectance properties. *Journal of vision*, 3(5):3–3, 2003.
- [68] W. Jakob. Mitsuba renderer, 2010. <http://www.mitsuba-renderer.org>.
- [69] S. Agarwal, J. Wills, L. Cayton, G. Lanckriet, D. Kriegman, and S. Belongie. Generalized non-metric multidimensional scaling. In *Artificial Intelligence and Statistics*, pages 11–18, 2007.
- [70] J. F. Sturm. Using sedumi 1.02, a matlab toolbox for optimization over symmetric cones. *Optimization methods and software*, 11(1-4):625–653, 1999.
- [71] C. E. Rasmussen. Gaussian processes in machine learning. In *Summer School on Machine Learning*, pages 63–71. Springer, 2003.
- [72] B. Burley and W. D. A. Studios. Physically-based shading at disney. In *ACM SIGGRAPH*, volume 2012, pages 1–7. vol. 2012, 2012.
- [73] E. H. Adelson. On seeing stuff: the perception of materials by humans and machines. In *Human vision and electronic imaging VI*, volume 4299, pages 1–12. International Society for Optics and Photonics, 2001.
- [74] L. Sharan, R. Rosenholtz, and E. H. Adelson. Accuracy and speed of material categorization in real-world images. *Journal of vision*, 14(9):12–12, 2014.

- [75] Z. Pizlo. Perception viewed as an inverse problem. *Vision research*, 41(24):3145–3161, 2001.
- [76] I. Motoyoshi, S. Nishida, L. Sharan, and E. H. Adelson. Image statistics and the perception of surface qualities. *Nature*, 447(7141):206–209, 2007.
- [77] J. Kim, P. Marlow, and B. L. Anderson. The perception of gloss depends on highlight congruence with surface shading. *Journal of Vision*, 11(9)(4):1–19, 2011.
- [78] C. Eugène. Measurement of "total visual appearance": a CIE challenge of soft metrology. In *12th IMEKO TC1 & TC7 Joint Symposium on Man, Science & Measurement*, pages 61–65, 2008.
- [79] D. Gigilashvili, J.-B. Thomas, M. Pedersen, and J. Y. Hardeberg. Material appearance: ordering and clustering. In *Material Appearance 2019, IS&T International Symposium on Electronic Imaging*, pages 202:1–202:6. Society for Imaging Science and Technology, 2019.
- [80] D. Gigilashvili, J.-B. Thomas, M. Pedersen, and J. Y. Hardeberg. Perceived glossiness: Beyond surface properties. In *Color and Imaging Conference*, number 1, pages 37–42. Society for Imaging Science and Technology, 2019.
- [81] ASTM. ASTM E284-17 standard terminology of appearance. ASTM International, West Conshohocken, PA, 2017.
- [82] R. S. Hunter. Methods of determining gloss. *NBS Research paper RP*, 958, 1937.
- [83] J.-B. Thomas, J. Y. Hardeberg, and G. Simone. Image contrast measure as a gloss material descriptor. In *International Workshop on Computational Color Imaging*, pages 233–245. Springer, 2017.
- [84] P. J. Marlow, J. Kim, and B. L. Anderson. The perception and misperception of specular surface reflectance. *Current Biology*, 22(20):1909–1913, 2012.
- [85] P. J. Marlow and B. L. Anderson. Generative constraints on image cues for perceived gloss. *Journal of Vision*, 13(14:2):1–23, 2013.
- [86] L. Qi, M. J. Chantler, J. P. Siebert, and J. Dong. Why do rough surfaces appear glossy? *Journal of the Optical Society of America A*, 31(5):935–943, 2014.

- [87] L. Qi, M. J. Chantler, J. P. Siebert, and J. Dong. The joint effect of mesoscale and microscale roughness on perceived gloss. *Vision Research*, 115:209–217, 2015.
- [88] G. Obein, K. Knoblauch, and F. Viénot. Difference scaling of gloss: Nonlinearity, binocularity, and constancy. *Journal of vision*, 4:711–720, 2004.
- [89] G. Wendt, F. Faul, V. Ekroll, and R. Mausfeld. Disparity, motion, and color information improve gloss constancy performance. *Journal of Vision*, 10(9)(7):1–17, 2010.
- [90] M. W. Wijntjes and S. C. Pont. Illusory gloss on lambertian surfaces. *Journal of Vision*, 10(9:13):1–12, 2010.
- [91] M. Toscani, D. Guarnera, G. C. Guarnera, J. Y. Hardeberg, and K. R. Gegenfurtner. Three perceptual dimensions for specular and diffuse reflection. *ACM Transactions on Applied Perception (TAP)*, 17(2):1–26, 2020.
- [92] J. Beck and S. Prazdny. Highlights and the perception of glossiness. *Perception & Psychophysics*, 1981.
- [93] I. S. Kerrigan and W. J. Adams. Highlights, disparity, and perceived gloss with convex and concave surfaces. *Journal of Vision*, 13(1:9):1–10, 2013.
- [94] A. C. Schmid, P. Barla, and K. Doerschner. Material category determined by specular reflection structure mediates the processing of image features for perceived gloss. *bioRxiv*, 2020. bioRxiv preprint DOI: <https://doi.org/10.1101/2019.12.31.892083>.
- [95] M. S. Landy. A gloss on surface properties. *Nature*, 447(7141):158–159, 2007.
- [96] D. Gigilashvili, M. Tanaka, M. Pedersen, and J. Y. Hardeberg. Image statistics as glossiness and translucency predictor in photographs of real-world objects. In *10th Colour and Visual Computing Symposium (CVCS)*, page 15 pages. CEUR Workshop Proceedings, 2020.
- [97] B. L. Anderson and J. Kim. Image statistics do not explain the perception of gloss and lightness. *Journal of Vision*, 9(11:10):1–17, 2009.
- [98] P. Marlow, J. Kim, and B. L. Anderson. The role of brightness and orientation congruence in the perception of surface gloss. *Journal of Vision*, 11(9)(16):1–12, 2011.

- [99] M. Olkkonen and D. H. Brainard. Joint effects of illumination geometry and object shape in the perception of surface reflectance. *i-Perception*, 2(9):1014–1034, 2011.
- [100] L. Qi, M. J. Chantler, J. P. Siebert, and J. Dong. How mesoscale and microscale roughness affect perceived gloss. In *Predicting Perceptions: Proceedings of the 3rd International Conference on Appearance*, pages 48–51. Lulu Press, Inc. Edinburgh, Scotland, 2012.
- [101] Y. Sakano and H. Ando. Effects of head motion and stereo viewing on perceived glossiness. *Journal of Vision*, 10(9)(15):1–14, 2010.
- [102] S. Nishida, I. Motoyoshi, L. Nakano, Y. Li, L. Sharan, and E. Adelson. Do colored highlights look like highlights? *Journal of Vision*, 8(6):339, 2008.
- [103] A. C. Chadwick, G. Cox, H. E. Smithson, and R. W. Kentridge. Beyond scattering and absorption: Perceptual unmixing of translucent liquids. *Journal of vision*, 18(11:18):1–15, 2018.
- [104] B. Xiao, S. Zhao, I. Gkioulekas, W. Bi, and K. Bala. Effect of geometric sharpness on translucent material perception. *bioRxiv*, page 795294, 2019.
- [105] N. S. Chowdhury, P. J. Marlow, and J. Kim. Translucency and the perception of shape. *Journal of vision*, 17(3:17):1–14, 2017.
- [106] M. Sawayama, Y. Dobashi, M. Okabe, K. Hosokawa, T. Koumura, T. Saarela, M. Olkkonen, and S. Nishida. Visual discrimination of optical material properties: a large-scale study. *BioRxiv*, page 800870, 2019.
- [107] T. Nagai, Y. Ono, Y. Tani, K. Koida, M. Kitazaki, and S. Nakauchi. Image regions contributing to perceptual translucency: A psychophysical reverse-correlation study. *i-Perception*, 4(6):407–428, 2013.
- [108] B. Xiao, B. Walter, I. Gkioulekas, T. Zickler, E. Adelson, and K. Bala. Looking against the light: How perception of translucency depends on lighting direction. *Journal of Vision*, 14(3:17):1–22, 2014.

- [109] D. Gigilashvili, F. Mirjalili, and J. Y. Hardeberg. Illuminance impacts opacity perception of textile materials. In *Color and Imaging Conference*, pages 126–131. Society for Imaging Science and Technology, 2019.
- [110] B. Xiao and D. H. Brainard. Surface gloss and color perception of 3d objects. *Visual neuroscience*, 25(3):371–385, 2008.
- [111] mfa Boston CAMEO. Paraffin wax. http://cameo.mfa.org/wiki/Paraffin_wax, 2020. Accessed on 25.08.2020.
- [112] Scientific Polymer Products, Inc. Refractive index of polymers. <https://scientificpolymer.com/technical-library/refractive-index-of-polymers-by-index/>, 2020. Accessed on 25.08.2020.
- [113] B. J. Frey and D. Dueck. Clustering by passing messages between data points. *Science*, 315(5814):972–976, 2007.
- [114] S. Holm. A simple sequentially rejective multiple test procedure. *Scandinavian journal of statistics*, pages 65–70, 1979.
- [115] P. G. Engeldrum. *Psychometric scaling: a toolkit for imaging systems development*. Imcotek, 2000.
- [116] K. Tsukida and M. R. Gupta. How to analyze paired comparison data. Technical report, University of Washington, Department of Electrical Engineering, Seattle, WA, 2011.
- [117] L. L. Thurstone. A law of comparative judgment. *Psychological review*, 34(4):273–286, 1927.
- [118] P. J. Green. A colour engineering toolbox. <http://www.color.org/resources/ColourEngineeringToolbox.zip>, 2003. Accessed on 25.08.2020.
- [119] R. L. Rosnow and R. Rosenthal. Effect sizes for experimenting psychologists. *Canadian Journal of Experimental Psychology/Revue canadienne de psychologie expérimentale*, 57(3):221, 2003.
- [120] J. Cohen. *Statistical power analysis for the behavioral sciences (2nd ed.)*. Hillsdale, NJ: Erlbaum., 1988.

- [121] Y.-X. Ho, M. S. Landy, and L. T. Maloney. Conjoint measurement of gloss and surface texture. *Psychological Science*, 19(2):196–204, 2008.
- [122] M. Meyer, M. Desbrun, P. Schröder, and A. H. Barr. Discrete differential-geometry operators for triangulated 2-manifolds. In *Visualization and mathematics III*, pages 35–57. Springer, 2003.
- [123] A. Dastan. Gaussian and mean curvatures calculation on a triangulated 3d surface. <https://www.mathworks.com/matlabcentral/fileexchange/61136-gaussian-and-mean-curvatures-calculation-on-a-triangulated-3d-surface>, 2020. Retrieved: 2020-07-30 from MATLAB Central File Exchange.
- [124] R. Azuma, Y. Baillot, R. Behringer, S. Feiner, S. Julier, and B. MacIntyre. Recent advances in augmented reality. *IEEE computer graphics and applications*, 21(6):34–47, 2001.
- [125] W. B. Kerr and F. Pellacini. Toward evaluating lighting design interface paradigms for novice users. In *ACM SIGGRAPH 2009 Papers*, SIGGRAPH '09, pages 26:1–26:9, New York, NY, USA, 2009. ACM.
- [126] R. Raskar, K. Low, and G. Welch. Shader lamps: Animating real objects with image-based illumination. Technical report, Chapel Hill, NC, USA, 2000.
- [127] D. G. Aliaga, Y. H. Yeung, A. Law, B. Sajadi, and A. Majumder. Fast high-resolution appearance editing using superimposed projections. *ACM Trans. Graph.*, 31(2):13:1–13:13, April 2012.
- [128] L. Miyashita, K. Ishihara, Y. Watanabe, and M. Ishikawa. Zoematrope: A system for physical material design. *ACM Trans. Graph.*, 35(4):66:1–66:11, July 2016.
- [129] Dynamic shader lamps: Painting on movable objects. In *Proceedings of the IEEE and ACM International Symposium on Augmented Reality (ISAR'01)*, ISAR '01, pages 207–, Washington, DC, USA, 2001. IEEE Computer Society.
- [130] M. B. Hullin, I. Ihrke, W. Heidrich, T. Weyrich, G. Damberg, and M. Fuchs. Computational Fabrication and Display of Material Appearance. In M. Sbert and L. Szirmay-Kalos, editors, *Eurographics 2013 - State of the Art Reports*. The Eurographics Association, 2013.

- [131] R. Ramamoorthi and P. Hanrahan. An efficient representation for irradiance environment maps. In *Proceedings of the 28th annual conference on Computer graphics and interactive techniques*, pages 497–500. ACM, 2001.
- [132] M. Knecht, C. Traxler, O. Mattausch, W. Purgathofer, and M. Wimmer. Differential instant radiosity for mixed reality. In *Mixed and Augmented Reality (ISMAR), 2010 9th IEEE International Symposium on*, pages 99–107. IEEE, 2010.
- [133] T. Grosch, T. Eble, and S. Mueller. Consistent interactive augmentation of live camera images with correct near-field illumination. In *Proceedings of the 2007 ACM symposium on Virtual reality software and technology*, pages 125–132. ACM, 2007.
- [134] K. Karsch, V. Hedau, D. Forsyth, and D. Hoiem. Rendering synthetic objects into legacy photographs. In *ACM Transactions on Graphics (TOG)*, volume 30, page 157. ACM, 2011.
- [135] P. Debevec. Rendering synthetic objects into real scenes: Bridging traditional and image-based graphics with global illumination and high dynamic range photography. In *ACM SIGGRAPH 2008 classes*, page 32. ACM, 2008.
- [136] P. Kán and H. Kaufmann. High-quality reflections, refractions, and caustics in augmented reality and their contribution to visual coherence. In *Mixed and Augmented Reality (ISMAR), 2012 IEEE International Symposium on*, pages 99–108. IEEE, 2012.
- [137] P. Lensing and W. Broll. Instant indirect illumination for dynamic mixed reality scenes. In *Mixed and Augmented Reality (ISMAR), 2012 IEEE International Symposium on*, pages 109–118. IEEE, 2012.
- [138] C. Dachsbacher and M. Stamminger. Reflective shadow maps. In *Proceedings of the 2005 symposium on Interactive 3D graphics and games*, pages 203–231. ACM, 2005.
- [139] G. Greger, P. Shirley, P. M. Hubbard, and D. P. Greenberg. The irradiance volume. *IEEE Computer Graphics and Applications*, 18(2):32–43, 1998.
- [140] G. J. Ward, F. M. Rubinstein, and R. D. Clear. A ray tracing solution for diffuse interreflection. *ACM SIGGRAPH Computer Graphics*, 22(4):85–92, 1988.

- [141] J. Krivánek, K. Bouatouch, S. N. Pattanaik, and J. Zara. Making radiance and irradiance caching practical: Adaptive caching and neighbor clamping. *Rendering Techniques*, 2006:127–138, 2006.
- [142] J. Schwarzhaupt, H. W. Jensen, and W. Jarosz. Practical hessian-based error control for irradiance caching. *ACM Transactions on Graphics (TOG)*, 31(6):193, 2012.
- [143] W. Jarosz, V. Schöenefeld, L. Kobbelt, and H. W. Jensen. Theory, analysis and applications of 2d global illumination. *ACM Transactions on Graphics (TOG)*, 31(5):125, 2012.
- [144] P. Kán and H. Kaufmann. Differential irradiance caching for fast high-quality light transport between virtual and real worlds. In *Mixed and Augmented Reality (ISMAR), 2013 IEEE International Symposium on*, pages 133–141. IEEE, 2013.
- [145] S. G. Parker, J. Bigler, A. Dietrich, H. Friedrich, J. Hoberock, D. Luebke, D. McAllister, M. McGuire, K. Morley, A. Robison, et al. Optix: a general purpose ray tracing engine. In *ACM Transactions on Graphics (TOG)*, volume 29, page 66. ACM, 2010.
- [146] H. Kato and M. Billinghurst. Marker tracking and hmd calibration for a video-based augmented reality conferencing system. In *Augmented Reality, 1999.(IWAR’99) Proceedings. 2nd IEEE and ACM International Workshop on*, pages 85–94. IEEE, 1999.
- [147] J. P. Stevens. *Applied multivariate statistics for the social sciences*. Routledge, 2012.
- [148] R. W. Fleming. Material perception. *Annual review of vision science*, 3:365–388, 2017.
- [149] S. K. Shukla and A. Kumanan. Durability of customer perceived quality of molded-in-color car bumper. Technical report, SAE Technical Paper, 2019.
- [150] Wisconsin. Wisconsin engraving. <http://www.wi-engraving.com/>, 2019.
- [151] S. Paul. St. paul engraving. <http://www.stpaulengraving.com>, 2019.
- [152] O. Rouiller, B. Bickel, J. Kautz, W. Matusik, and M. Alexa. 3d-printing spatially varying brdfs. *IEEE computer graphics and applications*, 33(6):48–57, 2013.
- [153] T. Weyrich, P. Peers, W. Matusik, and S. Rusinkiewicz. Fabricating microgeometry for custom surface reflectance. *ACM Transactions on Graphics (TOG)*, 28(3):32, 2009.

- [154] S. Zhao, W. Jakob, S. Marschner, and K. Bala. Structure-aware synthesis for predictive woven fabric appearance. *ACM Transactions on Graphics (TOG)*, 31(4):75, 2012.
- [155] Y. Lan, Y. Dong, F. Pellacini, and X. Tong. Bi-scale appearance fabrication. *ACM Trans. Graph.*, 32(4):145–1, 2013.
- [156] L. Wu, S. Zhao, L.-Q. Yan, and R. Ramamoorthi. Accurate appearance preserving prefiltering for rendering displacement-mapped surfaces. *ACM Transactions on Graphics (TOG)*, 38(4):137, 2019.
- [157] H. Wu, J. Dorsey, and H. Rushmeier. Physically-based interactive bi-scale material design. *ACM Transactions on Graphics (TOG)*, 30(6):145, 2011.
- [158] M. Ashikmin, S. Premože, and P. Shirley. A microfacet-based brdf generator. In *Proceedings of the 27th annual conference on Computer graphics and interactive techniques*, pages 65–74. ACM Press/Addison-Wesley Publishing Co., 2000.
- [159] R. L. Cook and K. E. Torrance. A reflectance model for computer graphics. *ACM Transactions on Graphics (TOG)*, 1(1):7–24, 1982.
- [160] B. Walter, S. R. Marschner, H. Li, and K. E. Torrance. Microfacet models for refraction through rough surfaces. In *Proceedings of the 18th Eurographics conference on Rendering Techniques*, pages 195–206. Eurographics Association, 2007.
- [161] E. Heitz. Understanding the masking-shadowing function in microfacet-based brdfs. *Journal of Computer Graphics Techniques*, 3(2):32–91, 2014.
- [162] E. Heitz, J. Hanika, E. d’Eon, and C. Dachsbacher. Multiple-scattering microfacet bsdfs with the smith model. *ACM Transactions on Graphics (TOG)*, 35(4):58, 2016.
- [163] N. Holzschuch and R. Pacanowski. A two-scale microfacet reflectance model combining reflection and diffraction. *ACM Transactions on Graphics (TOG)*, 36(4):66, 2017.
- [164] C. Aliaga, C. Castillo, D. Gutierrez, M. A. Otaduy, J. Lopez-Moreno, and A. Jarabo. An appearance model for textile fibers. In *Computer Graphics Forum*, volume 36, pages 35–45. Wiley Online Library, 2017.

- [165] Z. Dong, B. Walter, S. Marschner, and D. P. Greenberg. Predicting appearance from measured microgeometry of metal surfaces. *ACM Transactions on Graphics (TOG)*, 35(1):9, 2015.
- [166] G. Nam, J. H. Lee, H. Wu, D. Gutierrez, and M. H. Kim. Simultaneous acquisition of microscale reflectance and normals. *ACM Trans. Graph.*, 35(6):185–1, 2016.
- [167] L. Belcour and P. Barla. A practical extension to microfacet theory for the modeling of varying iridescence. *ACM Transactions on Graphics (TOG)*, 36(4):65, 2017.
- [168] J. Dupuy, E. Heitz, J.-C. Iehl, P. Poulin, and V. Ostromoukhov. Extracting microfacet-based brdf parameters from arbitrary materials with power iterations. In *Computer Graphics Forum*, volume 34, pages 21–30. Wiley Online Library, 2015.
- [169] S. Zhao, W. Jakob, S. Marschner, and K. Bala. Building volumetric appearance models of fabric using micro ct imaging. *ACM Transactions on Graphics (TOG)*, 30(4):44, 2011.
- [170] W. Heidrich, K. Daubert, J. Kautz, and H.-P. Seidel. Illuminating micro geometry based on precomputed visibility. In *Proceedings of the 27th annual conference on Computer graphics and interactive techniques*, pages 455–464. ACM Press/Addison-Wesley Publishing Co., 2000.
- [171] A. Kuznetsov, M. Hašan, Z. Xu, L.-Q. Yan, B. Walter, N. K. Kalantari, S. Marschner, and R. Ramamoorthi. Learning generative models for rendering specular microgeometry. *ACM Transactions on Graphics (TOG)*, 38(6):225, 2019.
- [172] W. Li and M. Fritz. Recognizing materials from virtual examples. In *European Conference on Computer Vision*, pages 345–358. Springer, 2012.
- [173] F. Romeiro and T. Zickler. Blind reflectometry. In *European conference on computer vision*, pages 45–58. Springer, 2010.
- [174] R. Vidaurre, D. Casas, E. Garces, and J. Lopez-Moreno. Brdf estimation of complex materials with nested learning. In *2019 IEEE Winter Conference on Applications of Computer Vision (WACV)*, pages 1347–1356. IEEE, 2019.
- [175] H. Liu and F. Sun. Material identification using tactile perception: A semantics-regularized

- p dictionary learning method.
- IEEE/ASME Transactions on Mechatronics*
- , 23(3):1050–1058, 2017.
- [176] C. Innamorati, T. Ritschel, T. Weyrich, and N. J. Mitra. Decomposing single images for layered photo retouching. In *Computer Graphics Forum*, volume 36, pages 15–25. Wiley Online Library, 2017.
 - [177] Y. Yu and W. A. Smith. Pvnn: A neural network library for photometric vision. In *Proceedings of the IEEE International Conference on Computer Vision*, pages 526–535, 2017.
 - [178] S. Georgoulis, K. Rematas, T. Ritschel, E. Gavves, M. Fritz, L. Van Gool, and T. Tuytelaars. Reflectance and natural illumination from single-material specular objects using deep learning. *IEEE transactions on pattern analysis and machine intelligence*, 40(8):1932–1947, 2018.
 - [179] A. Meka, M. Maximov, M. Zollhoefer, A. Chatterjee, H.-P. Seidel, C. Richardt, and C. Theobalt. Lime: Live intrinsic material estimation. In *Proceedings of the IEEE Conference on Computer Vision and Pattern Recognition*, pages 6315–6324, 2018.
 - [180] K. Kim, J. Gu, S. Tyree, P. Molchanov, M. Nießner, and J. Kautz. A lightweight approach for on-the-fly reflectance estimation. In *Proceedings of the IEEE International Conference on Computer Vision*, pages 20–28, 2017.
 - [181] X. Li, Y. Dong, P. Peers, and X. Tong. Modeling surface appearance from a single photograph using self-augmented convolutional neural networks. *ACM Transactions on Graphics (TOG)*, 36(4):45, 2017.
 - [182] K. Zsolnai-Fehér, P. Wonka, and M. Wimmer. Gaussian material synthesis. *ACM Transactions on Graphics (TOG)*, 37(4):76, 2018.
 - [183] E. Bruneton and F. Neyret. A survey of nonlinear prefiltering methods for efficient and accurate surface shading. *IEEE Transactions on Visualization and Computer Graphics*, 18(2):242–260, 2012.
 - [184] S. Brabec, T. Annen, and H.-P. Seidel. Shadow mapping for hemispherical and omnidirectional light sources. In *Advances in Modelling, Animation and Rendering*, pages 397–407. Springer, 2002.

- [185] P.-P. J. Sloan, W. Martin, A. Gooch, and B. Gooch. The lit sphere: A model for capturing npr shading from art. In *Graphics interface*, volume 2001, pages 143–150, 2001.
- [186] J. Filip and R. Vávra. Template-based sampling of anisotropic brdfs. In *Computer Graphics Forum*, volume 33, pages 91–99. Wiley Online Library, 2014.
- [187] S. Ioffe and C. Szegedy. Batch normalization: Accelerating deep network training by reducing internal covariate shift. *arXiv preprint arXiv:1502.03167*, 2015.
- [188] Y. Jia, E. Shelhamer, J. Donahue, S. Karayev, J. Long, R. Girshick, S. Guadarrama, and T. Darrell. Caffe: Convolutional architecture for fast feature embedding. In *Proceedings of the 22nd ACM international conference on Multimedia*, pages 675–678. ACM, 2014.
- [189] D. P. Kingma and J. Ba. Adam: A method for stochastic optimization. *arXiv preprint arXiv:1412.6980*, 2014.
- [190] Z. Xu, J. B. Nielsen, J. Yu, H. W. Jensen, and R. Ramamoorthi. Minimal brdf sampling for two-shot near-field reflectance acquisition. *ACM Transactions on Graphics (TOG)*, 35(6):188, 2016.

ProQuest Number: 28318033

INFORMATION TO ALL USERS

The quality and completeness of this reproduction is dependent on the quality and completeness of the copy made available to ProQuest.



Distributed by ProQuest LLC (2021).

Copyright of the Dissertation is held by the Author unless otherwise noted.

This work may be used in accordance with the terms of the Creative Commons license or other rights statement, as indicated in the copyright statement or in the metadata associated with this work. Unless otherwise specified in the copyright statement or the metadata, all rights are reserved by the copyright holder.

This work is protected against unauthorized copying under Title 17,
United States Code and other applicable copyright laws.

Microform Edition where available © ProQuest LLC. No reproduction or digitization of the Microform Edition is authorized without permission of ProQuest LLC.

ProQuest LLC
789 East Eisenhower Parkway
P.O. Box 1346
Ann Arbor, MI 48106 - 1346 USA